THESIS

MOIST STATIC ENERGY AND THE MADDEN-JULIAN OSCILLATION: UNDERSTANDING INITIATION, MAINTENANCE AND PROPAGATION THROUGH THE APPLICATION OF NOVEL DIAGNOSTICS

Submitted by

Brandon Wolding

Department of Atmospheric Science

In partial fulfillment of the requirements

For the Degree of Master of Science

Colorado State University

Fort Collins, Colorado

Spring 2014

Master's Committee:

Advisor: Eric Maloney

Richard Johnson
Dan Cooley

ABSTRACT

MOIST STATIC ENERGY AND THE MADDEN-JULIAN OSCILLATION: UNDERSTANDING INITIATION, MAINTENANCE AND PROPAGATION THROUGH THE APPLICATION OF NOVEL DIAGNOSTICS

As the dominant mode of tropical intraseasonal variability, the Madden-Julian Oscillation (MJO) has enormous societal impacts. Despite four decades of research motivated by these impacts, the processes that drive the initiation, maintenance and propagation of the MJO are still poorly understood. The development of large scale moisture anomalies plays an important role in many recent theories of the MJO, including moisture mode theory. This study identifies processes that support the development, maintenance and propagation of moisture anomalies associated with the MJO.

A new set of objective MJO diagnostics, obtained as an extension of CEOF analysis, are introduced. These diagnostics provide useful measures of previously overlooked information yielded by CEOF analysis, including an objective measure that allows geographically disparate locations to be compared and contrasted throughout a reference MJO lifecycle. Compositing techniques based on this measure are applied to the MJO in an attempt to determine key physical processes affecting the MSE budget, identify prominent geographical variability of these processes, and highlight changes in the mean state winds and moisture field that explain this variability.

The MSE budget reveals that variations in MSE associated with the MJO are largely the result of variations in column integrated moisture content ($\sim$ 90%), the majority of which occur between 850-500 hPa ($\sim$ 75%). Easterly(westerly) low level wind anomalies to the east(west) of the MJO result in a reduction(enhancement) of drying due to horizontal

advection, which is only partially offset by a reduction(enhancement) of surface latent heat flux. In the deep tropics (5°N−5°S) of the eastern hemisphere, anomalous horizontal advection is primarily the result of the anomalous winds acting on the mean state moisture gradient. Over the broader tropics (15°N−15°S), the anomalous horizontal advection appears to result primarily from the modulation of synoptic scale eddy activity. The incomplete cancelation that occurs between anomalous horizontal advection and anomalous surface latent heat flux allows for the enhancement(reduction) of MSE to the east(west) of the MJO, enhancing(reducing) convection and helping drive propagation of the MJO. Anomalous vertical moisture advection is the primary process maintaining moisture and MSE anomalies against dissipation by anomalous precipitation throughout the MJO lifecycle. Anomalously positive(negative) vertical moisture advection appears to slightly exceed anomalous precipitation during periods of enhanced(suppressed) convection, suggesting a potential positive feedback that could act to destabilize the MJO. Geographical changes in the MSE budget of the MJO are primarily associated with changes in the mean state winds and the mean state moisture gradient.

These results suggest that MJO convective anomalies are maintained by anomalous vertical moisture advection, and that propagation of these convective anomalies results from the large scale asymmetrical dynamical response to equatorial heating occurring in a specific arrangement of mean state winds and mean moisture gradient. The findings of this study support the hypothesis that the MJO is a moisture mode.

ACKNOWLEDGMENTS

I would like to express my utmost gratitude to several people who have helped make this work, and my time here at CSU, possible. Dr. Eric Maloney, thank you for taking a chance on a vagabond from an "untraditional" background. Your patience as I have journeyed through my research has been extraordinary, and is ultimately what made the results here possible. Thank you Dr. Richard Johnson and Dr. Dan Cooley for serving on my Master's committee, and providing your valuable insight and time throughout this process. An immeasurable debt is owed to me colleagues for allowing me to take their "open-door" policy to its practical limits. In particular, thank you Jim Benedict, Walter Hannah, Gus Alaka and James Ruppert. Our conversations and debates will live fondly in my memory throughout my life. Chris Slocum, thank you for the selfless hours you have spent helping me format this document. Chris Eldred, thank you for the random gems of insight you provide on a regular basis. Thank you Dr. Bill Cotton and Dr. Sue van den Heever for providing me with such a warm welcome to CSU. And finally, thank you Mom, Dad and Jennifer for all the support that has made the difficult tasks seem easy. This project was funded by National Science Foundation under Grants AGS-1062161 and AGS-1025584.

TABLE OF CONTENTS

CHAPTER 1

Introduction

1.1. Fundamentals of the Deep Tropics

A basic understanding of several unique features of the tropical atmosphere is essential for understanding current theories of the MJO. However, the implications of these features are vast, and a full treatment is beyond the scope of this thesis. As such, only a brief introduction to these features, limited in scope to aspects crucial to understanding the MJO, will be provided.

1.1.1. Weak Temperature Gradients

Observations show that, in general, the tropics are unable to maintain substantial free tropospheric temperature gradients. While the SST gradient from the Indo-Pacific warm pool to the east Pacific cold tongue can be up to 10°C, free tropospheric temperature typically varies by less than less 1°C across the tropics (Holton 2004). Convection over tropical warm pool regions can be communicated effectively over large longitudinal distances through the action of equatorial waves (Matsuno 1966; Heckley and Gill 1984; Wheeler and Kiladis 1999; Maloney and Sobel 2007), homogenizing the tropical free tropospheric temperature profile and roughly constraining it to the moist adiabatic structure determined by SST in the warm pool regions (Holton 2004). In contrast, boundary layer characteristics are closely tied to underlying SST. The combination of local control of boundary layer characteristics and remote control of the free tropospheric temperature profile ensures the distribution of diabatic heating from convection is directly linked to SST patterns. Large-scale circulations influenced by the distribution and structure of diabatic heating in turn affect SST patterns,

intricately linking tropical atmospheric and oceanic processes. Consequently, a satisfactory description of a large-scale tropical phenomenon must include consideration of atmospheric and oceanic processes over a large range of scales.

Large-scale tropical motions elude satisfactory description by a single dynamical framework. Several scale analyses (Charney 1963; Sobel et al. 2001; Holton 2004; Yano and Bonazzola 2009) of the tropics across a wide range of spatial and temporal scales have revealed two potential regimes (Yano and Bonazzola 2009): 1.) a balanced state, where diabatic heating is balanced by adiabatic cooling and gravity waves are unimportant to leading order, or 2.) a unbalanced state, where diabatic heating induces a temperature tendency, and equatorial waves modified by convective diabatic heating play an important role. High sensitivities to horizontal scale in the resulting solutions, as well as ambiguities inherent in such scale analyses, allow for the potential mutual validity of both regimes across a wide range of spatial and temporal scales (Yano and Bonazzola 2009). Observational constraints on scaling, as well as observational estimates of the validity of the balanced state itself (Yano and Bonazzola 2009), indicate that on timescales longer than a few days the balanced regime holds on meso to synoptic spatial scales, and potentially beyond (Haertel et al. 2008). This balanced state is known as Weak Temperature Gradient (WTG) balance, and its implications have the utility of providing great insight as to how diabatic heating across a range of scales combines to influence the large-scale circulation.

1.1.2. Tropical Heating Profiles and Vertical Motion Under WTG Balance

To the extent that the WTG balance regime is valid, and diabatic heating is balanced by adiabatic cooling, knowledge of the structure of diabatic heating imparts knowledge of the vertical and horizontal circulations associated with that heating. On the time and space

scales that WTG balance holds, a diabatic heating profile in the tropical atmosphere is largely the result of radiation and the net effect of a population of clouds. The vertical structure of diabatic heating determines the vertical structure of vertical velocity, which in turn prescribes the vertical structure of vertical and horizontal convergence/divergence. As will be discussed later, the manner in which this circulation response influences the further evolution of diabatic heating may be at the foundation of understanding the MJO. Consequently, understanding how the diabatic heating profiles of a variety of individual clouds within larger cloud populations combine to influence the large-scale circulation response is of chief importance.

Variations in the vertical structure of Q_1, the apparent heat source (Yanai et al. 1973), occur on a range of time-scales and can be associated with phenomena ranging from the diurnal cycle to large-scale atmospheric waves (Lin and Johnson 1996a; Schumacher et al. 2007). Large geographical variability exists in the evolution and predominance of different cloud types, which is reflected in the characteristic vertical structure of Q_1 at each location (Schumacher et al. 2007). Furthermore, the magnitude of heating associated with various cloud populations is disproportionate to the frequency of occurrence of those populations (Schumacher et al. 2007; Zhang and Hagos 2009). Fortunately, several simplifications can be made when considering area averaged (10^3-10^5 km^2) diabatic heating profiles relevant to the tropical large-scale circulation.

Schumacher et al. (2007) idealized latent heating profiles for different precipitating cloud types. Zhang and Hagos (2009) used sounding data from eight field campaigns in diverse regions of the tropics to investigate how these idealized latent heating profiles could be used as the building blocks (Mapes et al. 2006) for constructing the area averaged heating profile.

In addition to a deep tropospheric clear sky radiative cooling profile, three predominant heating profiles were present in large area average composites (Zhang and Hagos 2009); a bottom heavy profile with peak heating near 700 hPa, a profile with peak heating near 400 hPa , and a top heavy profile with peak heating at 400 hPa and a cooing peak near 400 hPa. Heating profiles at the various locations were found to follow a typical pattern of evolution, transitioning from the radiative cooling profile to the bottom heavy profile, transitioning through to the top heavy profile and back to radiative cooling. Zhang and Hagos (2009) then used linear combinations of the idealized profiles of Schumacher et al. (2007) to estimate fractional contributions of the various cloud types to each composite heating profile. The idealized deep convective profile contributed roughly 40% to all large area averaged profiles, but the idealized shallow/congestus and stratiform profiles dominated the remainder of the bottom heavy and top-heavy profiles respectively.

Zhang and Hagos (2009) then used a simple linear WTG model to show that the 3-D wind response and associated moisture convergence were highly sensitive to the vertical diabatic heating structure of the three large area average profiles. The response to the bottom heavy heating profile was wind and moisture convergence(divergence) below(above) 700 hPa, though the moisture divergence above 700 hPa was notably weaker in magnitude. The response to the profile with peak heating near 400 hPa consisted of strong wind and moisture convergence below 450 hPa, and strong wind divergence above. The top heavy heating profile resulted in wind and moisture convergence between 400 and 750 hPa, wind and stronger moisture divergence below, and wind divergence above.

The sensitivities of moisture convergence to these three area-averaged heating profiles, taken together with their typical pattern of evolution within convectively coupled tropical

disturbances (Kiladis et al. 2009), alludes to a typical evolution pattern of the moisture field. This evolution of cloud populations, diabatic heating, and moisture has been found as part of a self-similar structure (Kiladis et al. 2009) of tropical phenomena that vary greatly in scale and propagation speed, ranging from various convectively coupled equatorial waves (Kiladis et al. 2009) to the MJO (Benedict and Randall 2007; Jiang et al. 2011).

1.1.3. Precipitation and Water Vapor

A dry free tropospheric environment is thought to inhibit deep convection by reducing buoyancy of rising parcels and promoting downdrafts that penetrate into the boundary layer. Sensible and latent heat of a rising plume are reduced as entrained dry air must be warmed and saturated. Similarly, downdrafts that penetrate the boundary layer reduce boundary layer theta-e, potentially inhibiting further convection(Raymond, 1995). Modeling results(Raymond 2001) and observations (Bretherton et al. 2004; Peters and Neelin 2006; Holloway and Neelin 2009; Neelin et al. 2009; Sahany et al. 2012) have shown precipitation to be a strongly increasing non-linear function of various measures of free tropospheric moisture. In contrast, Holloway and Neelin (2009) and Bretherton et al. (2004) used radiosonde records at Nauru (0.5°S, 166.9°E) and Kwajalein (8.4°N, 167.4°W) islands respectively to show that boundary layer specific humidity and relative humidity vary little in relation to precipitation. CAPE similarly shows little relation to precipitation on daily timescales (Raymond 1995; Bretherton et al. 2004), given the strong influence that boundary layer characteristics have on its value and the weak free tropospheric temperature gradients observed in the tropics.

When periods of low and high precipitation were compared, specific humidity variations were found to be largest between 850 hPa and 500 hPa (Bretherton et al. 2004; Holloway and Neelin 2009). Neelin et al. (2009) found that the tropical atmosphere exhibits a critical

threshold of lower free tropospheric water vapor, beyond which precipitation and convective organization rapidly increased. This idea is supported by the idealized modeling study of Tompkins (2001), who found substantial positive moisture convection feedbacks. In the model, convection acted to moisten its surrounding environment, making conditions more favorable for further convection and leading to self-organization even in the absence of wind shear or a SST gradient. More enlightening was the finding of Neelin et al. (2009) that the critical threshold of lower free tropospheric water vapor was not influenced by SST, belying the traditional understanding of the relation between SST and precipitation on longer timescales. Instead of directly influencing precipitation by destabilizing the boundary layer through surface fluxes, Neelin et al. (2009) found SSTs linkage to precipitation was through its influence on the moistening processes of the lower free troposphere. By driving moisture convergence and enhancing surface fluxes for a given wind speed, regions of high SST allow the lower free troposphere to be near the critical threshold of water vapor more frequently. This conclusion is also supported by Tompkins (2001), who found that convection did not spontaneously develop when a region of enhanced SST was introduced into the previously discussed idealized model. Instead, convection that was already established elsewhere had to propagate to the region of enhanced SST.

As previously discussed, WTG balance allows diabatic heating to be related to the large-scale tropical circulation. The structure of the diabatic heating influences the structure of the circulation response, which in turn influences the evolution of the moisture field. The relationship of lower tropospheric moisture to precipitation implies that this strong coupling influences the distribution and structure of further diabatic heating. In other words, the

distribution and structure of moisture/diabatic heating determines the evolution of moisture/diabatic heating. This idea is at the heart of many theories of the MJO, but before these theories are discussed, several theoretical tools that will help frame and simplify further discussion must be introduced.

1.2. The Moist Static Energy Budget

The moist static energy (MSE) budget has played a crucial role in developing an understanding of various aspects of tropical convection (Neelin and Held 1987), and has a prominent role in the remainder of this work. Accordingly, a thorough introduction will be provided here, including a brief derivation with the intent of highlighting the assumptions that are commonly made and the physical interpretations of certain terms, which can differ from their mathematical meaning.

1.2.1. Derivation

Dry Static Energy(DSE), s, is defined as

$$s = C_p T + gz \tag{1.1}$$

If major sources and sinks of DSE are limited to condensation, evaporation, and radiation, the time tendency of DSE from a Eulerian perspective can be written (Yanai and Johnson 1993)

$$\frac{\partial s}{\partial t} + \vec{v} \cdot \nabla s + \omega \frac{\partial s}{\partial p} = Q_r + L(c - e) \tag{1.2}$$

where Q_r is the radiative heating rate in $J\,kg^{-1}\,s^{-1}$, c and e are the atmospheric condensation and evaporation rate in $kg\,kg^{-1}\,s^{-1}$ respectively, $\vec{v}$ is the horizontal velocity vector and L is

the latent heat of condensation. Applying the continuity equation, 1.2 can be rewritten as

$$\frac{\partial s}{\partial t} + \nabla \cdot (s\vec{v}) + \frac{\partial (s\omega)}{\partial p} = Q_r + L(c - e) \tag{1.3}$$

Decomposing each variable into a large-scale mean and deviation from that mean, such that for some quantity A, $A = \overline{A} + A'$, then applying a large-scale average to 1.3 and using Reynolds averaging gives

$$\frac{\partial \overline{s}}{\partial t} + \nabla \cdot (\overline{s}\overline{\vec{v}}) + \nabla \cdot (\overline{s'\vec{v}'}) + \frac{\partial (\overline{s}\,\overline{\omega})}{\partial p} + \frac{\partial (\overline{s'\omega'})}{\partial p} = Q_r + L(\overline{c} - \overline{e}) \tag{1.4}$$

Here a large-scale average is considered to be large enough to contain an ensemble of clouds but small enough to compromise only a small fraction of a large-scale disturbance such as the MJO. Applying continuity again, and rearranging terms gives

$$Q_1 \equiv \frac{\partial \overline{s}}{\partial t} + \overline{\vec{v}} \cdot \nabla \overline{s} + \overline{\omega} \frac{\partial \overline{s}}{\partial p} = Q_r + L(\overline{c} - \overline{e}) - \nabla \cdot (\overline{s'\vec{v}'}) - \frac{\partial (\overline{s'\omega'})}{\partial p} \tag{1.5}$$

A similar approach can be taken to look at the behavior of the latent heat budget on a large-scale average. Assuming area averaged sources and sinks of latent heat are limited to evaporation and condensation, the latent heat budget is given by (Yanai and Johnson 1993)

$$L\left(\frac{\partial q}{\partial t} + \vec{v} \cdot \nabla q + \omega \frac{\partial q}{\partial p}\right) = -L(c - e) \tag{1.6}$$

where q is specific humidity in $kg\,kg^{-1}$. Applying the steps used to retrieve equations 1.3 through 1.5 gives

$$Q_2 \equiv -L\left(\frac{\partial \overline{q}}{\partial t} + \overline{\vec{v}} \cdot \nabla \overline{q} + \overline{\omega} \frac{\partial \overline{q}}{\partial p}\right) = L(\overline{c} - \overline{e}) - L\left(\nabla \cdot (\overline{q'\vec{v}'})\right) - L\left(\frac{\partial (\overline{q'\omega'})}{\partial p}\right) \tag{1.7}$$

Q_1 and Q_2, the apparent heat source and apparent moisture sink (Yanai et al. 1973) respectively, are termed "apparent" because they include eddy flux convergences from unresolved motions, which are not true sources. Neglecting horizontal eddy flux convergences, which are assumed to be small, and subtracting Q_2 from Q_1 produces the MSE budget:

$$Q_1 - Q_2 = \frac{\partial \overline{h}}{\partial t} + \overline{\vec{v}} \cdot \nabla \overline{h} + \overline{\omega} \frac{\partial \overline{h}}{\partial p} = Q_r - \frac{\partial (\overline{h'\omega'})}{\partial p} \tag{1.8}$$

Here the terms involving condensation and evaporation have dropped out, as transformations between DSE and latent heat are incorporated in MSE, making it a variable that is approximately conserved in moist adiabatic processes. As defined here, MSE is only approximately conserved in moist adiabatic processes because latent heat exchanges associated with ice processes are neglected.

Further simplification and insight can be obtained with the application of a vertical integral over the depth of the troposphere to equation 1.8. The vertical integral is defined such that, for some quantity A, $\langle A \rangle = \frac{1}{g} \int_{p_t}^{p_s} A dp$, where p_s and p_t are the surface and tropopause pressure respectively. Applying this definition to each term in equation 1.8 gives

$$\langle Q_1 \rangle - \langle Q_2 \rangle = \left\langle \frac{\partial \overline{h}}{\partial t} \right\rangle + \langle \overline{\vec{v}} \cdot \nabla \overline{h} \rangle + \left\langle \overline{\omega} \frac{\partial \overline{h}}{\partial p} \right\rangle = \langle Q_r \rangle - \left\langle \frac{\partial (\overline{h'\omega'})}{\partial p} \right\rangle \tag{1.9}$$

Assuming hydrostatic balance and applying the chain rule gives $-\frac{\omega'}{g} \approx \rho w'$. Further assuming the vertical eddy flux of MSE through the tropopause is zero, and noting that z' is zero at the surface, gives

$$-\left\langle \frac{\partial (\overline{h'\omega'})}{\partial p} \right\rangle = -\frac{1}{g} \left(\overline{h'\omega'} \right)_{p_s} = \rho \left(\overline{h'w'} \right)_{p_s} = \rho \left[C_p \left(\overline{T'w'} \right) + L \left(\overline{q'w'} \right) \right] = SH + LH \tag{1.10}$$

where SH and LH are the surface sensible and latent heat fluxes respectively. The vertical eddy flux convergences throughout the column have canceled in the vertical, with only surface fluxes contributing to the MSE tendency. Thus, the vertically integrated MSE budget simplifies to

$$\langle Q_1 \rangle - \langle Q_2 \rangle = \left\langle \frac{\partial \overline{h}}{\partial t} \right\rangle + \left\langle \overline{\vec{v}} \cdot \nabla \overline{h} \right\rangle + \left\langle \overline{\omega} \frac{\partial \overline{h}}{\partial p} \right\rangle = \langle Q_r \rangle + SH + LH \tag{1.11}$$

which can also be written

$$\langle Q_1 \rangle - \langle Q_2 \rangle = \left\langle \frac{\partial \overline{h}}{\partial t} \right\rangle + \left\langle \overline{\vec{v}} \cdot \nabla \overline{h} \right\rangle + \left\langle \overline{h} \cdot \nabla \overline{\vec{v}} \right\rangle = \langle Q_r \rangle + SH + LH \tag{1.12}$$

using integration by parts with the assumption that vertical velocity is zero at the surface and the tropopause (Back and Bretherton 2006).

Throughout the derivation of this budget several assumptions have been made that may potentially impact its calculation in practice, as well as the fidelity with which it captures the physical processes it is meant to represent. As previously mentioned, the use of the latent heat of condensation earlier neglects energy exchanges involved with ice processes. It has been argued that horizontal eddy flux convergence may not be insignificant in certain situations. Practical considerations regarding pressure levels available in reanalysis datasets, combined with imprecise knowledge of tropical tropopause heights, impacts the calculation of the vertical integral. Similarly, given that the MSE is highest near the upper and lower boundaries, the assumption that vertical velocity is zero at these boundaries may be a potential source of substantial error. It is also worth noting that while the MSE budget is typically calculated using the vertical advection term as in equation 1.15, the vertical

advection term is commonly interpreted as being the net export of MSE by divergent motions through the depth of the column as in equation 1.12.

1.2.2. Interpretation Under WTG Balance

While the form of the MSE budget introduced in equation 1.15 is perfectly valid under WTG balance, further manipulation provides substantial simplification and a more direct physical interpretation of several terms. Of course, such simplifications and physical interpretations are only valid to the extent that WTG balance holds. Therefore, the following discussion should be understood to be a "first order" interpretation of the MSE budget.

In WTG balance

$$\left\langle \frac{\partial h}{\partial t} \right\rangle = \left\langle \frac{\partial Lq}{\partial t} \right\rangle \tag{1.13}$$

The goal of this study is to investigate the processes that support the development, maintenance and propagation of moisture anomalies (synonymous with MSE anomalies under WTG balance) associated with the MJO. The processes that affect $\langle Lq \rangle$ (and therefore $\langle h \rangle$) are given by the right hand side of equation 1.14,

$$\left\langle \frac{\partial Lq}{\partial t} \right\rangle = -\left\langle \vec{v} \cdot \nabla Lq \right\rangle - \left\langle \omega \frac{\partial Lq}{\partial p} \right\rangle - LP + LH \tag{1.14}$$

where the overbars denoting area averages have been dropped for simplicity, and we have approximated net atmospheric condensation minus evaporation as precipitation. In practice, it is often preferable to use equation 1.15,

$$\left\langle \frac{\partial h}{\partial t} \right\rangle = -\left\langle \vec{v} \cdot \nabla h \right\rangle - \left\langle \omega \frac{\partial h}{\partial p} \right\rangle + \langle Q_r \rangle + SH + LH \tag{1.15}$$

where

$$\left\langle \omega \frac{\partial h}{\partial p} \right\rangle = \left\langle \omega \frac{\partial s}{\partial p} \right\rangle + \left\langle \omega \frac{\partial Lq}{\partial p} \right\rangle \tag{1.16}$$

as MSE has the desirable quality of being an intensive quantity that is approximately conserved in moist adiabatic processes. Therefore, in order to gain physical insight into the processes affecting $\langle Lq \rangle$, each term on the right hand side of equation 1.14 must be quantified by terms on the right hand side of equation 1.15. In WTG balance

$$\langle \vec{v} \cdot \nabla h \rangle = \langle \vec{v} \cdot \nabla Lq \rangle \tag{1.17}$$

Given this, the only terms remaining on the right hand side of equation 1.14 that need to be quantified by terms on the right hand side of equation 1.15 are $-\left\langle \omega \frac{\partial Lq}{\partial p} \right\rangle$ and $-LP$. While it is not possible to quantify the affects of these two terms separately using equation 1.15, their net affect can be obtained using

$$\left\langle \omega \frac{\partial s}{\partial p} \right\rangle = LP + \langle Q_r \rangle + SH \tag{1.18}$$

Equation 1.18 is an expression of WTG balance, stating that area averaged diabatic heating is balanced by area averaged adiabatic cooling. Using equation 1.18, in combination with equations 1.15 and 1.16, results in

$$\left\langle \omega \frac{\partial h}{\partial p} \right\rangle - \langle Q_r \rangle - SH = LP + \left\langle \omega \frac{\partial Lq}{\partial p} \right\rangle \tag{1.19}$$

Now each term on the right hand side of equation 1.14 can be quantified using equation 1.15 as follows:

$$\langle \vec{v} \cdot \nabla Lq \rangle = \langle \vec{v} \cdot \nabla h \rangle \tag{1.20}$$

$$\left\langle \omega \frac{\partial Lq}{\partial p} \right\rangle + LP = \left\langle \omega \frac{\partial h}{\partial p} \right\rangle - \langle Q_r \rangle - SH \tag{1.21}$$

$$LH = LH \tag{1.22}$$

1.2.3. Gross Moist Stability (GMS)

Since its introduction by Neelin and Held (1987), numerous mathematical definitions have been used to represent the conceptual measure known as GMS. GMS represents the net export by divergent motions of an intensive quantity conserved in moist adiabatic processes (such as MSE) per unit measure of moist convection (such as convective mass flux) (Raymond et al. 2009). In the context of MSE in a WTG framework, GMS is an area-average metric of instability, representing the ability of convection to enhance or dissipate column MSE, thereby supporting or inhibiting further convection. For example, Bretherton et al. (2005) found that self-aggregation of convection occurred in a large-domain CRM with negative GMS, whereby convection moistened its own environment, favoring further convection in a manner similar to the aforementioned results of Tompkins (2001)

While GMS as a conceptual measure has remained relatively unchanged, the way in which GMS is viewed in relation to tropical convection is continually evolving. GMS has been used as a tool to provide further insight to aspects of tropical convection ranging from climatological features such as the ITCZ (Back and Bretherton 2006) to theories for the MJO such as moisture mode theory (Sobel et al. 2001; Raymond 2001; Raymond and Fuchs 2009; Maloney et al. 2010). Further discussion of GMS in relation to the MJO will be left to later sections.

1.3. MJO Fundamentals

1.3.1. Historical Perspective

"...we stumbled upon an apparent long-period oscillation in the station pressure and zonal wind components at Canton Island (3S,172W). The frequency of this oscillation is much lower than that of any wave mode to be hypothesized, but is higher than can be expected from any component of a seasonal variation" (Madden and Julian 1971). These words, from the opening paragraph of Madden and Julian (1971), mark the first documentation of the phenomena that would later come to be known as the Madden-Julian Oscillation (MJO).

In the years leading up to the discovery of the MJO, knowledge of the tropical atmosphere took several enormous leaps forward, driven by, and in turn driving, a resurgence of interest in the tropics. Discovery of the Quasibiennial Oscillation (QBO) (Ebdon 1960) motivated many of the principal questions of the time, while the seminal work of Matsuno on equatorial wave theory (Matsuno 1966) provided potential explanations. Simultaneously, ever increasing computing capabilities, combined with the development of the fast Fourier transform (Cooley and Tukey 1965), allowed researchers to fully exploit sparse tropical observations. It was in this context that the first observations of Matsuno's theoretically predicted mixed Rossby-gravity waves (Lindzen and Matsuno 1968), followed shortly after by the first observations of similarly predicted Kelvin waves (Wallace and Kousky 1968), were made.

Madden and Julian (1971) initially set out to similarly investigate Matsuno's predicted wave modes over a broader frequency range (Lau and Waliser 2012) by analyzing 10 years of rawinsonde data from Kanton Island (3°S, 172°W). Application of spectral analysis to surface pressure, winds, temperature and humidity revealed a broadband peak in the 40 to 50 day range, with upper and lower level winds being 180° out of phase and lower levels

winds nearly in phase with surface pressure. The periodicity and structure of the observed oscillation did not correspond to any of the theoretical equatorial wave modes. Madden and Julian (1972) expanded the analysis of Madden and Julian (1971) to include rawinsonde data from 25 stations across the tropics, concluding "The sum total of evidence indicates that the oscillation is the result of an eastward movement of large-scale circulation cells oriented in the equatorial (zonal) plane". Madden and Julian (1972) provided the first global description and schematic depiction of the MJO, which would serve as the jumping off point for the following four decades of research.

1.3.2. Fundamental Structure and Characteristics

The elementary structure of the MJO is traditionally described as consisting of a large-scale coupling of deep convection and tropospheric circulation anomalies that propagate slowly eastward at $\sim 5\ \mathrm{m\,s^{-1}}$, though coherent signals in many other variables are present. The convective signal of the MJO is typically limited to the eastern hemisphere and western Pacific, beyond which the dynamical signal in winds and surface pressure continue to propagate eastward as waves uncoupled from convection at much higher speeds of ~ 30 to $35\ \mathrm{m\,s^{-1}}$ (Zhang 2005). The broad spectral peak of convection associated with the MJO extends from approximately 30 to 100 days and spans zonal wavenumbers 1 to 3 (Wheeler and Kiladis 1999), with a large degree of variability in the spectral power being observed over this range (Hendon and Salby 1994; Zhang 2005). The behavior of the MJO is much more episodic and irregular than the term oscillation implies, varying substantially by geographical location, being significantly modulated on seasonal and interannual timescales (Hendon and Salby 1994), and exhibiting differences in propagation speed and break duration from event to event.

The MJO primarily modulates climatological convection and the large monsoons of the summer hemisphere, following the seasonal migration of the ITCZ and warm SSTs (Hendon and Salby 1994). While boreal winter propagation is predominantly eastward, boreal summer migration has a substantial northward component and interacts with independent northward propagating ISV in the south Asian monsoon region (Rui and Wang 1990; Jones et al. 2004; Lau et al. 2012a). Due to the relative complexity of the boreal summer MJO, the aim of this research and further discussion will be aimed at the boreal winter (roughly October to April) MJO.

The salient features of the MJO can be observed by compositing a MJO lifecycle (Figure 1.1). Although the construction of the figure is detailed later, it shows the eastward propagation of anomalies in 850-500 hPa specific humidity (contours), OLR (shading), and winds at 850 hPa (arrows). In the eastern hemisphere moisture and convection are coupled with the large-scale circulation, with anomalous low-level (upper-level) westerlies (easterlies) to the west of the enhanced moisture and convection, and easterlies (westerlies) to the east. This large-scale circulation is similar to the circulation response to heating in the equatorial β-plane model of Gill (1980), and the influence of equatorial wave dynamics is immediately apparent. The low-level (upper-level) westerlies (easterlies) are associated with cyclonic (anticyclonic) Rossby wave like gyres, while the easterlies (westerlies) have a Kelvin wave like structure (Rui and Wang 1990). The combined structure of the lower and upper level winds form overturning circulations that link the convective and suppressed phases of the MJO.

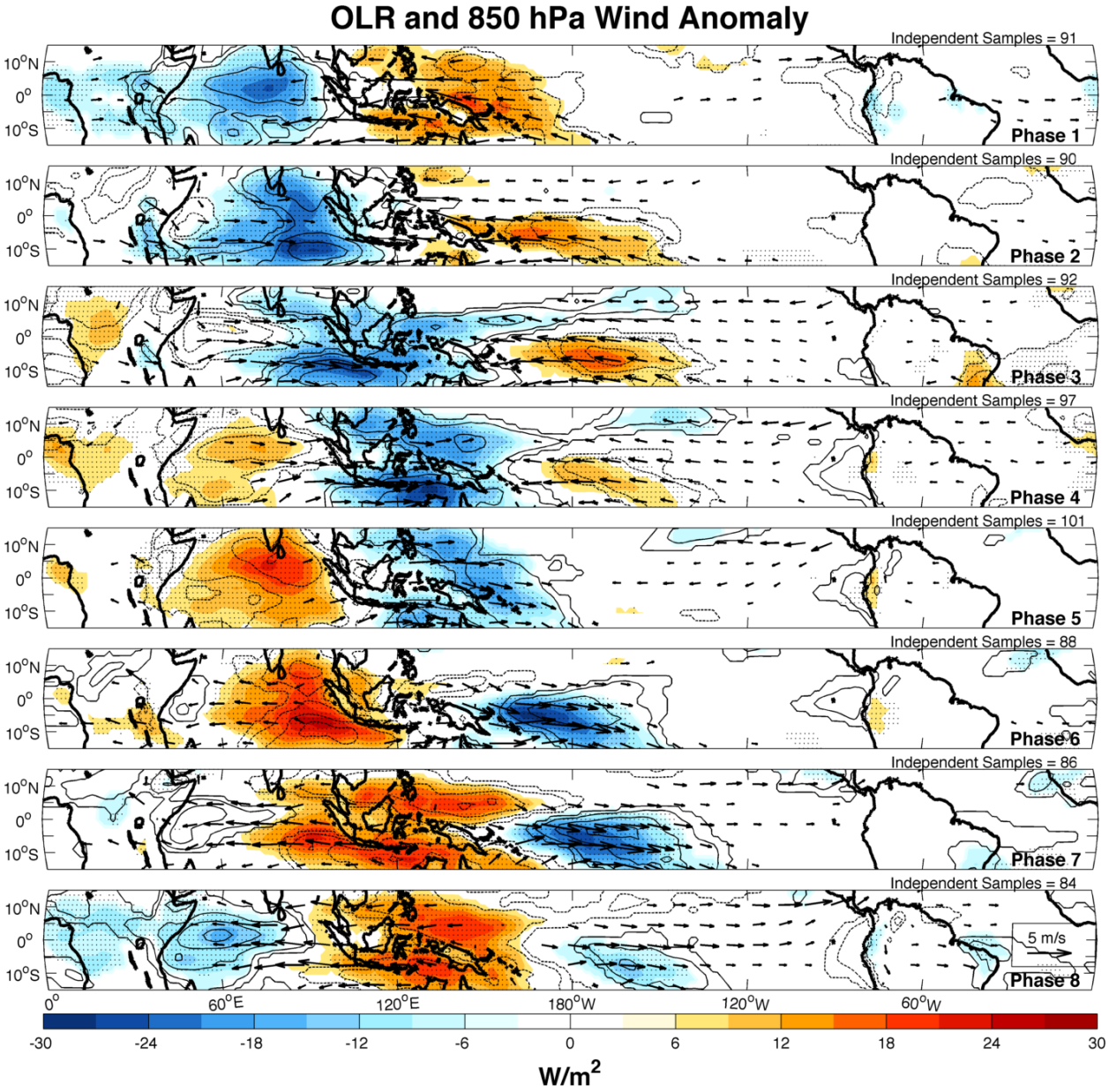

FIG. 1.1. ERAi composite of $q_{850,500}$ anomalies(contours), OLR anomalies (colored contours), and 850 hPa horizontal wind anomalies for 1981-2011 winters (October 1 - April 30). Bandpass filtering was not applied to these fields. Solid (dashed) contours are positive (negative) $q_{850,500}$ anomalies of 0.5,1.5,2.5,3.5 (-0.5,-1.5,-2.5,-3.5) $\mathrm{kg\,kg^{-1}}$. Wind vectors are statistically significant at the 95% level. A reference wind vector is provided in the lower right corner of the bottom panel. Stippling indicates OLR anomalies significant at the 95% level.

As convection moves eastward across the Indian Ocean, Maritime Continent and into the western Pacific, the phase relationship between the dynamical fields and convection changes

(Rui and Wang 1990). Convection weakens east of the dateline, allowing the dynamical response to decouple and propagate eastward as a Kelvin wave at 30 to 35 $\mathrm{m\,s^{-1}}$ (Matthews 2000; Zhang 2005). Therefore, MJO related variability in the dynamical fields consists of a convectively coupled propagating signal as well as a radiating atmospheric response to convection (Heckley and Gill 1984). Whether the former is considered to be the MJO and the latter a response, or both together are fundamental to the MJO remains an open question.

This traditional description of the MJO structure neglects many fundamental large-scale features central to understanding the MJO in a WTG framework, namely anomalies in water vapor, temperature, diabatic heating and divergence. These variables all exhibit large-scale patterns coherent with MJO convection and wind anomalies (Lin and Johnson 1996a; Kiladis et al. 2005; Benedict and Randall 2007), with low level convergence and increasing specific humidity east of the convective center and low level divergence and decreasing specific humidity to the west. These fields all display a westward tilt with height, the degree of which varies by geographical location (Kiladis et al. 2005).

Another feature that may prove key to understanding the MJO is its multi-scale structure. Nakazawa (1988) demonstrated that, far from being a homogenous packet of propagating convection, large-scale eastward propagating cloud complexes associated with ISV are actually composed of a hierarchy of convection, organized on a range of spatial and temporal scales propagating in all directions. The eastward propagation of the MJO does not result from the propagation of established convective systems, but instead from the tendency of new convective systems to develop slightly east of previous ones (Zhang 2005). The multi-scale structure of the MJO also contributes to the seemingly noisy signal of convection and

precipitation, where periods of suppressed convection and reduced precipitation occur even within the region of enhanced convection (Yamada et al. 2010).

1.3.3. Impacts and Interactions

The above description of the MJO, presented from a narrow mechanistic perspective and detached from the context of societal impacts, belies the great importance of, and motivation for its research. Furthering the understanding of the MJO is not merely a matter of satisfying trivial scientific curiosity, but has enormous prospective societal benefits and potential cascading effects of promoting understanding in seemingly disparate areas of atmospheric research. In support of this statement, various interactions between the MJO and phenomena across a range of timescales and geographical regions, put in context of their societal impacts, will be briefly discussed below.

The monsoon regions of Australia and southern Asia, where the MJO substantially modulates rainfall, encompass some of the most populated regions of the world. In addition, these regions make up a substantial portion of the world's agricultural production, which plays a critical role in supporting regional economies. Modulation of precipitation by intraseasonal variability in these regions is so prominent that it can often be discerned by eye from an unfiltered time series of precipitation. See Lau et al. (2012a) for further discussion of the societal importance of intraseasonal variability in these regions. Increased understanding of the interaction between the MJO and monsoon active/break periods, combined with appropriate use of extended MJO forecasts, could enhance the stability of agriculture production and economical growth in these regions.

While the convective signal of the MJO is primarily limited to the eastern hemisphere, the signal in fields such as zonal wind spans the breadth of the tropics. These zonal wind

anomalies modulate the environment that disturbances such as tropical cyclones exist in, to great effect. Maloney and Hartmann (2000a) found that hurricanes in the eastern Pacific during 850 hPa westerly wind phases are four times more frequent and substantially stronger than during easterly wind phases. Similar results were found for tropical cyclone activity in the Gulf of Mexico (Maloney and Hartmann 2000b) and Australia/Maritime Continent region (Hall et al. 2001). Increased understanding of how the MJO affects cyclone activity in these regions, combined with accurate MJO forecasts, could help provide extended-range forecasts of tropical cyclone activity (Slade and Maloney 2013).

MJO modulation of low-level zonal wind also drives intraseasonal fluxes of momentum, sensible and latent heat between the atmosphere and ocean. Variations in shortwave radiation reaching the surface, associated with changing cloud cover throughout the MJO lifecycle, contribute to intraseasonal variations in the surface energy budget and SST. In addition to being a potentially important feedback to the MJO, these changes are communicated effectively over great distances through the excitement of oceanic equatorial waves, remotely impacting other regions and phenomena. One of the more prominent relationships is that between the MJO and El Nino-Southern Oscillation (ENSO). While this relationship is still not well understood, observational evidence has demonstrated that the MJO played an important role in triggering the onset and demise of the 1997/1998 El Nino (McPhaden 1999; Takayabu et al. 1999), the largest on record (McPhaden 1999). A better understanding of the relationship between the MJO and ENSO has enormous potential benefits considering the well-documented far reaching teleconnections of ENSO.

Since the early 1980s it has been observed that the effects of the MJO extend far beyond the tropical atmosphere/ocean system to influence extratropical circulations (Lau et al.

2012b). Organized convective heating in the tropics can induce large-scale overturning circulations and excite Rossby wavetrains that propagate polewards, affecting the global circulation (Jin and Hoskins 1995). Composites analysis reveals patterns in extratropical 300 hPa geopotential height anomalies that evolve rather continuously as a function of MJO lifecycle (Lau et al. 2012b). It should be no surprise then that the MJO has been demonstrated to modulate phenomena as remote from the tropics as the North Atlantic, Arctic, and Antarctic oscillations (Roundy et al. 2010; Carvalho et al. 2005; Zhou and Miller 2005). Tropical-extratropical relations are particularly hard to diagnose, as they are not limited to one-way interactions. Convection in the tropics can be modulated by extratropical forcing, even outside of the westerly wind duct region (Hoskins and Yang 2000). In addition, high sensitivity of Rossby wavetrain propagation to background state winds and other modes of variability such as ENSO, makes elucidating relationships between the MJO and extratropical circulations difficult. Despite this, the prospect of leveraging the slow evolution of the MJO to extend useful predictions of background state extratropical weather conditions beyond traditional limits of numerical weather prediction remains promising (Moore et al. 2010; Lau et al. 2012b).

Clearly the MJO does not exist in isolation, insulated from its surroundings and other phenomena. Bridging the gap between short and long timescales of variability, connecting atmospheric and oceanic phenomena, and linking tropical and extratropical circulations, the MJO is truly a pervasive phenomenon. This pervasiveness means gains in understanding will have far reaching potential benefits, and provides immense motivation for further study.

1.4. MJO Theories

A comprehensive theory for any phenomena is tasked with explaining observed structural and behavioral characteristics throughout the lifecycle of the phenomena, including its growth, maintenance and decay. The immense complexity of the MJO, relative scarcity of observations and the lack of consensus within the research community as to what variables most succinctly capture the fundamental nature of the MJO make the construction of consistent benchmarks by which to assess any theory or model difficult. Wang (2012) proposes that a theory should explain: "(1) planetary-scale circulation coupled with a large-scale convective complex (Madden and Julian, 1972): (2) horizontal circulation comprising equatorial Kelvin and Rossby waves (Rui and Wang 1990) and baroclinic circulation with boundary layer convergence preceding the major convection region (Hendon and Salby 1994); (3) slow eastward propagation ($\sim$ 5 $\mathrm{m\,s^{-1}}$) in the eastern hemisphere (Knutson et al., 1986) and longitudinal dependence of amplification (Rui and Wang 1990); and (4) prominent northward propagation (Yasunari 1979, 1980) and off-equatorial westward propagation (Murakami 1980) during boreal summer in the summer monsoon region." Even these proposed benchmarks are debatable, as requiring a theory to explain preceding boundary layer convergence assumes a priori that it is essential to the MJO.

Some theories consider the MJO to be a response to an external forcing, while others treat it as a self-supporting response to some intrinsic atmospheric instability. Here only the latter will be discussed, as the former tend to lack observational support and diverge from the endeavors of this research. Instability theories regarding the MJO can be grouped into several broad categories, of which three will be discussed in turn below. These categories are based on: 1.) wave-CISK; 2.) wind-evaporation feedback; 3.) convection-water vapor feedbacks.

As many variations on each of these theories exist, discussion will be limited to an explanation of each theory in its original context and a brief description of subsequent developments that are particularly relevant. It should also be noted that while these theories vary fundamentally from each other, in many cases they do not exclude each other as potential mechanisms. A complete description of the MJO likely includes roles for several mechanisms to be discussed here.

1.4.1. Wave-CISK

The principal idea underlying wave conditional instability of the second kind (wave-CISK) is the existence of an unstable moisture convergence feedback, whereby low level convergence drives convective heating in a manner that strengthens geopotential perturbations, that in turn drive further low level convergence. Instead of acting to reduce the effective stratification in ascending regions by reducing adiabatic cooling, diabatic heating now dominates adiabatic cooling and promotes the unstable growth of disturbances. The CISK mechanism was first introduced by Charney and Eliassen (1964) as a feedback where small-scale convection drove Ekman pumping, which in turn drove large-scale low-level convergence that supported further convection. Lindzen (1974) introduced a modified CISK mechanism, termed wave-CISK, whereby a similar feedback occurred between tropical wave driven convergence and large-scale organized convection.

Many models have since been developed based on the wave-CISK mechanism, the character of which has proven to be very sensitive to the details of the moisture convergence feedback (Zhang 2005; Wang 2012). Unsuitable assumptions are often included, such as negligible horizontal MSE advection and an atmosphere conditionally unstable to moist convection. Problems many wave-CISK models have with explaining the MJO are a tendency

for instabilities to maximize at the smallest spatial scales and have faster than observed eastward propagation speeds (Zhang 2005; Wang 2012).

Rui and Wang (1990) introduced a related idea called frictional convergence instability (FCI), whereby boundary layer frictional moisture convergence effectively couples Kelvin and Rossby waves, resulting in an instability that propagates slowly eastward and favors the largest wavenumbers. While modeling studies have shown this model to be sensitive to the boundary layer frictional parameterization, it appears to be insensitive to the cumulus parameterization (Moskowitz and Bretherton 2000). Observational evidence has confirmed that the key feature of FCI, namely low-level moisture convergence leading convection, is present (Maloney and Hartmann 1998; Matthews 2000), but narrow in meridional extent.

1.4.2. Wind-Evaporation Feedback

A wind-evaporation feedback mechanism (Emanuel 1987; Neelin et al. 1987), later coined wind-induced surface heat exchange (WISHE) (Yano and Emanuel 1991), has been proposed to drive the instability supporting the MJO and its propagation. In linear WISHE theory, the low level anomalous wind structure of the MJO superimposed on the mean state winds introduces an asymmetry in SLHF. This asymmetry in SLHF induces an asymmetrical precipitation response such that convective heating anomalies occur in regions of positive temperature perturbations, supporting wave growth through generation of eddy available potential energy and driving eastward propagation.

Linear WISHE theory suffers the same deficiencies as wave-CISK in that it favors instability at the smallest scales and produces propagation speeds that are unrealistically fast. In addition, the original model relies on mean state low-level easterlies to produce eastward propagation, contrary to the observed westerly mean state of the equatorial Indian and west

Pacific oceans where the MJO is most active. The asymmetry of SLHF anomalies in linear WISHE is actually opposite of observations, where the largest SLHF anomalies occur in the region of anomalous westerlies west of convection (Lin and Johnson 1996a; Zhang and McPhaden 2000). Another questionable assumption made in the model is that anomalous winds are small relative to mean state winds, such that asymmetrical anomalous winds induce a substantial asymmetrical SLHF response. Despite these shortcomings, recent work (Sobel et al. 2010; Maloney et al. 2010) suggests that a modified wind-evaporation feedback mechanism may play a vital role in destabilization of the MJO.

1.4.3. Convection-Water Vapor Feedback

The intimate relationship between free tropospheric moisture and precipitation plays a central role in discharge-recharge and moisture mode based theories of the MJO. Discharge-recharge and moisture mode theories are related in that they revolve around processes that control free tropospheric humidity on intraseasonal timescales. The process of discharging/recharging free tropospheric humidity is at the core of moisture mode theory, and moisture mode theory is able to provide specific attribution to the processes responsible for driving the discharge/recharge mechanism. In essence, moisture mode theory provides a dynamical backbone and specific set of driving processes for discharge-recharge theory.

1.4.3.1. Discharge-Recharge Theory

Several studies (Bladé and Hartmann 1993; Kemball-Cook and Weare 2001; Kiladis et al. 2005; Benedict and Randall 2007) have documented an extended recharge period of gradual tropospheric moistening and increasing atmospheric instability preceding MJO convective

events, whose onset initiates a relatively rapid discharge in moisture and increase in atmospheric stability. Discharge is again followed by recharge, resulting in a cycle of relatively brief intense convective events separated by relatively long periods of recharge, the rate of which determines the overall period of the oscillation. Discharge-recharge theory does not exclude a role for wave-CISK or some form of WISHE theory, both of which may play an important role in driving the discharge and/or recharge processes. The structural and temporal characteristics of the observed recharge and discharge will be discussed in detail further below. In this theory, the modification of free tropospheric moisture content modulates deep convection through previously discussed affects on the buoyancy of convective plumes and prevalence of convective downdrafts.

While observations support the importance of the discharge/recharge process in the life-cycle of the MJO, eastward propagation is not intrinsically described by the theory. In order for eastward propagation to occur, some process must act to moisten and/or dry the atmosphere in a manner that is zonally asymmetric relative to the region of enhanced convection.

1.4.3.2. Moisture Mode Theory

Sobel et al. (2001) showed that application of a WTG scaling to a linear moist model, in which convective heating was controlled by a moisture variable, produced balanced dynamical modes as the result of interactions between moisture and large-scale wind fields. These balanced dynamical modes, termed moisture waves or moisture modes, can exist in a variety of dynamical frameworks with a range of background states, be stationary or propagating, and have a wide array of spatial and temporal scales (Sobel et al. 2001; Raymond and Fuchs 2009; Sobel and Maloney 2012, 2013). It is thought that many features of the MJO may be described by the simplified dynamics of a moisture mode (Raymond 2001).

At the heart of moisture mode theory is tropical WTG balance and the intimate relationship between moisture and convection. If the structure and distribution of diabatic heating can be diagnosed from the distribution of moisture, and the large-scale circulation response can be diagnosed from diabatic heating using WTG balance, the future distribution of moisture, and hence the evolution of the system, can be prognostically determined. If a feedback exists such that convection acts through various processes to increase moisture anomalies, instability occurs and the growth of a moisture mode may be supported. Furthermore, if those processes result in the horizontal movement of moisture anomalies, moisture mode propagation occurs. Moisture mode theory can thus be viewed as a way to describe the zonally asymmetric nature of the discharge/recharge process in a simplified dynamical framework, where knowledge of the moisture field alone, in context of the basic state, determines the evolution of the system. To the extent that the describe processes affecting the moisture field, various forms of WISHE, wave-CISK, and cloud-radiative feedback theories may have a role in moisture mode theories of the MJO.

The WTG balance inherent in moisture mode theory means the MSE budget becomes, to first order, a moisture tendency equation. The concept of GMS becomes particularly useful, representing the ability of convection to moisten its own environment and support moisture mode instability. An extension of this concept, termed effective GMS, allows the inclusion of effects relating to processes such as advection, self-enhancing surface fluxes and radiative effects. If effective GMS is negative, the net effect of these processes is to moisten the environment, allowing for the existence of moisture modes even when GMS is positive. Various forms of WISHE, wave-CISK, and cloud-radiative feedback theories may therefore have a role in a moisture mode theory of the MJO.

The current development of moisture mode theory seems to have many parallels with the publishing of Matsuno's theory on equatorial waves (Matsuno 1966) and subsequent discovery of their real-world counterparts in observations. The real world analogs were fundamentally similar to the simple structures predicted by Matsuno (1966), but had properties that were substantially modified by processes, such as convective-coupling, not accounted for in the simplified theory. While observations of the MJO clearly predated any such theory, current work on moisture mode theory involves an iterative process that tries to distinguish the fundamental attributes of the MJO predicted by moisture mode theory from attributes relating to processes not accounted for in this simplified framework. This iterative process involves using observations to determine processes critical to the MJO, using these critical processes to formulate idealized models in a WTG framework, and then trying to determine if similarities in the resulting moisture mode explain fundamental aspects of the MJO, and if differences are the result of processes not accounted for in the simplified WTG framework.

Many fundamental questions regarding moisture mode theory of the MJO remain. Are the large-scale circulation anomalies produced by MJO heating a quasi-equilibrium response, allowing their diagnosis from the heating field? Likewise, can convection in the MJO be assumed to be in a state of quasi-equilibrium with its forcings? What processes that affect the moisture field are not included in WTG balance dynamics, and what are the effects of neglecting these processes? How do other modes of variability interact with the MJO in a moisture mode framework?

1.5. MSE Budget of the MJO

While MSE budgets of the MJO have been investigated in several modeling studies (Maloney 2009; Maloney et al. 2010; Andersen and Kuang 2012; Wu and Deng 2013; Kim

et al. 2013a), only a few such analyses have been performed using reanalysis data (Kiranmayi and Maloney 2011; Wu and Deng 2013; Cai et al. 2013). While the results of the reanalysis studies are consistent to some degree, several findings of the various modeling studies appear to be, at least at first appraisal, inconsistent or even in direct contradiction (Andersen and Kuang 2012). Before further discussing the findings of previous MSE budget studies, the evolution of moisture and MSE throughout the MJO lifecycle, in both observations and reanalysis, will be briefly covered in the hope of providing context for further discussion.

1.5.1. Observations of Moisture and MSE

The modulation of atmospheric moisture content by the MJO was evident even in early studies (Madden and Julian 1972). Recent observational studies (Kemball-Cook and Weare 2001; Kiladis et al. 2005; Tian et al. 2010) have provided insight to the spatial and temporal evolution of the moisture field during a composite MJO event. These studies found that typical specific humidity anomalies during phases of peak enhanced or suppressed convection are on the order of 1 $\mathrm{gm\,kg^{-1}}$, while temperature anomalies tend to be less than 0.5°K . Therefore variations in moisture account for roughly 80% of MSE anomalies during MJO events, and the following discussion of the development of moisture anomalies largely reflects the development of MSE anomalies.

The findings of Kemball-Cook and Weare (2001), Kiladis et al. (2005) and Tian et al. (2010) agree that a typical progression of moisture and MSE anomalies in the Eastern Hemisphere is as follows. During the suppressed phase, dry anomalies extend from roughly 300 hPa down to at least 950 hPa with a strong peak near 600 hPa. Roughly 2 weeks prior to, and 30° longitude east of enhanced convection, lower tropospheric dry anomalies begin to slowly erode. This gradual moistening, possibly due to the gradual deepening and continual

detrainment of shallow convection, begins around the 950 hPa level and slowly progresses to around 700 hPa. Rapid moistening up to 300 hPa and the onset of deep convection follow, with a maximum moisture anomaly developing near 600 hPa. As this mid tropospheric moisture anomaly maximizes, marking the period of deepest convection, a low level drying has already began to occur. This low level drying gradually deepens in a progression similar to the gradual moistening process, marking the end of deep convection.

1.5.2. Moisture and MSE in Reanalysis

Global data assimilation products, commonly known as global reanalysis, provide easy to obtain, long-term spatially and temporally complete gridded datasets. These products make possible the study of phenomena that would otherwise rely on logistically impossible field campaigns (Zhang et al. 2013). While some fields are constrained by observations, reanalysis products rely on parameterization of processes thought to be critical to the MJO. Furthermore, observations in the Eastern Hemisphere, where the MJO is most prominent, are historically lacking. The necessary role reanalysis products must play in developing an understanding of the MJO make an evaluation of their validity paramount.

Tian et al. (2006) and Tian et al. (2010) compared the large-scale thermodynamic structure of the MJO in Atmospheric Infrared Sounder (AIRS) data to that in NCEP-DOE 2 and ERA-i reanalysis products respectively. Correlations of specific humidity between AIRS and ERA-I were 0.95, 0.8 and 0.3 in the free troposphere (above 850 hPa), boundary layers and near surface respectively, and were consistently 20% larger, 30% smaller and 80% smaller respectively. Similar correlation results were found for comparisons of the temperature field, though temperature anomalies in ERA-i were consistently smaller everywhere. ERA-I appears to have particular trouble with the leading edge of low-level moisture anomalies. The

tendency of reanalysis to underestimate boundary layer moistening is also evident in the results of Benedict and Randall (2007), who showed that low level moistening in ERA-40 begins near the 800 hPa level, followed 3 days later by boundary layer moistening. The findings of Mapes and Bacmeister (2012) may provide some insight into the errors observed in the reanalysis representation of the moistening phase of the MJO. Their analysis of Modern-Era Reanalysis for Reasearch and Applications (MERRA) analysis tendency fields suggested that the models convective scheme was prematurely transitioning to deep convection and acting as a unrealistic moisture sink during the moistening period. Despite the noted inconsistencies, Tian et al. (2010) concluded that ERA-I does pretty well describing the vertical moist thermodynamic structure of the MJO. Kim et al. (2013b) compared power spectra and coherence of precipitation in various reanalysis datasets with Global Precipitation Climatology Project (GPCP) and Tropical Rainfall Measuring Mission (TRMM) observations, similarly concluding that the MJO was well captured in ERA-i. In contrast, the precipitation power spectrum of the MJO is not captured as well in NCEP-DOE 2 and NCEP/NCAR reanalyses (Kim et al. 2013b). In addition, NCEP-DOE 2 has a poor representation of the vertical moist thermodynamic structure of the MJO, even showing opposite temperature anomalies compared to AIRS in the Indian Ocean (Tian et al. 2006).

1.5.3. MSE Budgets in Reanalysis

Column integrated MSE budgets have been performed using NCEP-DOE 2, ERA-I (Kiranmayi and Maloney 2011), ERA-40 (Cai et al. 2013) and NCEP/NCAR (Wu and Deng 2013) reanalysis data sets. Kiranmayi and Maloney (2011), Cai et al. (2013) and Wu and Deng (2013) found vertical advection anomalies to be the dominant term, roughly in quadrature with MSE tendency. Kiranmayi and Maloney (2011) and Wu and Deng (2013) found

that the affects of vertical MSE advection were partially offset by net radiation anomalies, which were dominated by LW fluxes. Vertical advection (radiative flux) anomalies acted to decrease (increase) MSE during times of anomalously high MSE, and had maximum values of approximately $20(10)\,\mathrm{W\,m^{-2}}$. Anomalous horizontal advection of MSE was found to be roughly in phase with MSE tendency in all three studies, and be partially offset by surface heat flux anomalies (not examined by Cai et al. (2013)), with maximum values of approximately 10 and $5\,\mathrm{W\,m^{-2}}$ respectively. The phase relationship between these terms and MSE tendency is less clear in Kiranmayi and Maloney (2011). Kiranmayi and Maloney (2011) found that changes in the moisture budget accounted for approximately 80% of the changes in the MSE budget. The residual in Kiranmayi and Maloney (2011) is considerable, at times exceeding the MSE tendency, and is a significant qualification of the analysis. The residuals of Wu and Deng (2013) and Cai et al. (2013) are not documented.

Kiranmayi and Maloney (2011) extended the analysis of the horizontal advection term, decomposing it into its zonal and meridional components and investigating contributions from mean and eddy components at various locations. Anomalous meridional advection was found to be dominant and have a more consistent phase relation with MSE tendency, though anomalous zonal advection still played a significant role. In several locations, the anomalous zonal wind acting against the mean moisture gradient dominated the zonal component, while at other locations the various contributors played more ambiguous roles. The anomalous meridional advection term was dominated by the enhancement or suppression of synoptic scale eddies mixing against the mean meridional moisture gradient. Further discussion of this term will be left until later.

1.5.4. MSE Budgets in Modeling Studies

Using the NCAR CAM3, a Relaxed Arakawa Schubert convective scheme, and a climatological seasonal cycle in SST and insolation, Maloney (2009) was able to produce realistic MJO-like ISV. A column integrated anomalous MSE budget showed the familiar buildup of MSE leading up to enhanced convection, followed by the decrease of MSE leading to suppressed convection. The phase relationship of the terms relative to MSE tendency was very similar to that observed in the previously discussed reanalysis budgets, but the relative magnitude of vertical advection anomalies and radiation anomalies were reduced, while that of horizontal advection anomalies and surface fluxes anomalies were much greater. Horizontal advection anomalies essentially drove the buildup of MSE, being partially offset by SLHF anomalies. Around the time of maximum anomalous precipitation, SLHF anomalies became very large and were important in aiding the maintenance of anomalous MSE. Anomalous meridional advection was again found to be a dominant term, primarily through the enhancement and suppression of synoptic scale eddies. This led Maloney (2009) to hypothesize that a realistic basic state distribution of winds and specific humidity was critical to the ability of climate models to simulate realistic ISV.

Maloney et al. (2010) similarly used the CAM3, this time with various idealized aquaplanet arrangements, to test the hypothesis of Maloney (2009). To the surprise of Maloney et al. (2010), an aquaplanet arrangement with a greatly reduced meridional SST gradient produced more realistic ISV than an aquaplanet arrangement with a realistic meridional SST gradient. Meridional advection anomalies were effectively reduced, though it remained a substantial contributor to the MSE budget. The role of zonal advection in driving MSE tendency was found to be very large, primarily by mean state winds advecting across an anomalous

specific humidity gradient. The phase relationship between low level wind anomalies and anomalous convection was more representative of the SPCZ, where the strongest westerly winds are directly beneath convection, allowing enhanced SLHF to support the maintenance of MSE anomalies. Excessively strong low-level mean state winds were a caveat of the results, as they appeared to produce a different partitioning of horizontal advection anomalies than in observations.

Andersen and Kuang (2012) used the SPCAM to investigate ISV on a zonally symmetric aquaplanet. Anomalous vertical and horizontal advection drove the MSE tendency, with synoptic eddy modulation driving changes in the anomalous meridional advection term. Anomalous longwave heating was an essential source of MSE near the convective center, balancing MSE loss due to anomalous vertical and horizontal advection. Anomalous SLHF was found to serve a minimal role in propagation, and was a relatively small sink of MSE near the convective center given the basic state easterlies of the model.

1.5.5. Summary

While MSE budgets of the MJO in reanalysis products are generally consistent, they differ in several respects from the results of the various modeling studies. The relative importance of vertical advection is reduced in modeling studies, while that of horizontal advection horizontal advection is increased. The relative importance of radiative affects is not consistent among the modeling studies. Other inconsistencies among the modeling studies, such as the role of SLHF, are expected given the vastly different idealized setups in which the models were run, and the resulting phase changes between low-level winds and convection. The decomposition of zonal advection processes into eddy and mean components has not indicated any clearly dominant process. In contrast, it has been consistently demonstrated

that the meridional advection term acts primarily through the modulation of synoptic-scale eddies (Maloney 2009; Maloney et al. 2010; Kiranmayi and Maloney 2011; Andersen and Kuang 2012), reducing their activity and corresponding drying to the east of the convective center and enhancing their activity and drying to the west.

The consistent importance, in both reanalysis and modeling studies, of modulation of synoptic scale eddies affecting meridional advection suggests that this process is a fundamental part of the real world observed MJO. Yet the ability of Maloney et al. (2010) to produce robust MJO-like ISV with this process largely removed suggests it may not be a critical to the existence of MJO-like ISV. Realistic MJO-like ISV has developed in models with mean state conditions varying from low-level mean state easterlies and zonally symmetric SST to low-level mean state westerlies with a greatly reduced meridional SST gradient. In all cases, this MJO-like ISV meets the fundamental criteria of a moisture mode, in that MSE anomalies are to 1st order q anomalies, and the distribution of moisture is closely linked to the distribution of diabatic heating.

The ability to produce realistic MJO-like ISV with moisture mode characteristics in such vastly different idealized conditions through unique combinations of processes poses fundamental questions. If the observed MJO is a moisture mode, is it really unique as a large-scale moisture mode, or are there numerous large-scale MJO-like moisture modes that can exist given a range of basic state conditions? If MJO-like ISV exists with basic state conditions that differ from those observed, is it accurate to consider that ISV an MJO? If so, are there processes common to the various forms of MJO-like ISV that can be considered critical to the MJO? Answers to these questions may provide insight to what the affects basic state changes due to ENSO or climate change may have on the MJO.

1.6. Winter Mean Low-Level Winds and Free Tropospheric Moisture

As previously discussed, several modeling studies have demonstrated that the mean state winds and moisture distribution fundamentally affect the development of ISV. Mean state winds also play a central role in theories such as WISHE, and observations have shown that MJO activity maximizes in regions of westerly mean state wind. Therefore, a brief discussion of the winter mean state winds and moisture distribution is in order. Figure 1.2 shows ERA-Interim mean winter (October 1 to April 30) winds at 850 hPa and specific humidity averaged from 850 to 500 hPa (hereafter denoted $q_{850,500}$). Notable features include a positive moisture gradient from the western Indian ocean to approximately the date line, a negative moisture gradient east of the date line and a ubiquitous negative equator to pole moisture gradient. The zonal moisture gradient is greatly reduced poleward of $\sim 7.5°$. Also note that while mean low level westerly winds are present from approximately 2.5°N to 7.5°S in the eastern hemisphere, poleward of these latitudes mean low level winds are easterly. Mean low level winds are easterly everywhere outside of the eastern hemisphere, with the transition from mean low level westerlies to easterlies occurring near the date line. With the exception of the Arabian Sea, there is relatively little meridional component in the mean state winds in the region of 15°N to 15°S.

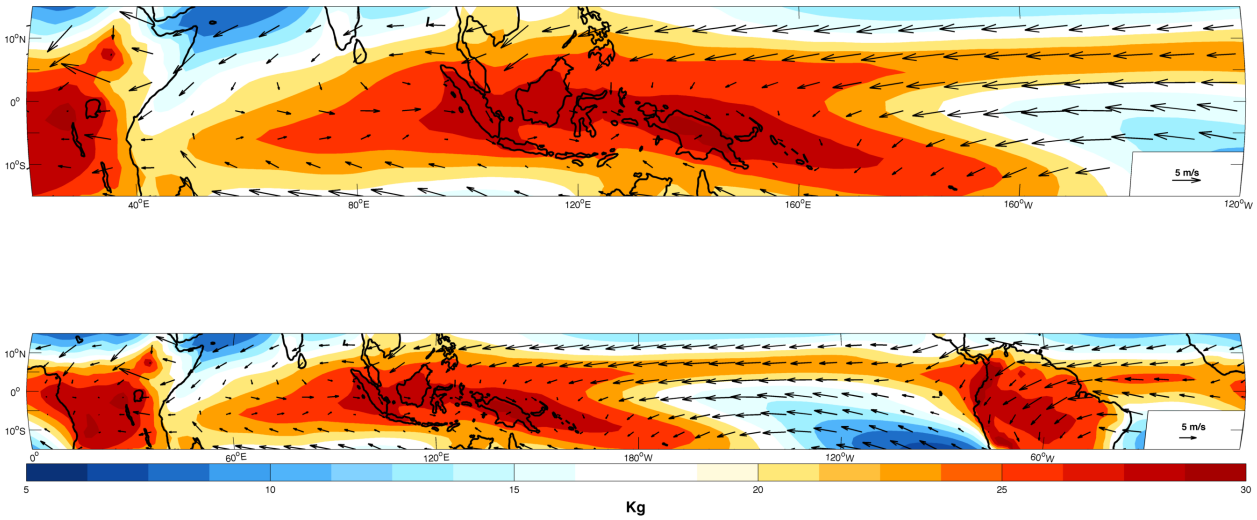

FIG. 1.2. ERAi mean $q_{850,500}$ (color contours) and 850 hPa horizontal for 1981-2011 winters (October 1 - April 30). Reference wind vectors are provided in the lower right corner of both panels.

1.7. MJO DIAGNOSTICS

Basic requisites of any useful index are that it captures the salient features of the MJO while meeting essential needs of the user. The immense complexity and pervasive nature of the MJO, combined with the current lack of understanding of the physical mechanism(s) responsible for its destabilization, maintenance and propagation, make assessment of the first requirement largely a matter of personal perspective. The wide array of MJO-related research makes it no easier to define a base set of essential user needs that must be met. While the forecast community requires real-time assessment, a researcher studying tropopause dynamics may need to efficiently sift through decades of data looking for convective or upper-level wind signals. In contrast, knowledge of low-level winds may be of primary interest for someone studying surface fluxes. Extensive datasets, and a wide range of mathematical techniques with which to interpret them, has allowed for the creation of as many indices as there are user needs and perspectives of the MJO.

Given our current understanding of the MJO, the abundance of suitable indices certainly has the benefit of promoting research along different theoretical lines. Yet this abundance creates difficulties. Large field campaigns have difficulty choosing a single index suitable for the wide range of user groups, yet using multiple indices means users groups may not even agree on the number of events observed during the field campaign. The prevalence of so many different indices in the literature makes gaining a true understanding and valuable assessment of the related research difficult, and makes the comparison of results challenging.

Most of the various MJO indices in use today can be generalized as being based on some variation of a filtering technique, EOF/PC based method, or combination of the two. The advantages and disadvantages of each technique will be briefly discussed.

1.7.1. EOF/PC Based Methodology

Perhaps the most commonly used MJO index is the Realtime Multivariate MJO (RMM) index, originally introduced by Wheeler and Hendon (2004). Other EOF/PC based methods that are commonly used follow a similar construction to that of the RMM, and have similar advantages and disadvantages. Calculation of the RMM index involves the application of combined EOF (CEOF) analysis to 15°N-15°S averaged OLR and zonal winds at 850 and 200 hPa (hereafter U850 and U200 respectively). The combined structure of the CEOF is effective at removing higher frequency variability (Wheeler and Hendon 2004), although Rossby-waves and other convectively coupled waves retain some ability to project onto the index (Roundy et al. 2009). Removing the previous 120-day running mean from all fields prior to calculation effectively limits the influence of interannual variability (Lin et al. 2008).

One of the main advantages of the RMM index is its real-time availability. It is also user friendly, being relatively easy to calculate and understand, and provides a visually intuitive

one-stop figure that indicates the estimated strength of the MJO and approximate location of enhanced convection. The RMM is, to a limited extent, influenced by both circulation and convective anomalies, meaning that it assesses the multi-field structure of the MJO.

Recent work by Straub (2013) has highlighted several of the major disadvantages of the RMM index. The three fields used to create the EEOF do not have equal influence in determining the magnitude and phase of the RMM index, with U200 having the dominant influence. It has been argued that this makes the RMM index poorly suited for investigating processes such as initiation (Straub 2013). In addition, the index does not provide a precise location of the enhanced convective phase, or even indicate if one is present. This has several major implications. First, it limits the ability to compare data at different locations relative to some part of the MJO lifecycle. A consequence of this is that researchers often determine a reference Day 0 based on some local measure of convection, which is not entirely appropriate. Another disadvantage of the RMM occurs when compositing a large number of events, when detailed inspection of each is not practical. Events where wind anomalies remote to the location of interest project onto the index in a manner that indicates enhanced convection in the location of interest are likely to be included in such a composite. Compositing such events together can lower the signal to noise ratio in phenomena of interest, potentially hindering the detection of processes such as those involved with initiation.

1.7.2. Wavenumber-Frequency Filtering

First introduced by Wheeler and Kiladis (1999), the technique of filtering a given field within wavenumber-frequency space, to a region that approximately encompasses the spectral peak of the MJO, is likely the most frequently used filtering technique at present. For instance, this could involve filtering precipitation or OLR within the approximate range of

eastward wavenumbers 0 to 5 and periods of roughly 30 to 96 days (Kiladis et al. 2005). In addition to looking at the characteristics of this filtered variability, days where values of this filtered field exceed some threshold locally can be used as reference Day 0.

Although this method has been used to great success (Kiladis et al. 2005, 2009), it does have some notable limitations. Filtering precludes the application of this method for any real-time assessment. It also retains other forms of ISV that fall within the same spectral window. Perhaps the largest limitation is the inherent assumption that an index made from knowledge of a single variable can provide accurate assessment of a phenomena as complex as the MJO. Wind-only and convection-only indices frequently provide very different assessments of the strength of MJO events, to the extent that some events that appear strong on one index completely fail to register on another (Straub 2013).

1.8. MJO Initiation

Convective initiation of the MJO has been theorized to be forced by mechanisms of both tropical and extratropical origin. Theories based on extratropical forcing are often related to organization of tropical convection by extratropical Rossby waves (Kiladis and Weickmann 1992; Matthews and Kiladis 1999) or baroclinic disturbances (Hoskins and Yang 2000). Theories on tropical forcing include both local and remote mechanisms. Local mechanisms such as cloud-radiative feedbacks (Hu and Randall 1994) and forcing by SST anomalies (Woolnough et al. 2001) have been proposed. Remote mechanisms involve either a upstream forcing by a circumnavigating signal associated with a prior MJO (Matthews 2008), or a downstream mechanism driven by the opposite phase of the MJO (Zhao et al. 2013). This study does not aim to test these theories, or put forward a new one, but instead to extend the analysis of precursor signals present prior to convective initiation. As such, the following

review will be limited to a discussion of precursor signals observed in the studies of Matthews (2008), Straub (2013) and Zhao et al. (2013)

Matthews (2008) found that while MJO events most often initiated in the Indian Ocean, more than half identified in the study initiated in regions spanning the maritime continent to the west Pacific. About 40% of the events identified were thought to be "primary", having no associated precursor event, as in "successive" events. Both Matthews (2008) and Straub (2013) identified a stationary region of suppressed convection that developed in situ over the Indian Ocean 25 to 15 days prior to primary initiation. Both studies also found that easterly(westerly) U850(U200) wind anomalies developed over the Indian Ocean during this time, slowly strengthening and expanding in zonal extent. Straub (2013) found that these anomalies developed in the absence of a convective anomaly and began propagating eastward into the western Pacific well before the onset of convection in the Indian Ocean. Zhao et al. (2013) found similar dynamical signals in a study of successive events, and noted a marked increase in lower tropospheric specific humidity and temperature beginning 10 days before convective initiation. Moisture budget and temperature budget analysis showed that changes in MSE in the initiation region were mostly due to changes in column integrated moisture content. This build up of moisture was found to be dominated by the advection of mean state moisture by anomalous winds associated with the MJO. Zhao et al. (2013) concluded the this buildup of moisture was associated with the downstream Rossby-wave like dynamical response to suppressed convection over the maritime continent and western Pacific, and was not the result of a circumnavigating dynamical signal.

1.9. Study Outline

This study aims to identify and explain processes that control the development, maintenance and propagation of $\langle h \rangle$ and $\langle q \rangle$ anomalies associated with the MJO. This is done by implementing novel diagnostics to analyze the column integrated MSE budget of the MJO. Definitions of these diagnostics are provided in Section 2, along with descriptions of the various datasets and methods used in this study. Section 3 first looks at the geographical variability of the various processes affecting $\langle h \rangle$ and $\langle q \rangle$ anomalies. Composite MSE budgets of the Indian Ocean and convective initiation over the western Indian Ocean are then presented. Section 4 provides a discussion of the main findings of the study.

CHAPTER 2

Data and Methodology

2.1. Data

2.1.1. ERA-Interim

The European Center for Medium-Range Weather Forecasts (ECMWF) has produced several global atmospheric reanalysis products, the most recent of which is ERA-Interim. ERA-Interim is produced with a forecast model that has fully coupled atmosphere, land surface and ocean wave components (Dee et al. 2011). The ERA-Interim atmospheric model has 60 model layers in the vertical and a spectral T255 horizontal resolution, corresponding to $\sim$ 80 km spacing on a reduced Gaussian grid. In addition to its increased resolution, ERA-Interim boasts several advancements over its predecessor ERA-40. These include an improved hydrologic cycle, more realistic stratospheric circulation, and better observation bias correction (Dee et al. 2011). ERA-Interim is currently available from 1979 to present, and is the primary dataset utilized in this study. All fields were obtained with 6-hour temporal resolution and $1.5^\circ \times 1.5^\circ$ spatial resolution.

2.1.2. NOAA Interpolated OLR

NOAA Interpolated OLR is an observational data product resulting from the spatial and temporal interpolation of OLR data from the NCAR archives (Liebmann and Smith 1996). Daily values are available from 1974 to present in $2.5^\circ \times 2.5^\circ$ spatial resolution. These data were then spatially interpolated to a $1.5^\circ \times 1.5^\circ$ grid corresponding to ERA-Interim data, and used to verify results relating to ERA-Interim OLR.

2.1.3. SeaFlux SLHF

High-resolution satellite based estimates of SLHF are available from 1998 to 2007 as part of the SeaFlux Turbulent Flux Dataset version 1.0. These data were obtained for the years 2000 to 2007, with $0.25^\circ \times 0.25^\circ$ spatial and 3-hourly temporal resolution. They were then interpolated temporally to daily values and spatially to a $1.5^\circ \times 1.5^\circ$ grid corresponding to ERA-Interim data. These data were then used to verify results relating to ERA-Interim SLHF. Further documentation of the SeaFlux Turbulent Flux Dataset is available at www.seaflux.org.

2.1.4. TRMM Precipitation

Combined-sensor precipitation estimates are available from 1998 to present at 3-hourly temporal and $0.25^\circ \times 0.25^\circ$ spatial resolution as part of the Tropical Rainfall Measuring Mission (TRMM) (Cite Huffman et al, 2007). This merged product includes data from GMS, GOES-E, GOES-W, Meteosat-7, Meteosat-5 and NOAA-12. Data were obtained for the years 2000 to 2009 and then interpolated temporally to daily values and spatially to a $1.5^\circ \times 1.5^\circ$ grid corresponding to ERA-Interim data. These data are used to demonstrate the effectiveness of some of the methods described below.

2.2. Methodology

2.2.1. Calculation of CEOFs and PCs

ERA-Interim specific humidity integrated from 850 to 500 hPa (hereafter $q_{850,500}$), OLR, and zonal wind at 850 and 200 hPa (hereafter U850 and U200 respectively) were used to calculate the CEOF structure. The method used to construct the CEOF is similar to that of Wheeler and Hendon (2004), and was chosen because of its relative simplicity, potential

for real time application and likely familiarity to the reader. It differs in construction from Wheeler and Hendon (2004) in that it is a 2-D CEOF analysis and includes a fourth variable, $q_{850,500}$. This construction has been chosen because it allows certain features of the new diagnostics to be demonstrated, and also because $q_{850,500}$ is a key variable in moisture mode theory and its inclusion in the CEOF structure allows for a "process-oriented" approach to the application of the new diagnostics. All fields were limited spatially to 15°N from 15°S and to the time period of 1979-2010. The time mean and first three harmonics of the annual cycle were removed from each field at each grid point in order to remove the influence of the seasonal cycle. Removal of interannual variability was accomplished by removal of the previous 120-day mean from each field at each grid point. Each field is then weighted by the square root of the cosine of latitude, and divided by its global standard deviation to ensure that each field contributes equally to the variance of the combined vector. Eigenanalysis was then performed on the covariance matrix combined field vector, where latitude and longitude have been rearranged to make up a single spatial dimension. The first two CEOF structures were chosen to represent the MJO. Two sets of PCs were then calculated. This first set was calculated by projecting the combined field vectors onto the first two CEOF structures in order to calculate the values of PC1 and PC2 respectively. The second set of PCs were calculate by bandpass filtering the combined field vectors to 20-100 days before their projection onto the first two CEOF structures.

2.2.2. Diagnostics

CEOF1 and CEOF2 are, by construction, orthogonal. Therefore PC1 and PC2 can be used to define a 2 dimensional phase space, and a index vector can be defined within in that

phase space such that its amplitude and phase are given by:

$$\text{amplitude} = \sqrt{PC1^2 + PC2^2} \tag{2.1}$$

$$\text{phase} = \tan^{-1}\left(\frac{PC2}{PC1}\right) \tag{2.2}$$

Traditionally the value of a PC is calculated by multiplying the data by the CEOF spatial structure. It is just as valid to calculate the PC value as the sum of its individual component PCs, which are themselves calculated by multiplying subsets of the data used to calculate the PCs by corresponding subset regions of the CEOFs (see figure here). The ability to deconstruct PCs into component PCs can be leveraged in PC1/PC2 phase space using vector calculus, allowing various properties of the fields used to construct the CEOFs, and their relationships to each other, to be calculated. Remember, for arbitrary vectors $\vec{A}$ and $\vec{B}$

$$\|\vec{A}\| = \sqrt{\left\langle \vec{A}, \vec{A} \right\rangle}$$

is the norm,

$$\cos\theta = \frac{\left\langle \vec{A}, \vec{B} \right\rangle}{\|\vec{A}\|\|\vec{B}\|}$$

where θ is the angle between the two vectors, and

$$\vec{A}_{\vec{B}} = \|\vec{A}\|\cos\theta = \frac{\left\langle \vec{A}, \vec{B} \right\rangle}{\|\vec{B}\|}$$

is the scalar projection of $\vec{A}$ onto $\vec{B}$.

Calculations of the following diagnostics are generalized to be applicable to any index calculated from a pair of CEOFs/PCs containing J fields with K grid points, such that

$$\begin{aligned}\overrightarrow{\text{Index}} &= (PC1, PC2) \\ &= \left(\sum_{j=1}^{J} fPC1_j \, , \sum_{j=1}^{J} fPC2_j\right) \\ &= \left(\sum_{j=1}^{J}\sum_{k=1}^{K} gpPC1_{j,k} \, , \sum_{j=1}^{J}\sum_{k=1}^{K} gpPC2_{j,k}\right)\end{aligned}$$

Here $fPC1_j$ and $fPC2_j$ correspond to the PC values of the jth field in the CEOF structure and $gpPC1_{j,k}$ and $gpPC2_{j,k}$ correspond to the PC values of the kth grid point in the jth field in the CEOF structure. PCs associated with an individual field are preceded with a letter f, and PCs associated with an individual grid point are preceded by the letters gp. This notation has been introduced to help distinguish diagnostics calculated from an individual field from those calculated from an individual grid point in subsequent sections. Vectors in PC1/PC2 phase space can be defined for each field and grid point such that

$$\overrightarrow{fPC_j} = (fPC1_j, fPC2_j)$$

$$\overrightarrow{gpPC_{j.k}} = (gpPC1_{j.k}, gpPC2_{j,k})$$

Please note that field PC vectors are functions of both time and field, and grid point PC vectors are functions of time, space and field. Illustrations to aide visualization of the following diagnostics are presented in Figures 2.1 and 2.2 below.

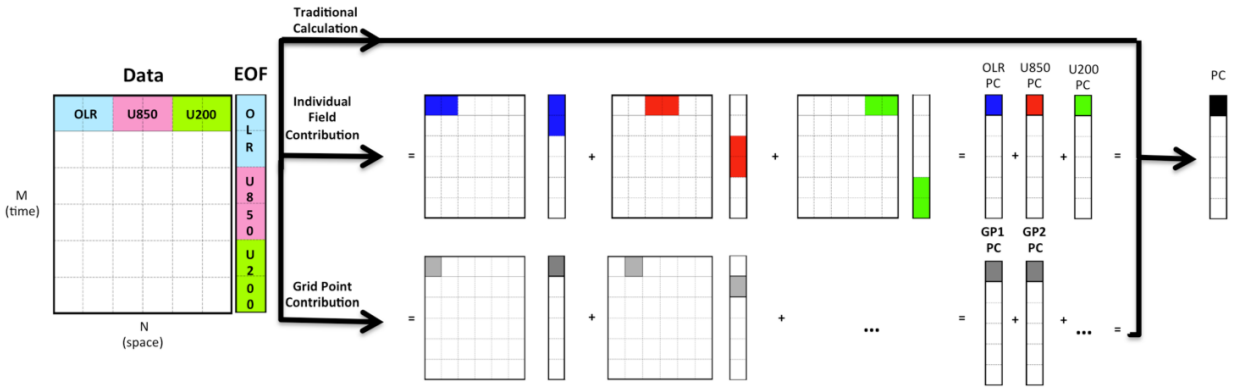

FIG. 2.1. An illustration of how the PCs used in various diagnostics introduced in this study are calculated. In this example, a CEOF composed of OLR, U850 and U200 is used. The traditional calculation (top) of a PC, the calculation of an individual field PC (middle), and the calculation of the PC for a single grid point of a single field (bottom) are illustrated here.

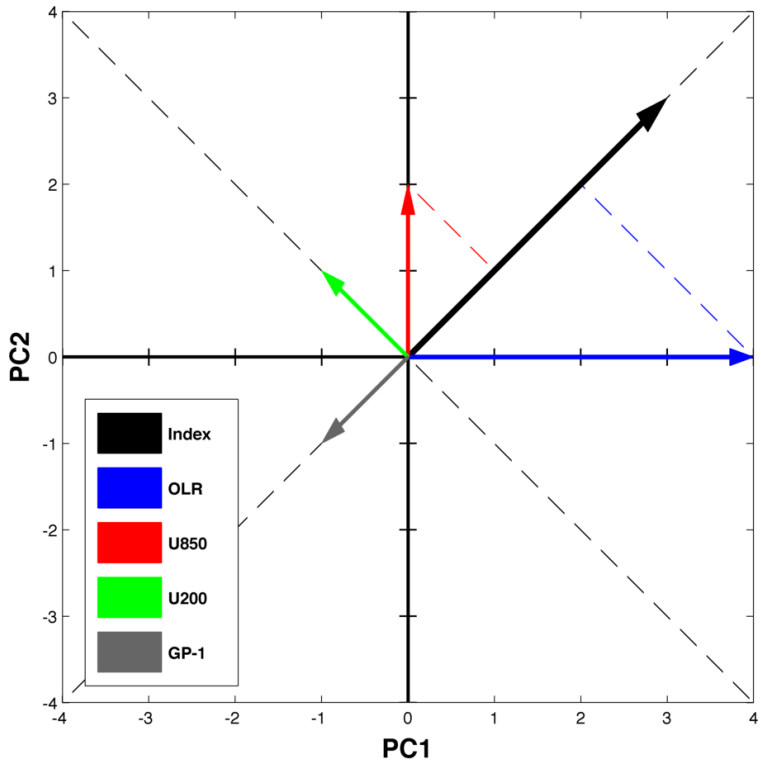

FIG. 2.2. An illustration of how various vectors may be used in PC1/PC2 phase space to calculate some of the diagnostics in this study. The vectors of individual fields (denoted here as OLR, U850, and U200) can be projected onto the index vector to obtain their individual field contributions. A similar process can be used to calculate the grid point contribution of a single grid point of an individual field (represented here by the GP-1 vector).

2.2.2.1. Individual Field Contribution

The contribution of the jth field to the overall amplitude of the index vector is simply the projection of that field vector onto the index vector. In PC units this is

$$\text{Field Contribution} = \overrightarrow{fPC_j}_{\overrightarrow{\text{Index}}} \tag{2.3}$$

or, dividing by the index amplitude

$$\text{scaled Field Contribution} = \frac{\overrightarrow{fPC_j}_{\overrightarrow{\text{Index}}}}{\|\overrightarrow{\text{Index}}\|} = \frac{\left\langle \overrightarrow{fPC_j}\,, \overrightarrow{\text{Index}} \right\rangle}{\|\overrightarrow{\text{Index}}\|^2} \tag{2.4}$$

results in units of percent contribution to total index amplitude.

2.2.2.2. Grid Point Phase

The ratio of the values of the first two CEOF structures at any spatial location, or grid point, is fixed. This means that any data projected onto these CEOF structures during the calculation of the PC values produces the same ratio of PC2 to PC1 at each location. In other words, each grid point of each field has a fixed phase in PC1/PC2 phase space, given by

$$\text{Grid Point Phase} = \tan^{-1}\left(\frac{CEOF2_{j,k}}{CEOF1_{j,k}}\right) = \phi \tag{2.5}$$

where $CEOF1_{j,k}$ and $CEOF2_{j,k}$ are the values of the first two CEOF structures at the kth grid point of the jth field. While the ratio of PC2 to PC1 is fixed, the data projected onto the CEOF structures may be either positive or negative and vary in amplitude, determining the amplitude of the resultant grid point vector and whether it projects positively or negatively (180° away from) along the grid point phase.

2.2.2.3. Grid Point Contribution

Just as the contribution of a single field to the overall amplitude of the index is simply the projection of that field vector onto the index vector, the contribution of a single grid point of a single field to the overall amplitude of the index is simply the projection of the grid point vector onto the index vector. In PC units this is

$$\text{Grid Point Contribution} = \overrightarrow{gpPC_{j,k}}_{\overrightarrow{\text{Index}}} \tag{2.6}$$

or, dividing by the index amplitude

$$\text{scaled Grid Point Contribution} = \frac{\overrightarrow{gpPC_{j,k}}_{\overrightarrow{\text{Index}}}}{\|\overrightarrow{\text{Index}}\|} = \frac{\left\langle \overrightarrow{gpPC_{j,k}}, \overrightarrow{\text{Index}} \right\rangle}{\|\overrightarrow{\text{Index}}\|^2} \tag{2.7}$$

results in units of percent contribution to total index amplitude.

2.2.2.4. Relative Phase

Transition through 360° of phase in PC1/PC2 phase space represents a full lifecycle of the MJO. If the phase of the index is known, the grid point phase can be used to determine what stage of the MJO lifecycle of a given field is occurring at each location. The stage in the MJO lifecycle of a given variable at each location is given by:

$$\begin{aligned} \text{relative phase} &= \text{index phase} - \text{grid point phase} && (2.8) \\ &= \tan^{-1}\left(\frac{PC2}{PC1}\right) - \tan^{-1}\left(\frac{CEOF2_{j,k}}{CEOF1_{j,k}}\right) && (2.9) \end{aligned}$$

A brief example can highlight how this diagnostic works. Suppose U850 at a given grid point has and CEOF2 value of 1 and CEOF1 value of 1. This means that the grid point phase of

U850 is 45°, and a positive anomaly of U850 projects such that the grid point vector has a phase of 45° in PC1/PC2 phase space. Therefore the CEOF structure has determined that a positive U850 anomaly contributes maximally to the index amplitude when the index phase is 45°, a negative U850 anomaly contributes maximally to the index amplitude when the index phase is 225°, and an anomaly of either sign plays no role in determining the index amplitude when the index phase is 135° or 315°. This is a very powerful tool, as it allows for the compositing and comparison of data from different locations relative to a lifecycle of the MJO in a given field.

2.2.2.5. Phase Activity

As previously stated, any subset of grid points in the CEOF structure can be combined to form a component vector of the full index vector, which can then be projected onto the full index vector to assess its contribution to the amplitude of the index. This is equivalent to summing the grid point contribution of each of the individual grid points used to make the component vector. Creating component vectors out of grid points in the CEOF structure within a phase range for each variable then allows the contribution of each phase of each variable to the amplitude of the index to be assessed. The measure of the contribution by a phase range of a given variable to the amplitude of the index is given by

$$\text{Phase Activity}(\phi_2 - \phi_1) = \overrightarrow{component}(\phi_2 - \phi_1)_{\overrightarrow{\text{Index}}} \tag{2.10}$$

$$= \sum_{n=1}^{N} \overrightarrow{gpPC_{j,n}}_{\overrightarrow{\text{Index}}} \tag{2.11}$$

where $(\phi_2 - \phi_1)$ gives the range of grid point phase that the phase activity is measured over, and n is the index of N grid points located within that phase range. Again, dividing by the

index amplitude gives units of percent contribution to index amplitude such that

$$\text{scaled Phase Activity}(\phi_2 - \phi_1) = \frac{\text{Phase Activity}}{\|\overrightarrow{\text{Index}}\|} \tag{2.12}$$

$$= \frac{\sum_{n=1}^{N} \overrightarrow{gpPC_{j,n}}_{\overrightarrow{\text{Index}}}}{\|\overrightarrow{\text{Index}}\|} \tag{2.13}$$

2.2.3. Box-Cox Transformation

Calculating the amplitude of an index based on its leading PC values results in a distribution that is positively skewed. In order to standardize the amplitude values appropriately, a power transformation can be used. The transformation has the form:

$$y(\nu) = \begin{cases} \frac{y^{\nu}-1}{\nu} & \text{if } \nu \neq 0 \\ \ln(\nu) & \text{if } \nu = 0 \end{cases} \tag{2.14}$$

where ν is chosen iteratively using the Box-Cox method (Olivier and Norberg 2010). This involves choosing a ν value that ensures the best transformation to a normal distribution, where "best" is determined by maximizing the R^2 value of the sorted transformed data regressed against a sorted inverse normal distribution. The power transformation can then be reversed in order to determine what amplitude of the index corresponds to statistically significant values from the normally distributed transformed data. This method is demonstrated in the results section, but in order to maintain consistency with previous work, the remainder of the results are presented using the traditional calculation of index amplitude.

2.2.4. Spectral Analysis

Power spectra and cross-spectra were computed for PCs calculated from daily data subjected to the same pretreatment as was performed in the calculation of the CEOF. While PCs calculated from 20-100 day bandpass data are used in the MSE budget analysis, scrutiny of the power spectra and cross-spectra of the PCs calculated from daily data is one method of assessing the fidelity of the CEOF in isolating the MJO signal. The daily data was limited to the months of October to April, and then subset into 33 winter seasons. A Hann window was applied to each subset of data before application of the FFT. Power spectra were computed for each subset, and then averaged together. This averaged power spectra was used to compute the cross-spectra. The statistical significance of spectral peaks were assessed using an a priori F-Statistic test at the 0.95 significance level. This was done by comparing the observed spectral peaks to the power spectrum of red noise calculated from the lag-1 autocorrelation. One potential criticism of the aforementioned process is that, due to limitations imposed by subsetting, the influence of interannual variability on the index is not assessed. It is assumed that removal of the previous 120-day mean addressed this concern, consistent with Lin et al. (2008).

2.2.5. MSE Budget Term Calculations

All MSE budget terms were first calculated in 6-hourly form and subsequently averaged to daily. All terms were vertically integrated from the surface to 100 hPa. Values from the layer nearest the surface pressure were used in the integration to surface pressure. Both horizontal and vertical winds were interpolated to grid cell edges for use in calculation of advective terms. All budget terms were correlated with the budget residual to ensure that there was no consistent relationship between them.

Components of the horizontal advection were decomposed into time mean and eddy components. Time mean components were defined as the 51-day running mean, meant to represent the average over the duration of an average MJO lifecycle. Eddy components were defined as deviations from the 51-day running mean. The contribution of high frequency variability to these terms was assessed by applying a 20 day high-pass filter to eddy components before the calculation of the various budget terms, which were then bandpass filtered to 20-100 days.

2.2.6. Time Filtering

In some instances time filtering was used to isolate intraseasonal signals of physical interest. A 20-100 day Butterworth Bandpass filter was applied to all MSE budget terms, as well as the dynamical fields projected onto CEOF structures to calculate corresponding PC's. After application of the filter, data was limited to October 1, 1981 - April 30, 2011. These MSE budget terms and PCs will subsequently be referred to as filtered MSE budget terms and filtered PCs respectively. MSE budget terms and PCs not subjected to this treatment will subsequently be referred to as unfiltered MSE budget terms and unfiltered PCs respectively, although the dynamical fields used to compute the latter have had the seasonal cycle and previous 120-day mean removed.

2.2.7. Composite MSE Budgets

2.2.7.1. Relative Phase MSE Budget Term Composites

Bandpass filtered fields were used in the calculation of the PCs, and therefore in the calculation of the relative phase diagnostics. Days included in relative phase MSE budget term composites were chosen by first selecting all days where the relative phase for a grid

point was within 5° of the desired relative phase and then limiting these to days when the index amplitude was greater than 1. Days of the same relative phase that occurred more than 20 days apart were considered to be independent events. Little sensitivity was exhibited to reasonable changes in this threshold. These values were latitudinally averaged from 15°N-15°S for the latitudinally averaged composites, and over the region of 15°N-15°S,50°E-95°E for the composite Indian Ocean MSE budget.

2.2.7.2. Initiation Budgets

For reasons discussed in the results section, the initiation domain was chosen to be 4.5°N-4.5°S, 49.5°E-60°E. The GPC from negative OLR anomalies was calculated from unfiltered PCs, and a timeseries was made by averaging these values over the chosen domain. Peaks exceeding one standard deviation, and separated by at least 20 days were identified. Any peak where the index amplitude was below one, or fell below one in the subsequent 10 days, was excluded. A total of 39 peaks remained, which were chosen to be the "Day 0" of the initiation composites. Lag composites of both filtered and unfiltered MSE budget terms, OLR, and dynamical fields were made.

2.2.8. Scatterplots of MSE and Moisture Budget Terms

Several scatterplots of various MSE and moisture budget terms are presented in the results section. All terms were calculated using ERAi data from 1981-2011, and bandpass filtered to 20-100 days. Precipitation was calculated as $Q_2 + LH$ using the moisture budget terms. The various terms were averaged over the central Indian Ocean (4.5°N-4.5°S,70.5°E-79.5°E) during periods where the index amplitude exceeded a value of 1. Correlation analysis

was performed on each scatterplot, with significance being assessed using a two-tailed test at the 95% level.

2.2.9. Significance Testing

The Student's t-test was applied in several of the composite analyses to assess the significance of the results. The 95% confidence limits for the mean of each sample were assessed using:

$$\mu = \overline{x} \pm t_c \frac{s}{\sqrt{N-1}} \tag{2.15}$$

where $\overline{x}$ is the composite value at a particular spatial point, t_c is the critical t-statistic given the degrees of freedom and the confidence interval desired, s is the standard deviation of the sample used to calculate the composite value, and N is the number of independent samples. The value of t_c was chosen using the minimum number of independent samples included for any single point included in the composite, and therefore should be viewed as a conservative estimate of the statistical significance. As each composite was calculated from data in anomaly form, the composite value $\overline{x}$ was tested against a population mean of zero. If the confidence interval did not include zero the composite value was considered to be significant.

CHAPTER 3

Results

3.1. CEOF Results

The spatial structures of $q_{850,500}$, OLR, U850 and U200 in the leading two CEOFs are presented in Figures 3.1 and 3.2. Combined, the leading two CEOF structures explain 10.7% of the total variance of the original fields. The variance explained is lower than that of the latitudinally averaged CEOFs of Wheeler and Hendon (2004), but similar to the variance explained by their 2-D CEOFs. Based on the criteria of North et al. (1982) with an effective sample size of 64 (assuming a minimum of 2 events per year), the leading CEOF structures are considered well separated from CEOF 3 (Figure 3.3). Power spectra and cross-spectra of the leading PCs are shown in Figures 3.4 and 3.5 respectively. These PCs were calculated using data not subjected to bandpass filtering. The fraction of the total variance occurring within the 30 to 70 day band is 0.68 for both PCs, and clearly exceeds that expected of red noise at a statistical significance of 95%. Cross spectral analysis results show the leading PCs have an average coherence squared of 0.83 in the 30 to 70 day period range, with eastward propagation evidenced by PC1 leading PC2 by a quarter of a cycle. These results provide confidence that the leading CEOF structures effectively capture the structure of the MJO, and indicate the substantial influence of the MJO even in data not bandpass filtered to intraseasonal periods. The correlation with the RMM index is 0.83 during winter periods 1980 to 2012.

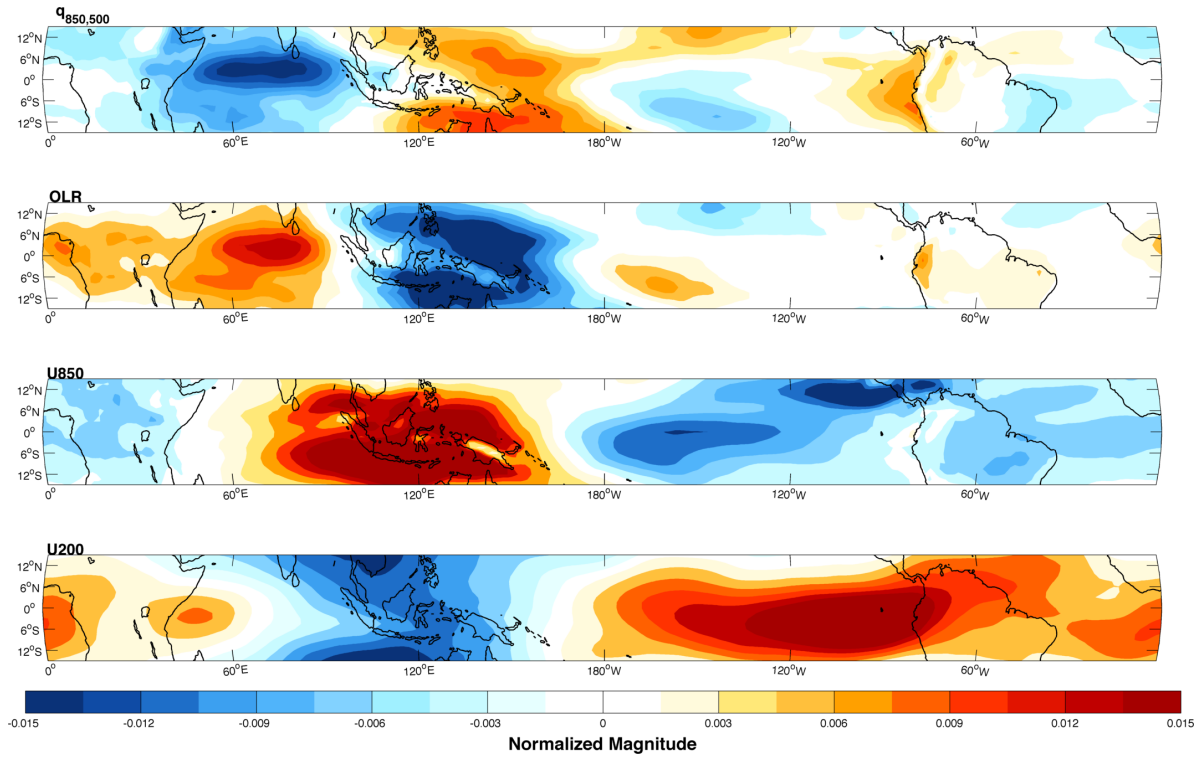

FIG. 3.1. First CEOF structure of ERAi $q_{850,500}$, OLR, U850 and U200 during winter months (October 1 to April 30) from 15°N-15°S.

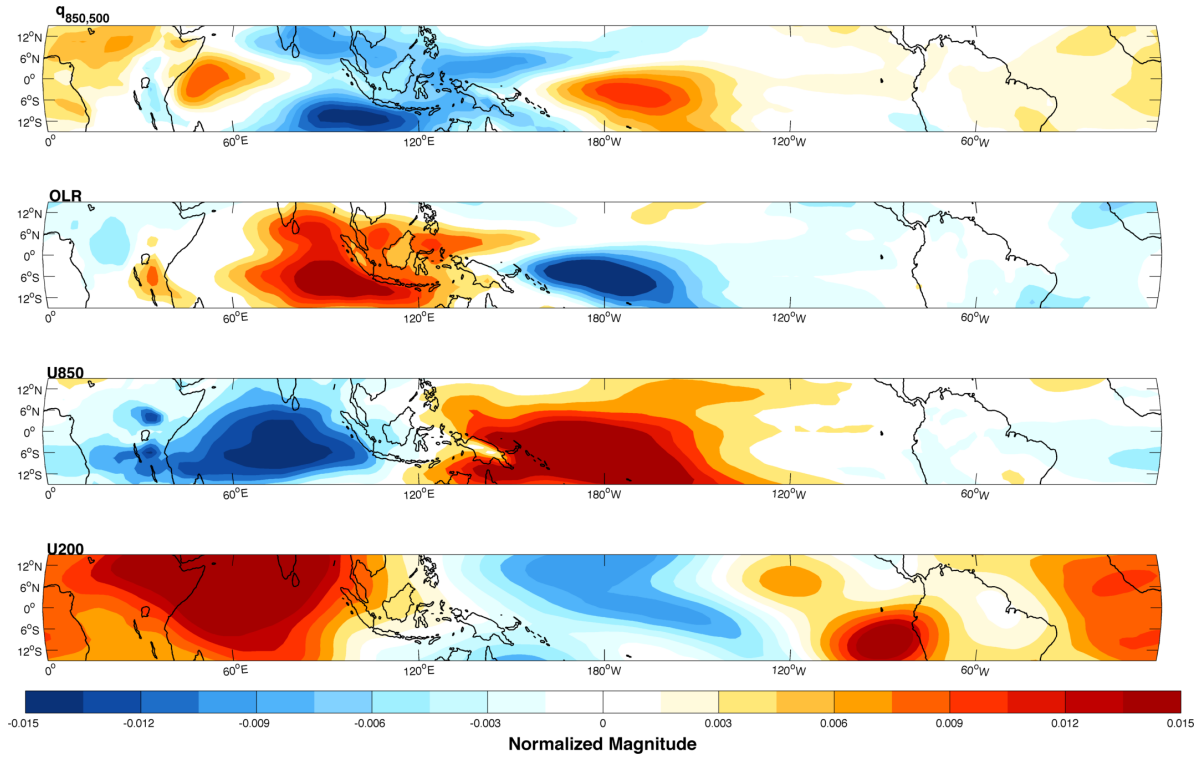

FIG. 3.2. As in Figure 3.1, except for CEOF2.

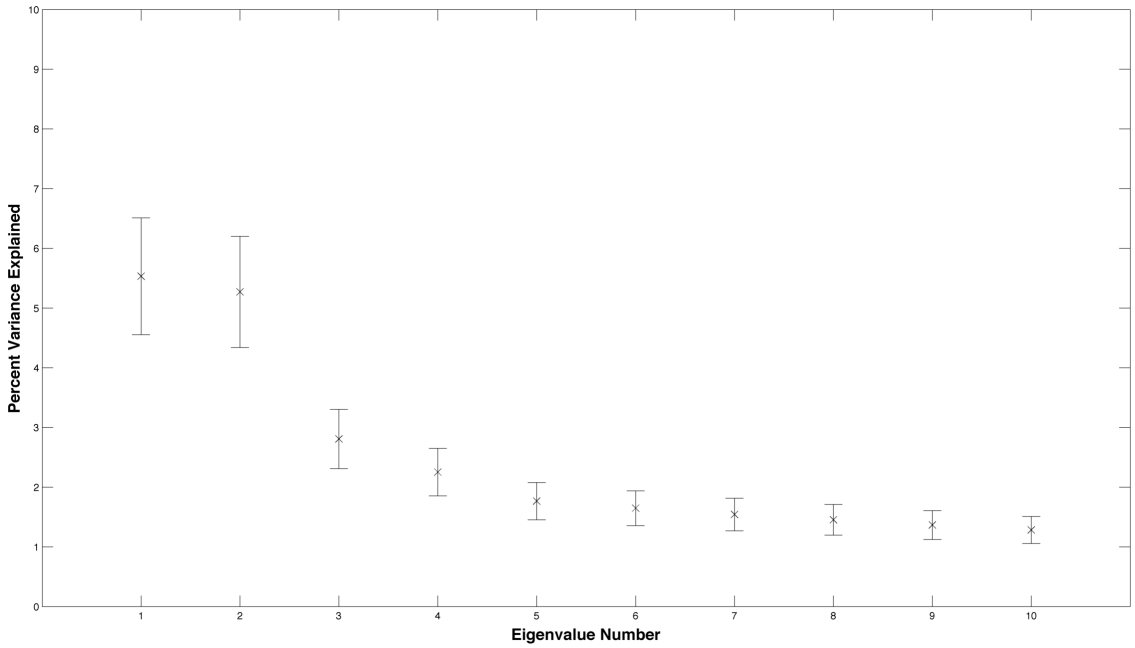

FIG. 3.3. Eigenvalue spectrum of the leading 10 CEOFs, with associated error bars. Errors bars were calculated as in North et al. (1982), assuming an effective sample size of 64.

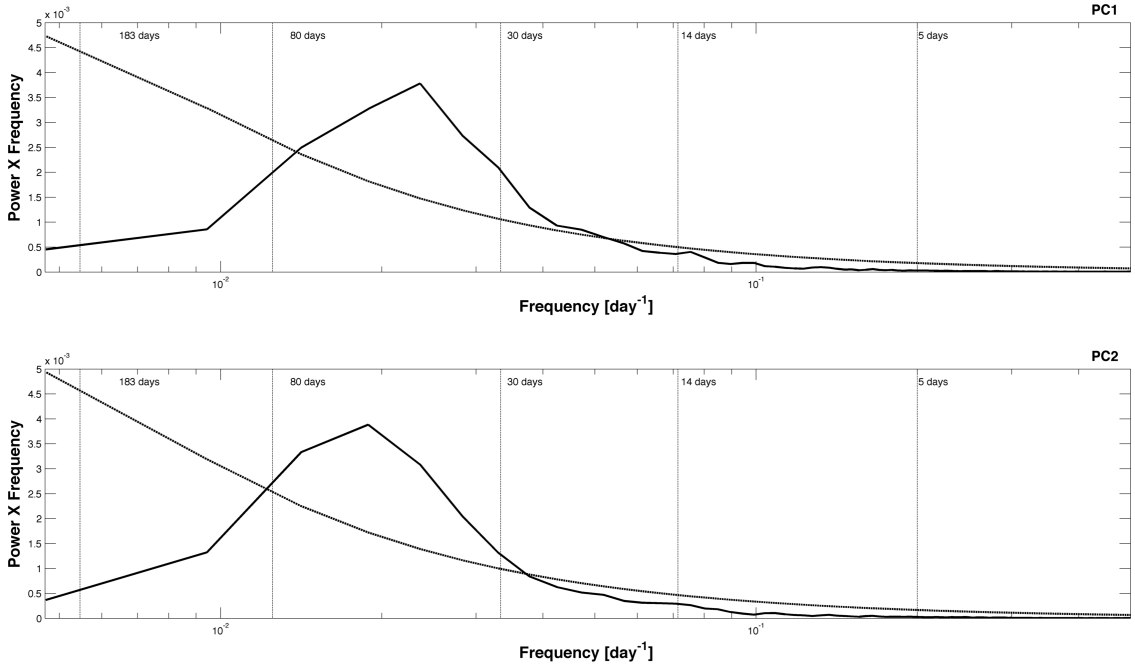

FIG. 3.4. Power spectra of the unfiltered PCs of the leading two CEOF structures. The dashed line indicates the threshold for exceeding the red-noise spectrum with a statistical significance of 95%. The area of each curve is scaled such that the area under the entire curve is equal to 1. The chosen plotting format is such that the area under the curve between two frequencies is proportional to the fraction of the variance that falls within that band.

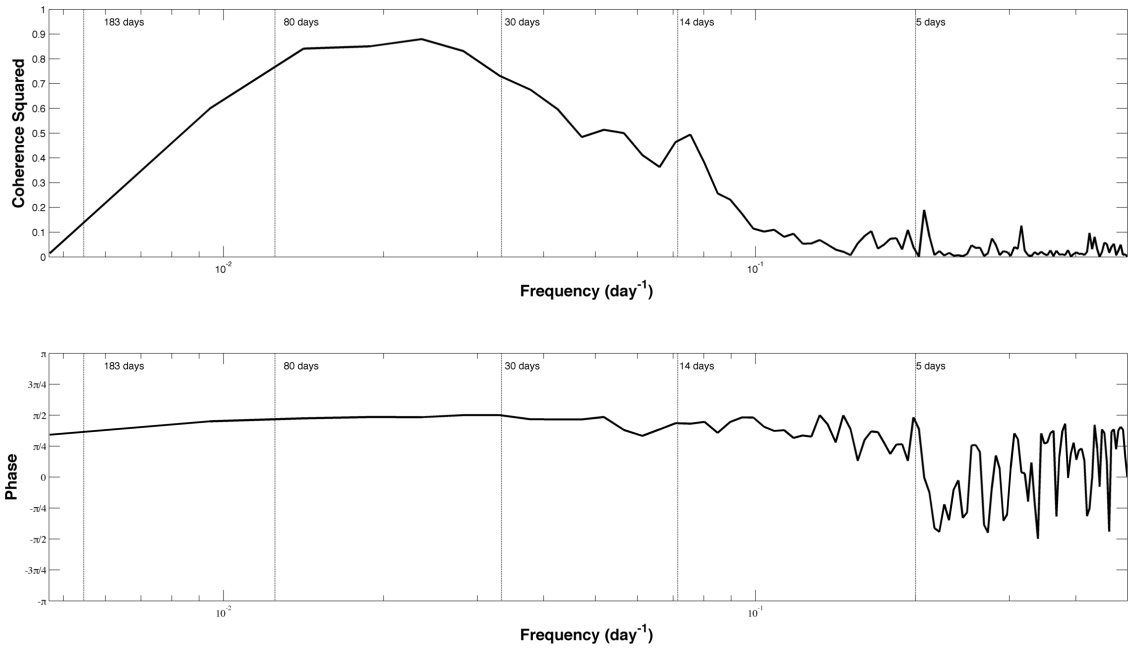

FIG. 3.5. Cross spectrum of PC1 and PC2, with coherence squared (phase) between PC1 and PC2 shown in the top(bottom) plot respectively. The 0.01% confidence level on the null hypothesis of no association is 0.212, and the leading PCs have an average coherence squared of 0.83 in the 30 to 70 day period range. A $\frac{\pi}{2}$ relationship means that PC1 leads PC2 by a quarter of a cycle.

The grid point phase (see equation 2.5) of each field included in the CEOF structures is presented in Figure 3.6. The grid point phase is determined by the ratio of CEOF2 to CEOF1 (Figures 3.1 and 3.2) at each location. The tendency for the grid point phase of any field to increase eastward indicates the eastward propagation of the MJO with increasing phase. Regions where MJO propagation is typically slow, such as the eastern hemisphere, exhibit a large range of grid point phase in a small geographical location. Regions where MJO propagation is typically fast, such as the western hemisphere, exhibit a small range of grid point phase in a large geographical location. The consistency with which the grid point phase evolves for any field within a region serves as an indication of the fidelity of the grid point phase for representing a real physical relation to the MJO. Clearly, regions exist where the grid point phase has no tangible connection to the evolution of field in question. These

regions typically correspond to regions where the CEOF structures have little amplitude, an indication of the lack of coherent MJO signal. An example of such a region is over the Andes Mountains of South America. Grid point phase compositing methods should not be applied in these regions.

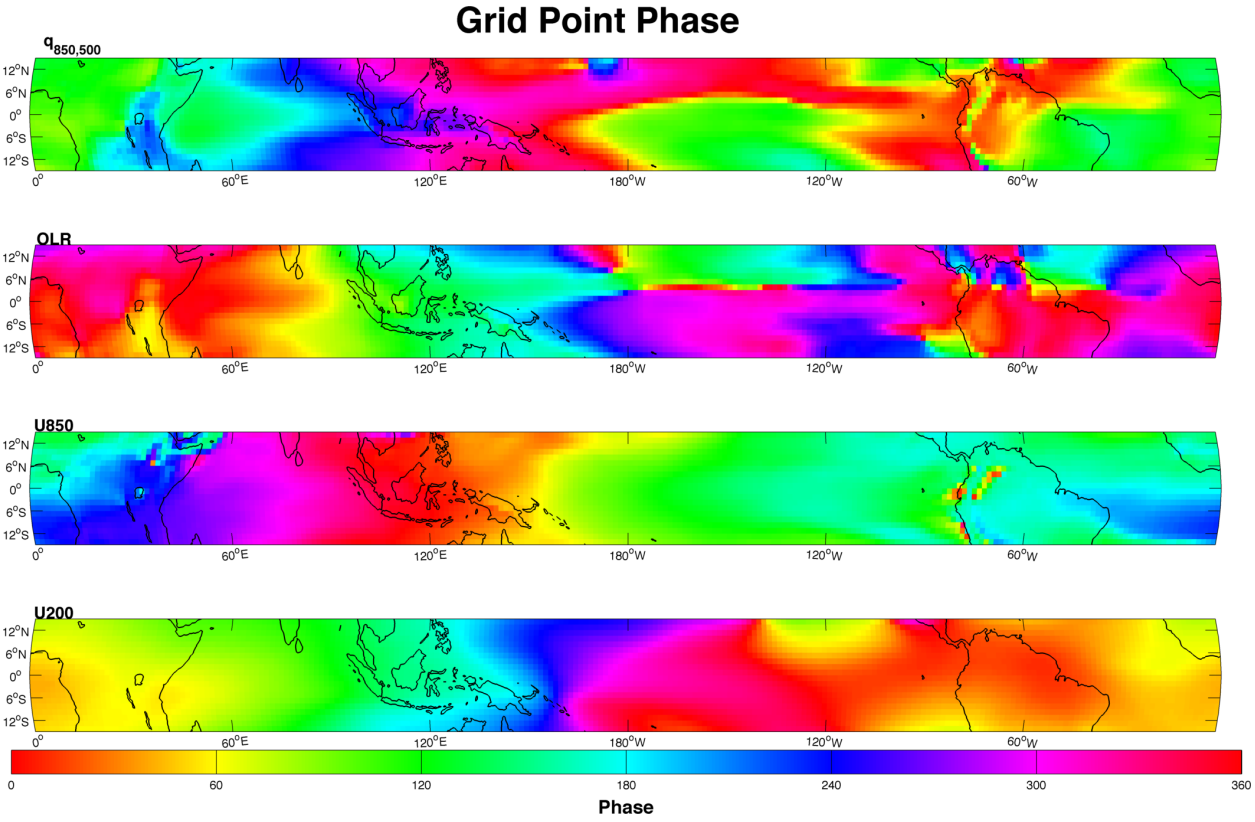

FIG. 3.6. Grid point phase of each variable used in the CEOF structure.

The relative influence of each field in determining the amplitude and phase of the index are indicated by their mean scaled field contributions (see equation 2.4). The index is disproportionately influenced by U200 and U850 , whose average scaled field contributions are 42.22% and 32.72% respectively. In contrast, OLR and $q_{850,500}$ have average scaled field contributions of 14.82% and 10.24%. This is consistent with the findings of Straub (2013) regarding the RMM index. The average scaled field contributions of each field are fairly insensitive to the period over which averaging is applied, remaining approximately constant

when the mean is taken only during periods where the index exceeds a value of 1, is less than 1, or over the whole record.

The geographical regions in which fields preferentially contribute to the amplitude and phase of the index can be assessed by looking at their mean scaled grid point contribution (see equation 2.7) (Figure 3.7). Inspection of Figure 3.8, which shows CEOF amplitude (see equation A.2) of each variable at each location, shows that mean grid point contribution of each field roughly coincides with the CEOF amplitude of that field at any location. The mean grid point contributions are approximately the same when averaged only over periods where the index exceeds a value of 1. The large influence of U200 in the westerly wind duct is immediately apparent. Each field plays a more equitable role in determining the index if the scaled field contributions are assessed only over the Indian ocean and western Pacific (60°E-180°E, 15°N-15°S). In this region $q_{850,500}$, OLR, U850 and U200 contribute approximately 12.51%, 28.84%, 35.68% and 22.97% respectively.

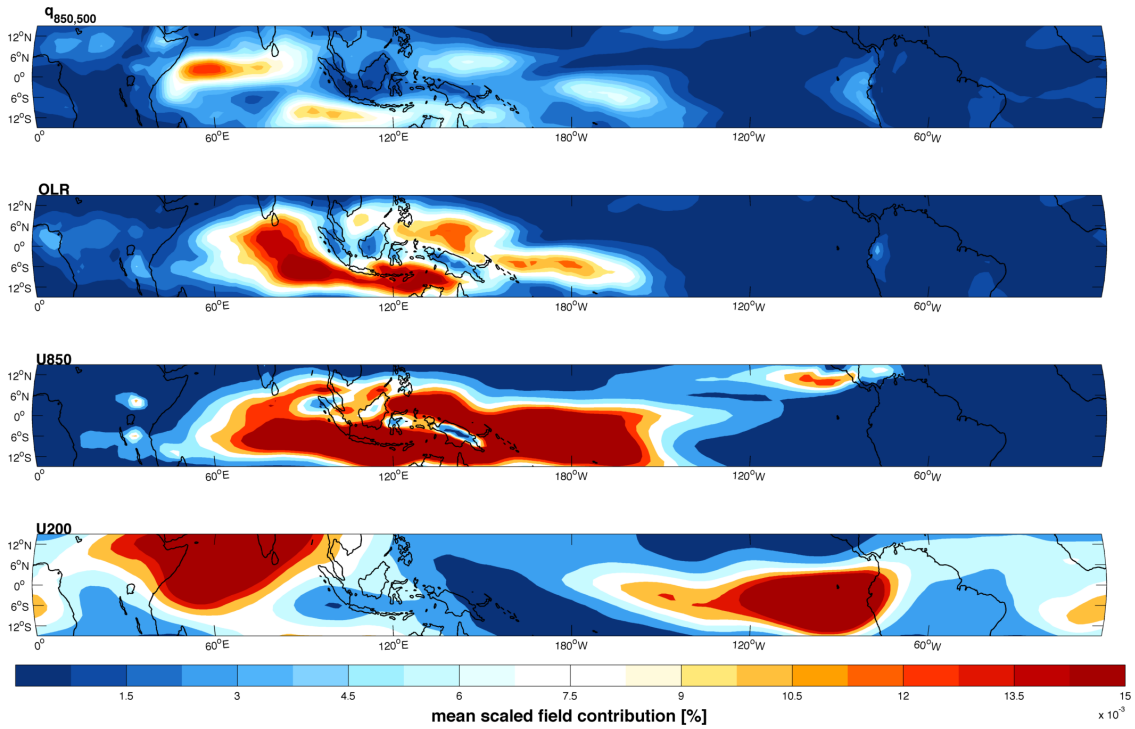

FIG. 3.7. Scaled grid point contribution for each variable used in the CEOF structure, averaged over winter periods (October-April) from 1981-2011. The scaled grid point contribution was calculated from the unfiltered PCs.

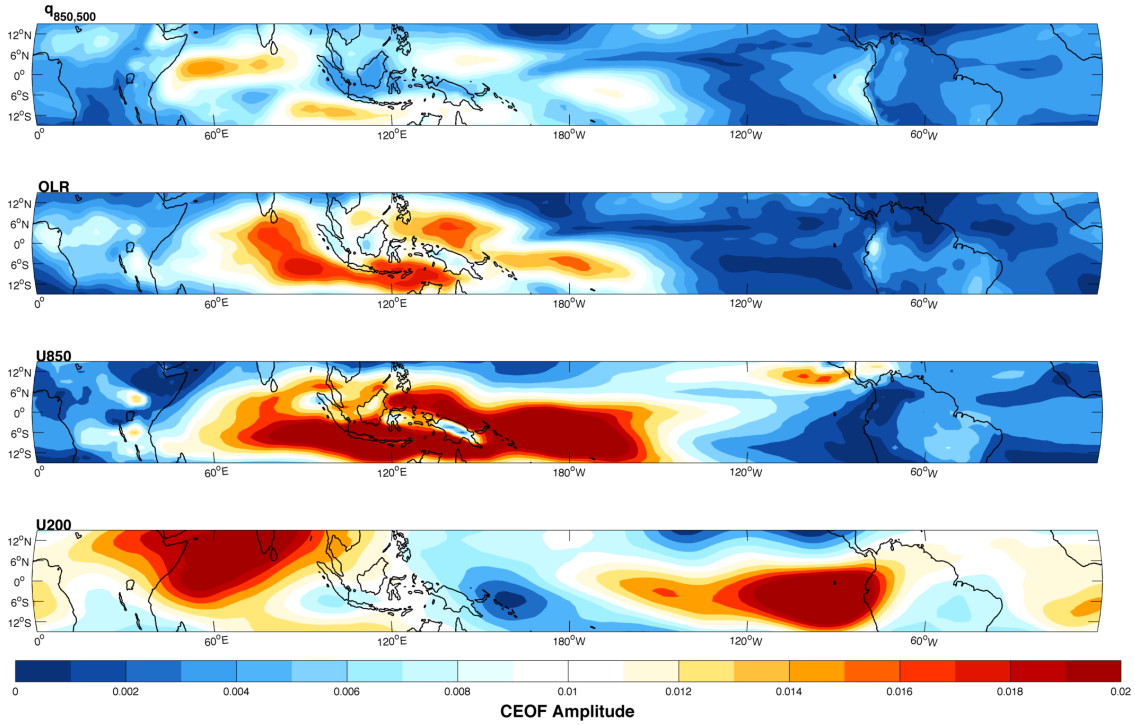

FIG. 3.8. CEOF amplitude for each variable used in the CEOF structure.

Figure 3.9 presents a histogram of the index amplitude in its original form (top) as well as after the power transformation (bottom). The skewed nature of the index in its original form is immediately apparent. Application of a power transformation via the Box-Cox methodology, with ν equal to 0.5, results in an approximately normal distribution to which traditional statistical measures can be applied. Values of the index in its original form corresponding to standard deviations calculated based on the approximately normal distributions are indicated by vertical dashed lines in the top panel of Figure 3.9. Clearly the traditional index value of 1, arbitrarily chosen to represent significant events, is far from the value of one standard deviation it is typically mistaken for. The misconception that an index amplitude of 1 represents a one standard deviation event remains common, as evidenced by the following statement from Straub (2013): "The choice of amplitude 1.0 as the crossover point for MJO initiation is arbitrary, but represents a one standard-deviation anomaly in the RMM index and is typically used as a threshold for significant MJO events (e.g., WH04)". While an index amplitude of 1 may be an appropriate measure for determining when the MJO is likely present, it occurs far more frequently in the historical context of observed events than one standard deviation events have.

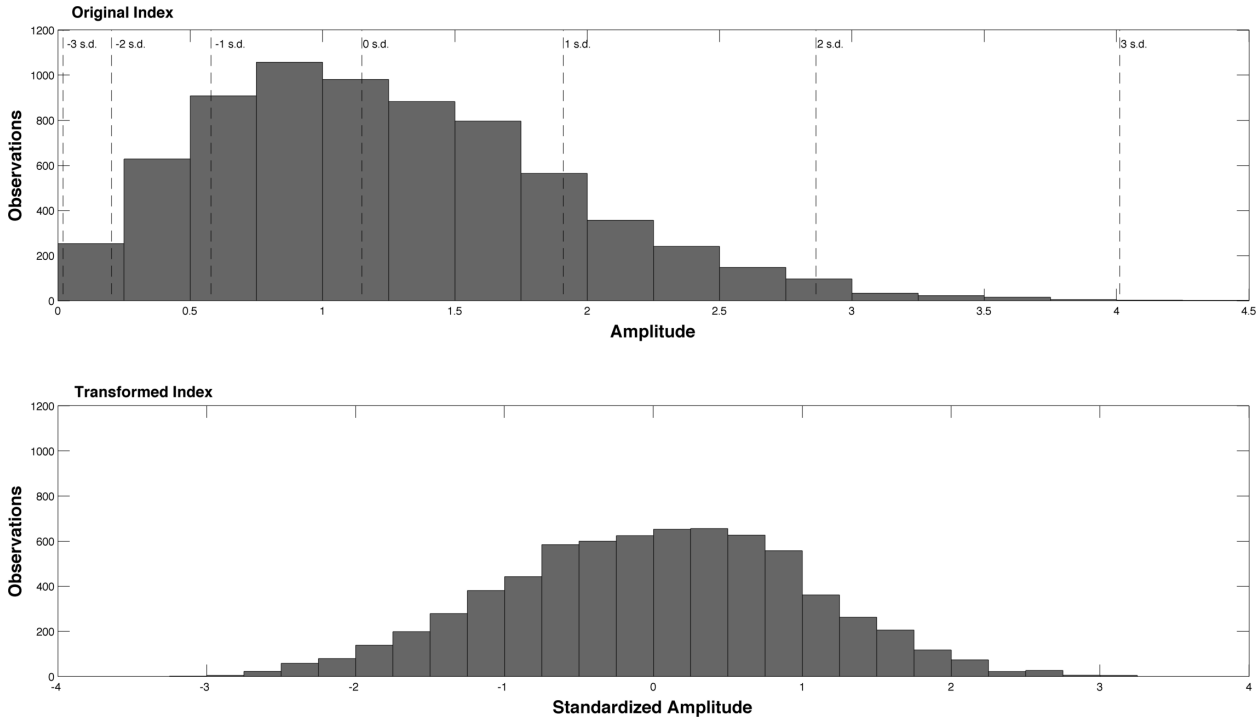

FIG. 3.9. Histograms of the index amplitude when calculated using the traditional method(top) and after application of a power transformation via the Box-Cox methodology(bottom). The dashed vertical lines in the top plot indicate the values of the standard deviations as obtained using the Box-Cox methodology.

A composite lifecycle of the MJO is presented in Figure 1.1, which shows the composite evolution of $q_{850,500}$, OLR and U850 throughout PC1/PC2 phase space. This figure was constructed using a traditional compositing technique, where each phase is defined as in Wheeler and Hendon (2004). In phase one, enhanced convection is co-located with increased free tropospheric humidity mainly over Africa and the Indian Ocean, while suppressed convection is co-located with an anomalously dry free troposphere over the eastern portion of the Maritime continent and the western Pacific. Anomalous U850 easterly conditions extend throughout the region of suppressed convection and westward to the eastern periphery of enhanced convection, while anomalous U850 westerlies prevail throughout the western

periphery of enhanced convection. As the phase increases, regions of enhanced and suppressed convection progress eastward, remaining co-located with $q_{850,500}$ anomalies. U850 wind anomalies continually shift eastward relative to the OLR and $q_{850,500}$ anomalies until, in phase 6, the maximum U850 westerly anomalies are located directly underneath the region of minimum OLR and maximum $q_{850,500}$ in the western Pacific. At this point, the OLR and $q_{850,500}$ anomalies largely disappear, while the U850 anomalies progress rapidly around the western hemisphere. Of particular note are the positive $q_{850,500}$ anomalies that are already present in phase 6 in the initiation region of the western Indian ocean. These anomalies continue to build through phase 7 until the first OLR anomalies develop in phase 8. This increase in free tropospheric humidity occurs a full 2 phases before the appearance of OLR anomalies. Also worth noting is the phase relationship between U850 anomalies and OLR anomalies in the Indian Ocean, which will have substantial implications for the MSE budget of the MJO in the Indian Ocean. While a substantial amount of covariance does exist between U850 and OLR anomalies, maximum U850 anomalies at a given location in the Indian Ocean occur during the transition from enhanced to suppressed phases, roughly in quadrature with OLR anomalies. Comparison of Figure 1.1 with phase composites from Wheeler and Hendon (2004) reveals a remarkable degree of similarity between the two sets of composites, including the phase relationship between U850 and OLR anomalies.

3.2. Moisture, MSE, and Convection

Before discussing the results of the MSE budget, it is worth verifying that several assumptions inherent in the chosen compositing technique are valid. Compositing using relative phase mandates a choice of which fields perspective to view the lifecycle of the MJO from. Results in subsequent sections will largely be presented from the perspective of $q_{850,500}$. This

is motivated by recent studies that have indicated that the MJO may be a moisture mode, and that it is largely $q_{850,500}$ which regulates convection on these timescales. Therefore processes that modify $q_{850,500}$ throughout the MJO lifecycle are of primary interest. The MSE budget was chosen as the tool used to investigate these processes because of the approximately conservative properties of MSE. The WTG balance central to moisture mode theory implies that changes in $\langle h \rangle$ are, to first order, due to changes in $\langle q \rangle$. It is further assumed in this study that changes in $\langle q \rangle$ are largely due to changes in $q_{850,500}$. It is now demonstrated that each of these assumptions is justifiable.

Figure 3.10 shows latitudinally averaged anomalies in $L * q_{850,500}$ as a function of the relative phase of $q_{850,500}$, where L is the latent heat of condensation. This figure shows a composite lifecycle of the MJO from the perspective of $q_{850,500}$, and how that lifecycle changes as a function of longitude. The evolution of $q_{850,500}$ from its minimum value (top of figure) to its maximum value (middle of figure), and then back to its minimum value (bottom of figure) throughout the MJO lifecycle is seen here by analyzing the figure from the top to the bottom. As expected, $q_{850,500}$ anomalies maximize near 0° relative phase, minimize near $180^\circ/-180^\circ$ relative phase, and are near zero when in quadrature with the index (90° or -90°). The relative phase of a given field accurately identifies when the anomalies in that field should be maximized or minimized relative to the MJO life cycle.

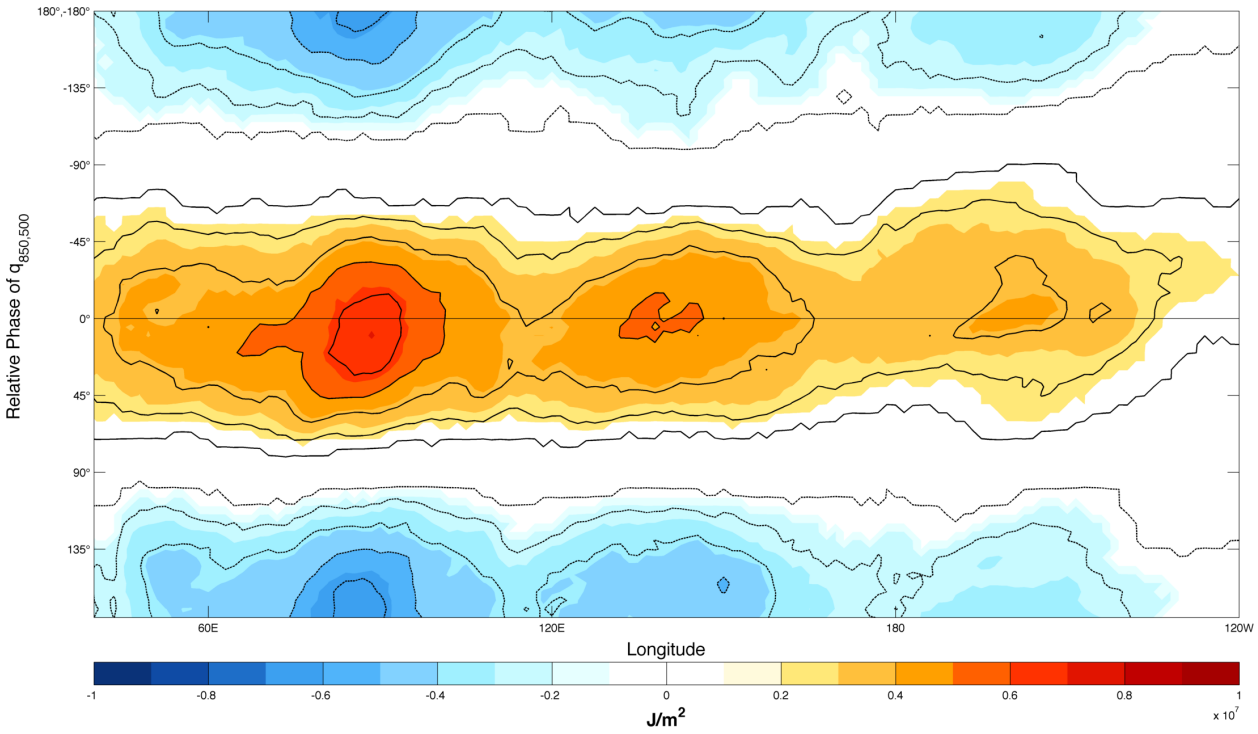

FIG. 3.10. Composite of latitudinally averaged (15°N−15°S) $L*q_{850,500}$ anomalies (color contours) and $q_{850,500}$ anomalies (contours) as a function of relative phase of $q_{850,500}$. Solid (dashed) contours are positive (negative) $q_{850,500}$ anomalies of 0.5,1.5,2.5,3.5 (-0.5,-1.5,-2.5,-3.5) $\mathrm{kg\,kg^{-1}}$.

Figures 3.11 and 3.12 show latitudinally averaged anomalies in $\langle Lq \rangle$ and $\langle h \rangle$ as a function of the relative phase of $q_{850,500}$ respectively. Comparison of these figures shows that changes in $\langle Lq \rangle$ account for $\sim$ 90% of changes in $\langle h \rangle$ throughout the MJO lifecycle, irrespective of geographic location. This is a slightly larger proportion than found in Kiranmayi and Maloney (2011), who found that $\langle Lq \rangle$ anomalies accounted for $\sim$ 80% of changes in $\langle h \rangle$. Further comparison with Figure 3.10 shows that changes in $L * q_{850,500}$ account for $\sim$ 75% of changes in $\langle Lq \rangle$ and $\sim$ 70% of changes in $\langle h \rangle$. This is consistent with the findings of Kiladis et al. (2005) and Benedict and Randall (2007). Therefore, in the context of the present MSE budget, it is appropriate to view processes that modify $\langle h \rangle$ on intraseasonal timescales as process that modify $\langle q \rangle$ and $q_{850,500}$.

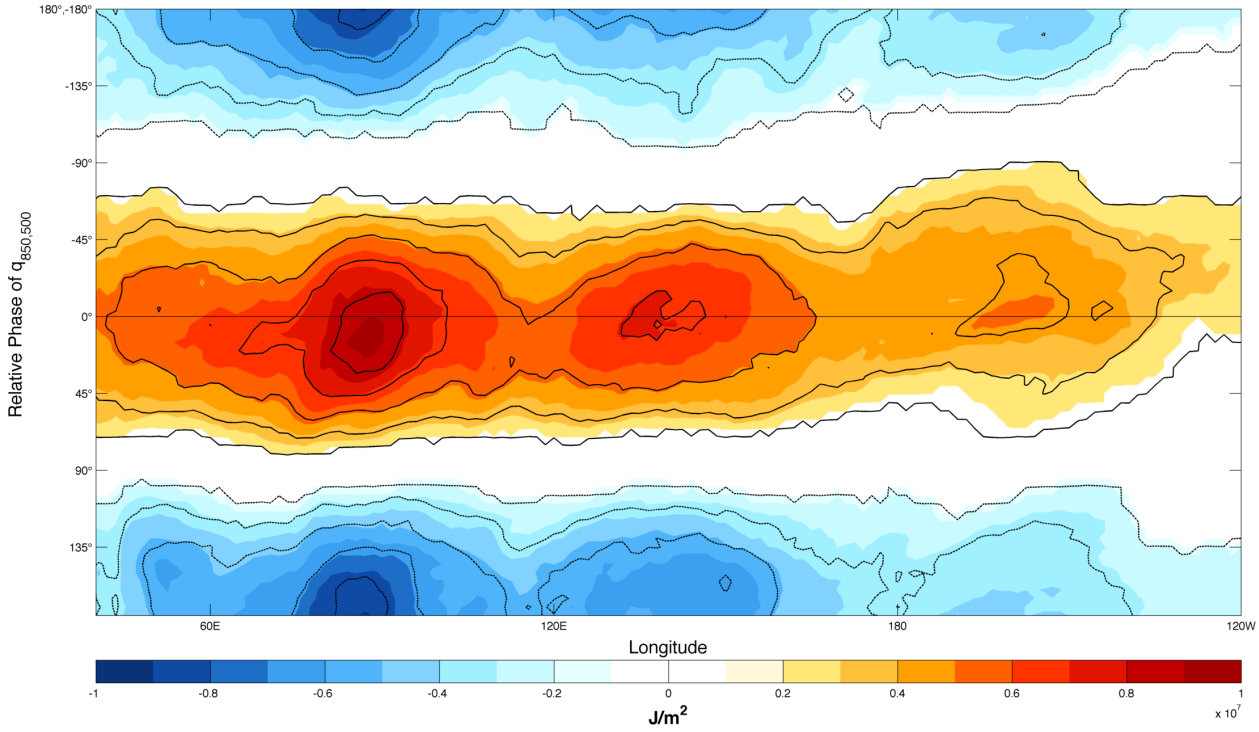

FIG. 3.11. As in Figure 3.10, except color contours are $\langle Lq \rangle$ anomalies.

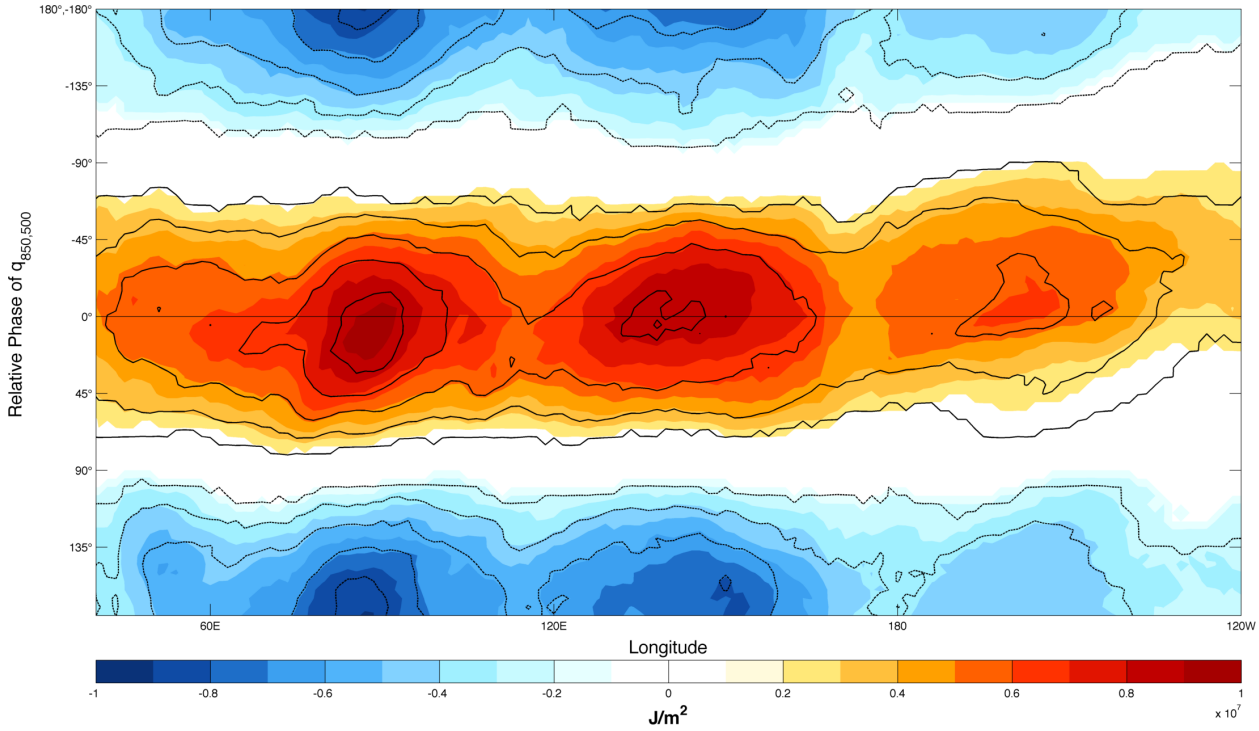

FIG. 3.12. As in Figure 3.10, except color contours are $\langle h \rangle$ anomalies.

The phase composites presented in Figure 1.1 showed that $q_{850,500}$ and OLR anomalies are approximately co-located at each phase of the MJO lifecycle. Figure 3.13 supports this assertion, showing that OLR anomalies reach their minimum near the time of maximum $q_{850,500}$, and vice versa. Minimum values of OLR lag the peak in $q_{850,500}$ by $\sim 15°$, approximately 5% of the MJO lifecycle. A similar lag between MSE and OLR anomalies was observed in the analysis of Cai et al. (2013), who used ERA-40 data in their analysis. As will be discussed later, this lag may be spuriously introduced by the bandpass filtering of $q_{850,500}$. Further evidence for the relationship between $q_{850,500}$ and convection is provided by Figure 3.14, a scatterplot of TRMM precipitation at four locations as a function of index amplitude and relative phase of $q_{850,500}$. Below an index amplitude of 1 (denoted by a vertical dashed line in Figure 3.14), and especially below an an index amplitude of 0.5, little variation in precipitation rates as a function of relative phase of $q_{850,500}$ is apparent at any of the four locations. In other words, when the index amplitude is low, little modulation of precipitation occurs as the index phase changes. When the index amplitude exceeds 1, precipitation is a strong function of the relative phase of $q_{850,500}$ at all four locations, being largest when $q_{850,500}$ anomalies are largest (relative phase near 0°) and smallest when $q_{850,500}$ anomalies are smallest (relative phase near $180°/-180°$). Not only does this demonstrate that $q_{850,500}$ anomalies are closely related to convection on MJO timescales, but it shows that the convective lifecycle of the MJO at disparate geographical locations can be compared effectively and objectively using the relative phase of $q_{850,500}$. The close relationship between free tropospheric humidity and precipitation is consistent with previous studies by Bretherton et al. (2004), Holloway and Neelin (2009) and Neelin et al. (2009).

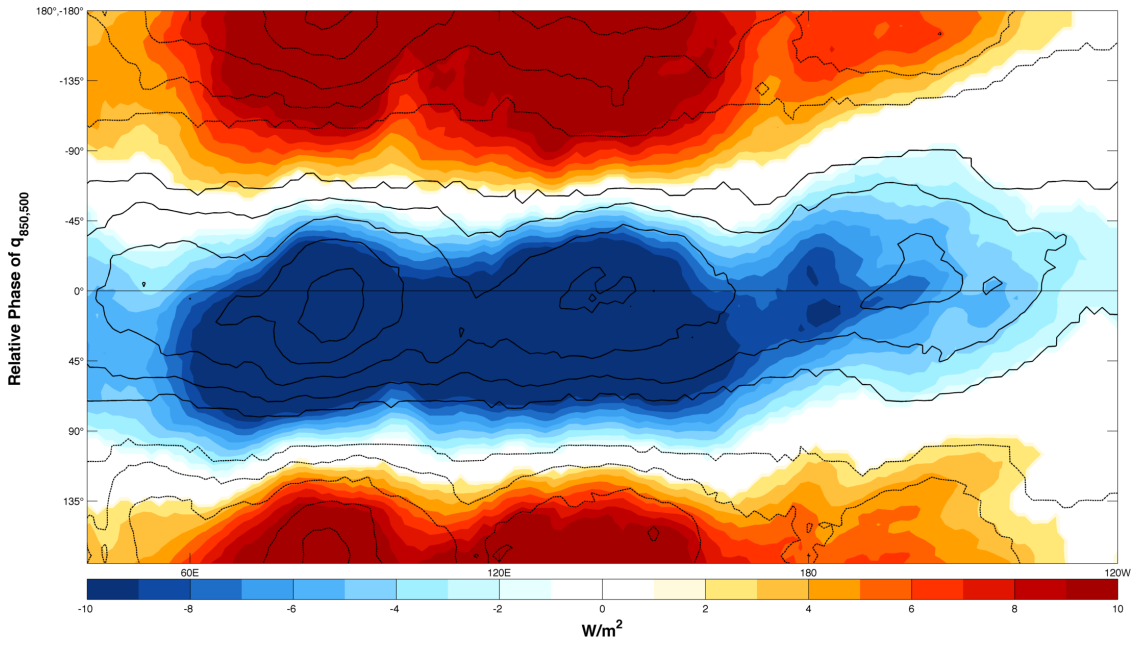

FIG. 3.13. As in Figure 3.10, except color contours are ERAi OLR anomalies.

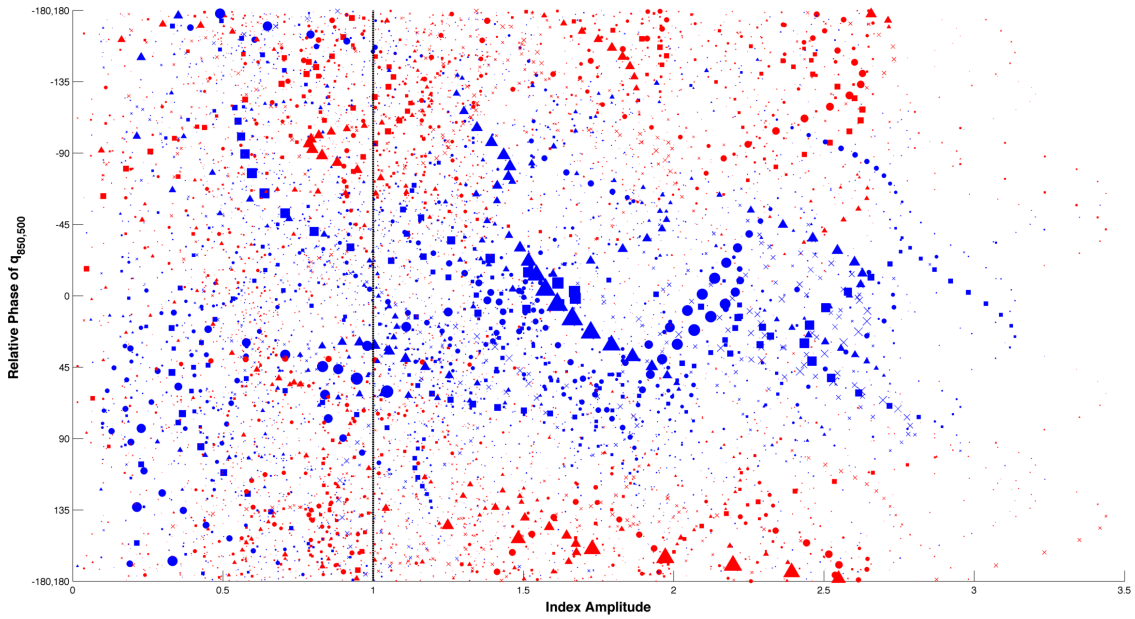

FIG. 3.14. 20 -100 day bandpass filtered TRMM precipitation at 64.5°E, 0°S (square),79.5°E, 0°S (circle), 150°E, 0°S (x), 169.5°E, 10.5°S (triangle) from October 1 2000 to April 30 2009 as a function of index amplitude. Negative (positive) anomalies are colored red (blue) and the size of the marker is scaled to be proportional to the square of the amplitude of the anomaly. A vertical dashed line denotes an index amplitude of 1.

3.3. MSE Budget Results

The phase relationship between low level wind anomalies and moisture anomalies is crucially important in determining whether certain processes, such as LH, affect the destabilization and/or propagation of the MJO. Figure 3.15 shows the relationship of U850 anomalies to $q_{850,500}$ anomalies as a function of relative phase of $q_{850,500}$. The phasing between U850 anomalies and $q_{850,500}$ anomalies changes substantially as a function of longitude. Light easterly U850 anomalies are co-located with maximum $q_{850,500}$ anomalies in the western IO. There, the transition to westerly wind anomalies occurs approximately 30° of phase after the maximum $q_{850,500}$ anomalies. U850 anomalies and $q_{850,500}$ anomalies are approximately in quadrature from the central IO to the eastern edges of the Maritime Continent, with the transition from easterly anomalies to westerly anomalies occurring about 15° of phase prior to maximum $q_{850,500}$ anomalies over much of this region. In the western Pacific, stronger westerly U850 anomalies are co-located with maximum $q_{850,500}$ anomalies, and the transition from easterly to westerly U850 anomalies occurs approximately 45° degrees of phase prior to maximum $q_{850,500}$ anomalies. The change of phasing typically observed between low level winds and convection as a function of longitude has been well documented (Hendon and Salby 1994; Wheeler and Hendon 2004; Zhang 2005; Kiladis et al. 2005; Benedict and Randall 2007), and is seen in the traditional composite presented earlier in Figure 1.1. This provides confidence in the compositing technique implemented here, and serves as a reminder that the "fundamental" observed structure of the MJO is not static.

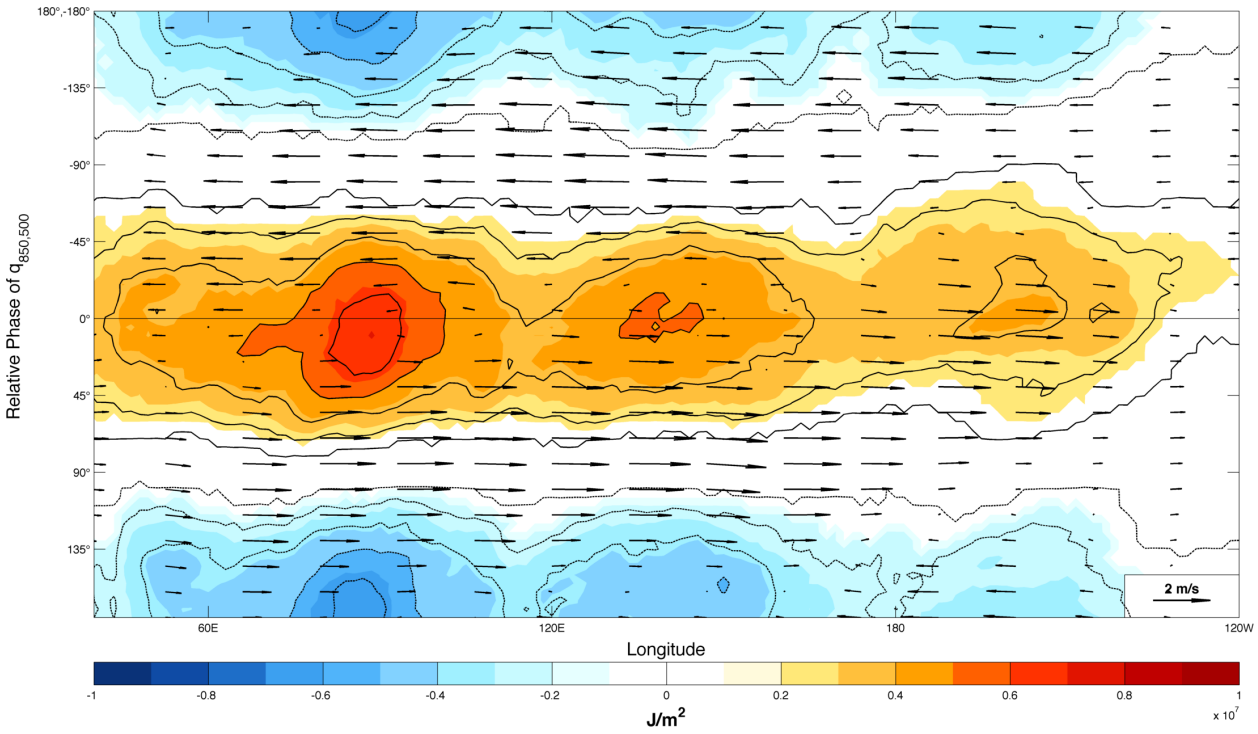

FIG. 3.15. Composite of latitudinally averaged (15°N−15°S) $L*q_{850,500}$ anomalies (color contours), $q_{850,500}$ anomalies (contours) and 850 hPa horizontal wind anomalies (vectors) as a function of relative phase of $q_{850,500}$. Solid (dashed) contours are positive (negative) $q_{850,500}$ anomalies of 0.5,1.5,2.5,3.5 (-0.5,-1.5,-2.5,-3.5) $\mathrm{kg\,kg^{-1}}$. A reference wind vector is provided in the lower right corner.

The latitudinally averaged column integrated MSE tendency is displayed as a function of relative phase of $q_{850,500}$ and longitude in Figure 3.16. MSE tendency is approximately in quadrature with $q_{850,500}$ anomalies in the eastern hemisphere. Geographical locations of maximum MSE tendency coincide with regions with largest $q_{850,500}$ anomalies. Maximum column integrated MSE tendencies are approximately $15\frac{\mathrm{W}}{\mathrm{m}^2}$, but keep in mind that these are values averaged from 15°N-15°S. These tendencies are larger than those found by Kiranmayi and Maloney (2011) and Wu and Deng (2013). Figure 3.17 shows that the budget residual is largest during periods of intense moistening (drying) immediately preceding maximum (minimum) $q_{850,500}$ anomalies. The budget residual of Kiranmayi and Maloney (2011) was

also found to be largest during transition periods between suppressed and convective phases. Mapes and Bacmeister (2012) also identified spurious moisture processes during the transition from suppressed to enhanced convection, and concluded that poorly constrained deep convective schemes were likely serving as overactive moisture sinks during this period. This suggests that the budget residual may result from the misrepresentation of moistening/drying processes associated with the MJO, as well as inaccuracies associated with performing the budget calculation using standard output variables instead of direct output from the model dynamical core. The budget residual is substantially smaller than the observed tendency, but nonetheless is a qualification to the subsequent interpretation of budget results.

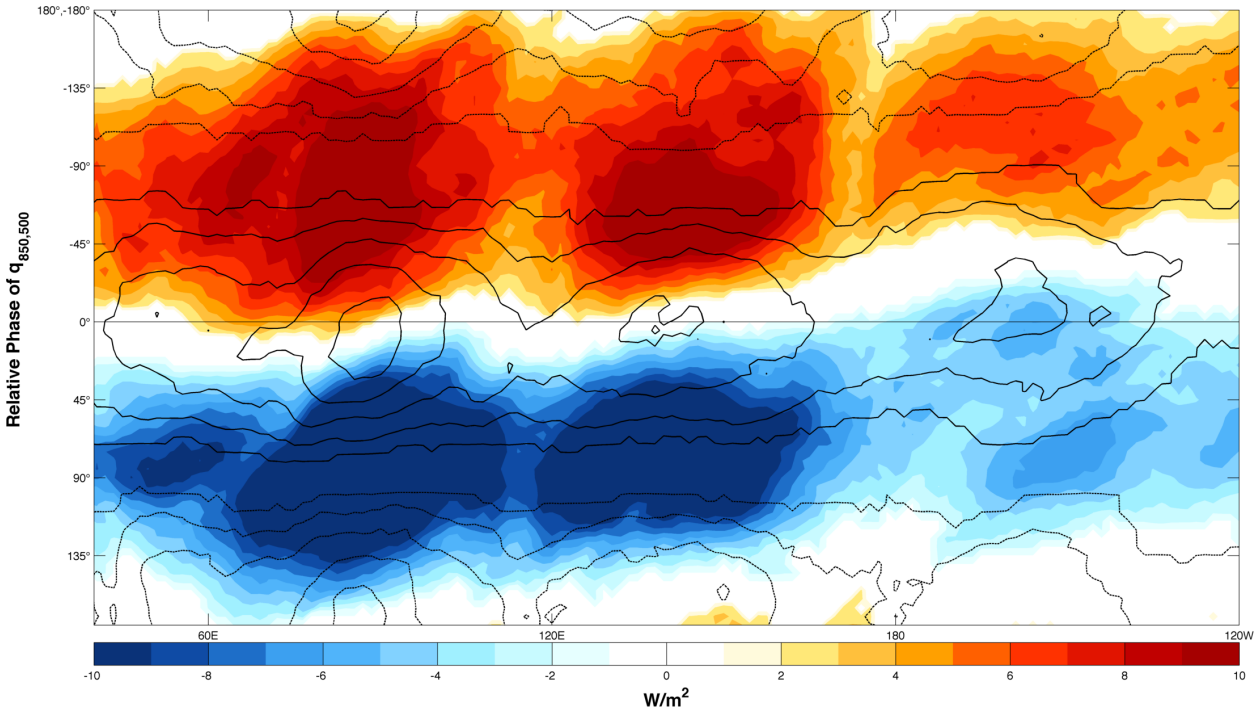

FIG. 3.16. As in Figure 3.10, except color contours are $\left\langle \frac{\partial h}{\partial t} \right\rangle$.

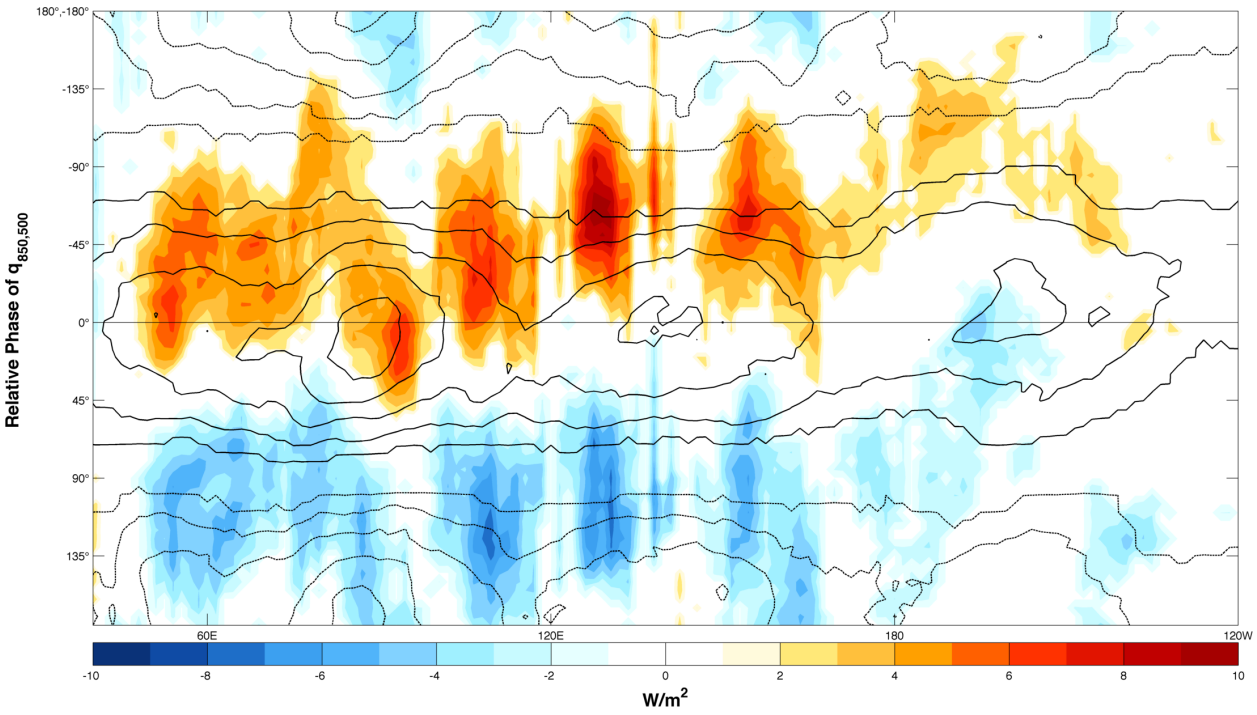

FIG. 3.17. As in Figure 3.10, except color contours are the budget residual.

Figure 3.18 shows that anomalous column integrated radiative heating is approximately in phase with $q_{850,500}$. Comparison with Figure 3.13 shows that, at least in ERAi, anomalous radiative heating is almost entirely the result of the modulation of OLR, which implies that changes to net surface longwave radiation and and column shortwave absorption are small. Wu and Deng (2013) similarly noted that the shortwave heating component was small in a MSE budget of the MJO using NCEP reanalysis. As ERAi relies on convective parameterizations, it is prudent to seek observational verification for these OLR values. Figure 3.19 shows latitudinally averaged NOAA OI OLR anomalies as a function of relative phase. Qualitatively these values correspond very closely with those of ERAi, showing almost identical phasing and geographical locations of maximum and minimum values. Quantitatively, ERAi appears to underestimate OLR anomalies by $\sim 20\%$ relative to NOAA OI values. While it is tempting to make a direct connection between this bias in OLR and the $\langle Q_r \rangle$ term of the

MSE budget, this can not be done without corresponding observational verification of the SW component.

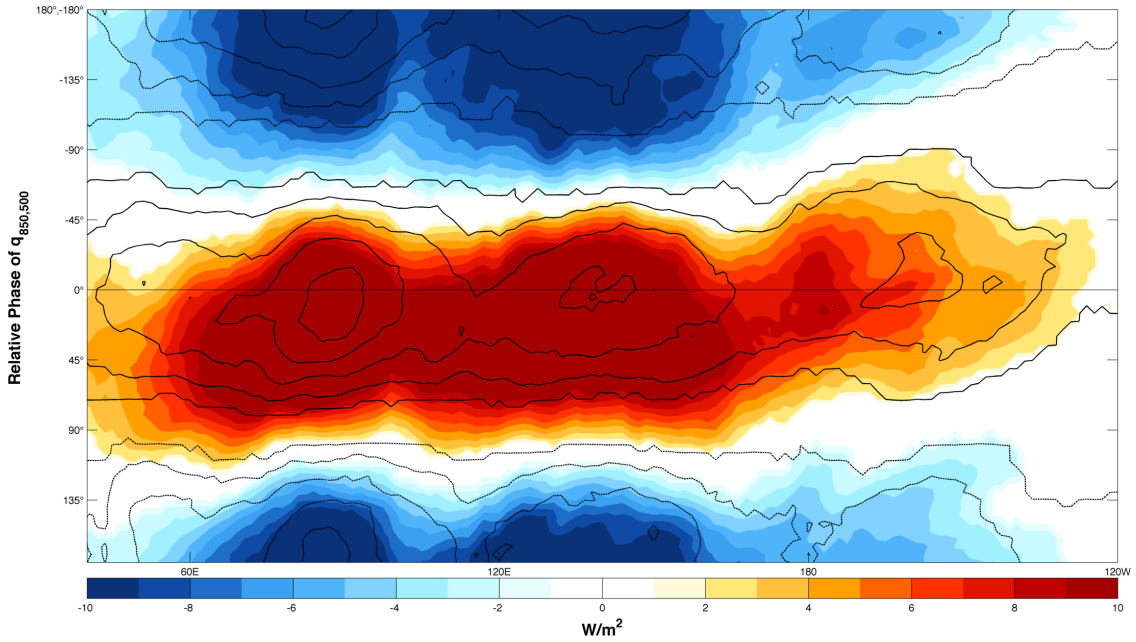

FIG. 3.18. As in Figure 3.10, except color contours are ERAi $\langle Q_r \rangle$ anomalies.

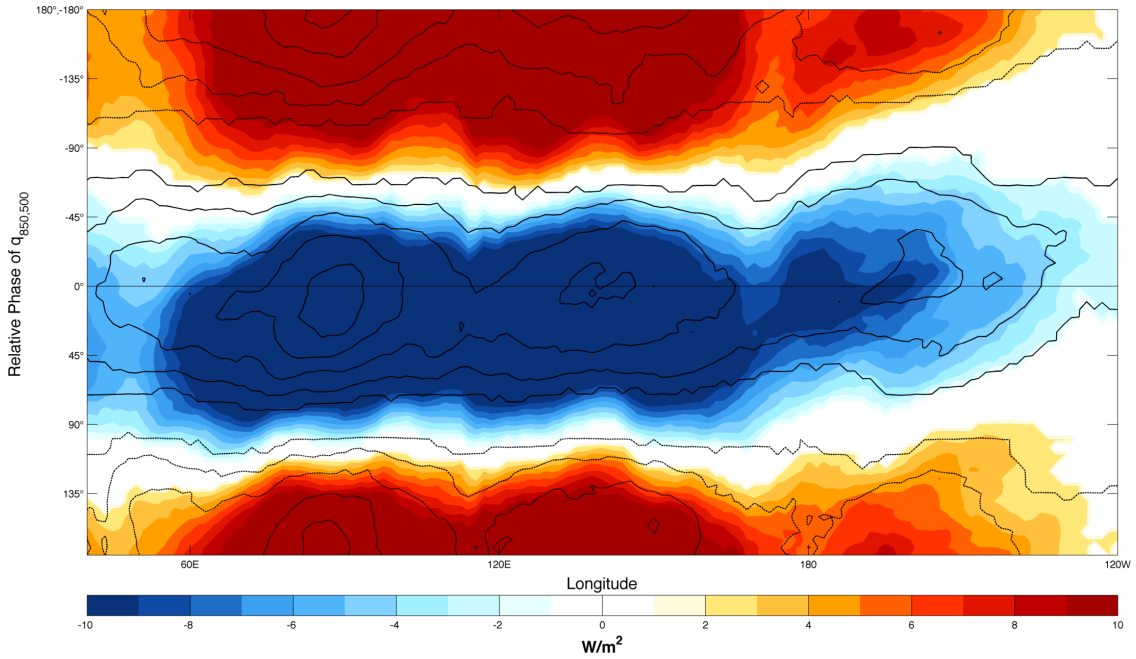

FIG. 3.19. As in Figure 3.10, except color contours are NOAA OI OLR.

Figure 3.20 shows that anomalous vertical MSE advection is approximately out of phase with anomalous $q_{850,500}$, as well as radiative heating anomalies. During periods of anomalously low $q_{850,500}$ and suppressed convection, when area averaged heating profiles are anomalously shallow, the vertical MSE advection term is acting to import MSE to the column in both an anomalous and total sense. During periods of anomalously high $q_{850,500}$ and enhanced convection, when area averaged heating profiles are anomalously top heavy, the vertical MSE advection term is acting to export MSE from the column, in both an anomalous and total sense.

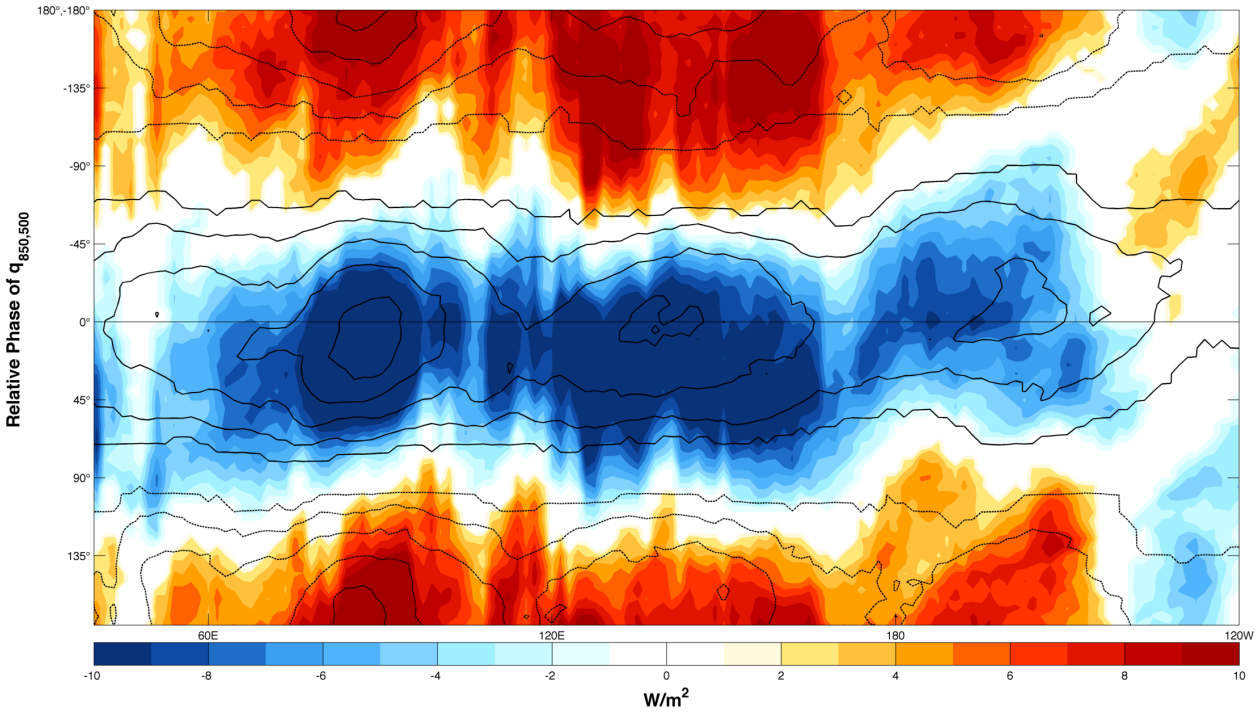

FIG. 3.20. As in Figure 3.10, except color contours are $-\left\langle \omega \frac{\partial h}{\partial p} \right\rangle$ anomalies.

LH dominates the surface fluxes in the MSE budget, often contributing in excess of 90% of the combined surface fluxes of MSE. This is consistent with similar MSE budgets by Kiranmayi and Maloney (2011) and Wu and Deng (2013). Figure 3.21 shows that in the eastern hemisphere, where mean state low level winds are predominantly westerly, LH

anomalies are nearly in phase with U850 anomalies. This in phase relationship has been observed by Lin and Johnson (1996b) and Zhang and McPhaden (2000). East of the date line, where mean state low level winds are easterly, LH anomalies are out of phase with U850 anomalies. The close relationship between U850 anomalies and LH anomalies means that the phase relationship between MSE anomalies and LH anomalies varies substantially with longitude. This change in phase relation, which appears to occur as a result of the change in mean state low level winds, fundamentally changes the way in which LH anomalies affect MSE anomalies. In the eastern hemisphere, LH anomalies are largest when in quadrature with MSE anomalies, and consistently act to oppose the MSE tendency. East of the date line LH is enhanced during periods of suppressed convection and reduced during periods of enhanced convection, consistently acting to reduce the amplitude of MSE anomalies. LH anomalies appear to be relatively small in the region from 70°E to 100°E, but further inspection reveals this not to be the case. The top (bottom) of Figure 3.22 shows U850 anomalies and LH anomalies at 0° (−180/180°) relative phase of U850. This corresponds to the period of maximum U850 westerly(easterly) wind anomalies associated with the MJO at each location. Close inspection of the region of 70°E to 100°E shows that LH anomalies are actually quite large, but substantial cancellation occurs in the latitude averaging used to create Figure 3.21. During periods of anomalous U850 westerly(easterly) winds LH is enhanced(reduced) in the region of mean state westerly winds, while the poleward regions of easterly mean state winds experience reduced(enhanced) LH.

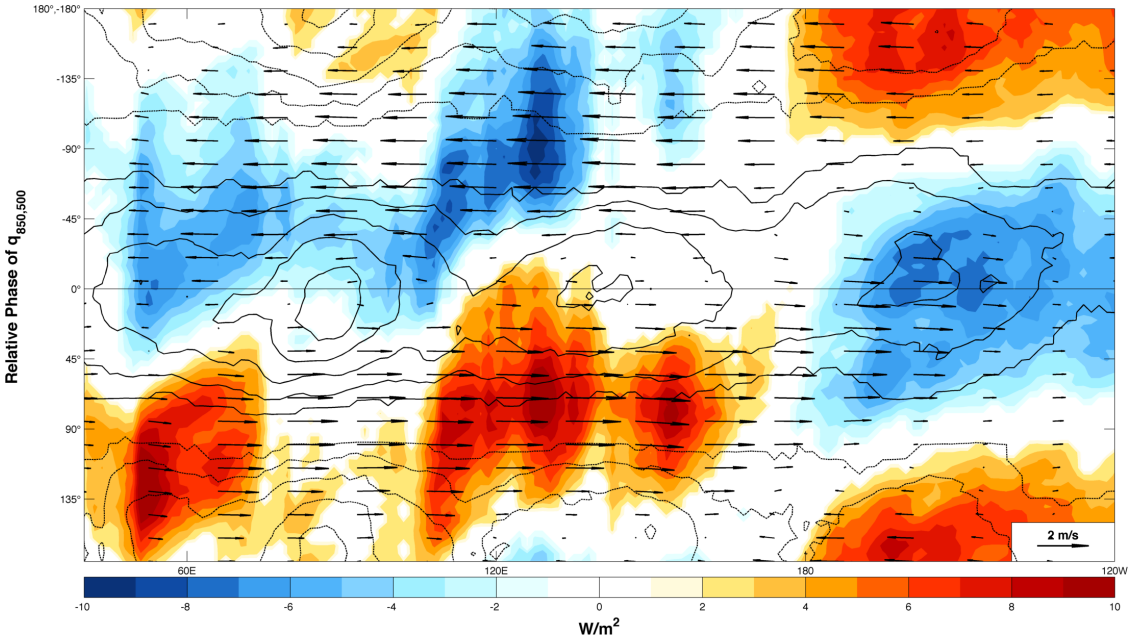

FIG. 3.21. As in Figure 3.15, except color contours are LH anomalies.

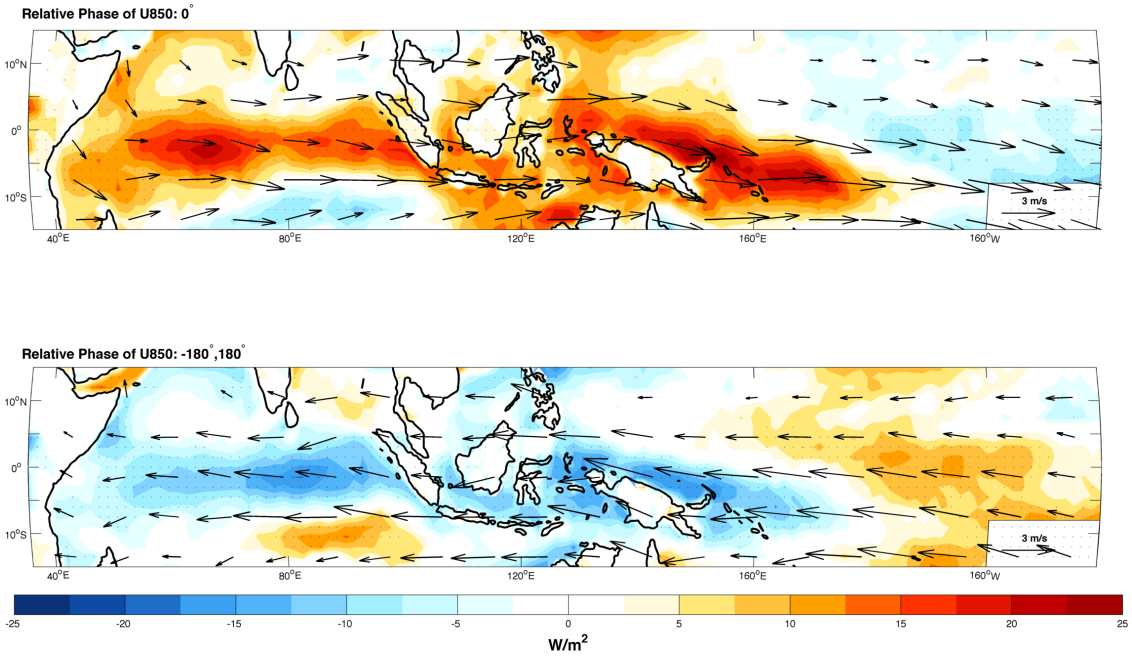

FIG. 3.22. The top (bottom) panel shows composite LH anomalies (color contours) and 850 hPa horizontal wind anomalies (vectors) at 0° (−180°, 180°) relative phase of U850. Stippling indicates LH anomalies significant at the 95% level. Wind vectors are statistically significant at the 95% level. A reference wind vector is provided in the lower right corner.

Comparison of LH anomalies in ERAi with SeaFlux LH estimates (Figure 3.23) shows that the two are qualitatively very similar, showing the same phase relationship with winds and $q_{850,500}$ as well as similar geographical locations of maximum and minimum values. Please note that the composite in Figure 3.23 is calculated using data from 2000-2007, and that the contour levels differ from those in Figure 3.22. Quantitatively, LH anomalies in ERAi are consistently $\sim 50\%$ larger than SeaFlux estimates. No significant correlation was found between LH and the budget residual when computed on various temporal and spatial scales.

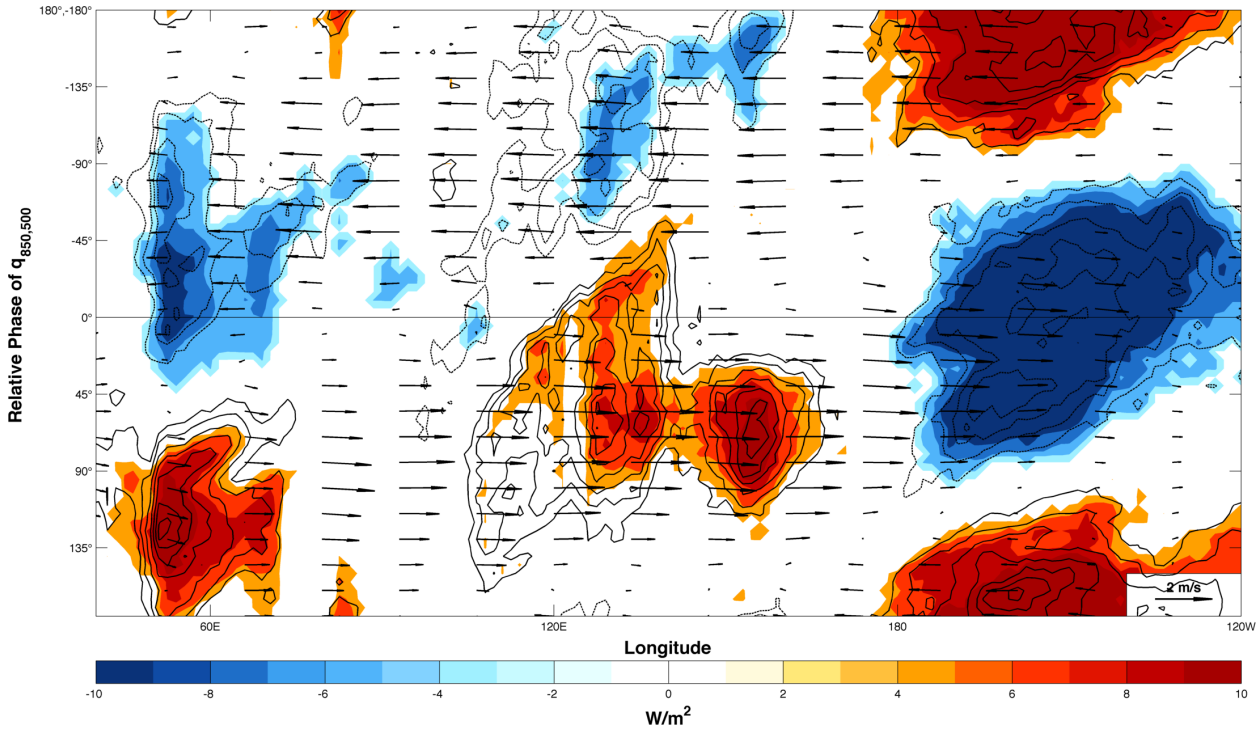

FIG. 3.23. Composite of latitudinally averaged (15°N – 15°S) SeaFlux LH anomalies (color contours), ERAi LH anomalies (contours) and 850 hPa horizontal wind anomalies (vectors) as a function of relative phase of $q_{850,500}$ for winter months from 2000 to 2007. Solid (dashed) contours are positive (negative) ERAi LH anomalies of 4,6,8,10,12,14,16 (-0.5,-1.5,-2.5,-3.5) $\mathrm{W\,m^{-2}}$. A reference wind vector is provided in the lower right corner.

Figure 3.24 shows SH anomalies as a function of relative phase of $q_{850,500}$. Please note that the color scale in this figure only ranges from -1 to 1 $\frac{\mathrm{W}}{\mathrm{m}^2}$. SH anomalies are only about 10% of total surface flux anomalies, and contribute very little to the overall anomalous MSE

budget. Worth noting is that periods of maximum amplitude SH anomalies seem to occur when wind anomalies are small, and do not correspond with periods of maximum amplitude LH anomalies. This phase relationship between low level winds and SH is supported by the observations of Lin and Johnson (1996b).

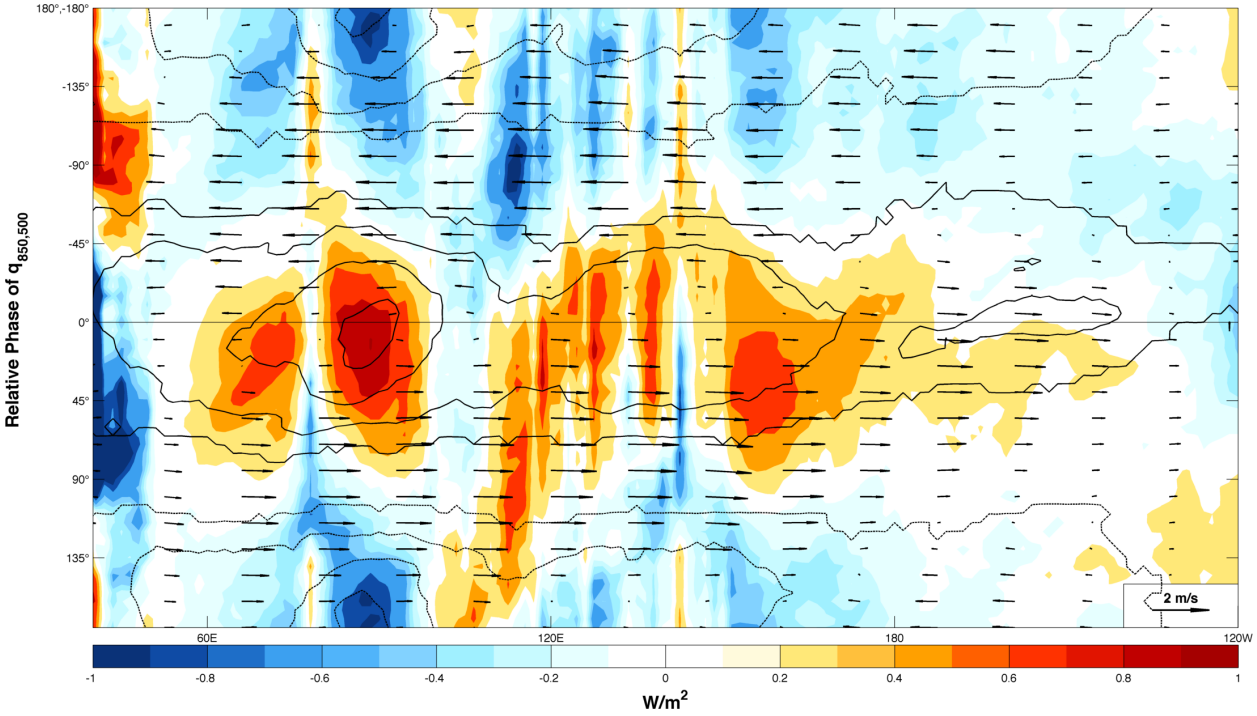

FIG. 3.24. As in Figure 3.10, except color contours are SH anomalies.

Similar to LH anomalies, anomalous horizontal MSE advection is closely tied to low level wind anomalies, and its phase relationship with MSE anomalies changes substantially as a function of longitude. Anomalous horizontal MSE advection is approximately in quadrature with MSE anomalies in the eastern hemisphere. Anomalous horizontal MSE advection begins to anomalously import MSE when convection is at its most suppressed state, and continues to do so until just before the peak of convection. This is consistent with the findings of Kiranmayi and Maloney (2011) and Wu and Deng (2013). This phase relationship begins to change near the dateline, and east of the date line anomalous horizontal MSE advection,

although substantially reduced, is approximately in phase with MSE anomalies. Worth noting is that while positive horizontal MSE advection is associated with easterly U850 anomalies in the eastern hemisphere, east of the date line positive horizontal MSE advection is associated with westerly U850 anomalies. Horizontal advection will be further discussed below.

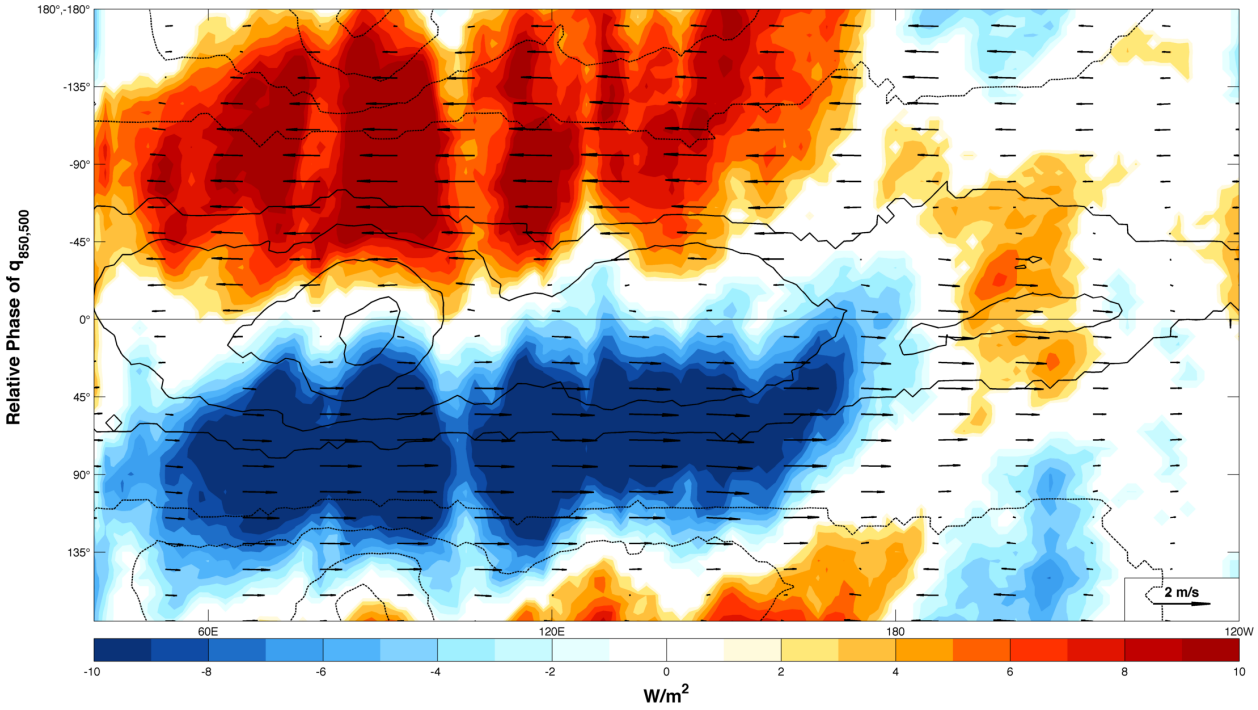

FIG. 3.25. As in Figure 3.15, except color contours are $-\langle \vec{v} \cdot \nabla h \rangle$ anomalies.

3.3.1. Maintenance and Propagation

In the eastern hemisphere, MSE anomalies are approximately in phase with radiative heating anomalies and SH anomalies, and approximately out of phase with vertical MSE advection anomalies. MSE tendency is approximately in phase with horizontal advection anomalies and approximately out of phase with LH anomalies. This motivates looking at a balance of these budget terms to see how they may contribute to the maintenance and propagation of the MJO in the eastern hemisphere.

Figure 3.26 shows that, in almost all locations, and at almost all stages of the MJO life cycle, the net affects of anomalous radiative heating, SH and vertical MSE advection result in a large degree of cancelation. This is quite profound given equation 1.19, which says that in WTG balance, the net affects of these three terms quantifies the net affects of anomalous vertical moisture advection and anomalous precipitation on $\langle Lq \rangle$. Considering that area averaged LP anomalies are often on the order of several hundred watts per meter squared, the large degree of cancelation between anomalous radiative heating, SH and vertical MSE advection implies that anomalous moistening or drying by vertical moisture advection is almost completely balancing anomalous moisture loss by precipitation in both enhanced and suppressed convective periods. The residual of anomalous radiative heating, SH and vertical MSE advection (Figure 3.26), implies a small amount of anomalous moistening or drying occurs as the net result of anomalous precipitation and anomalous vertical moisture advection. This is actually seen in moisture budgets performed by Kiranmayi and Maloney (2011) at various locations, ranging from entrap Indian Ocean to the west Pacific.

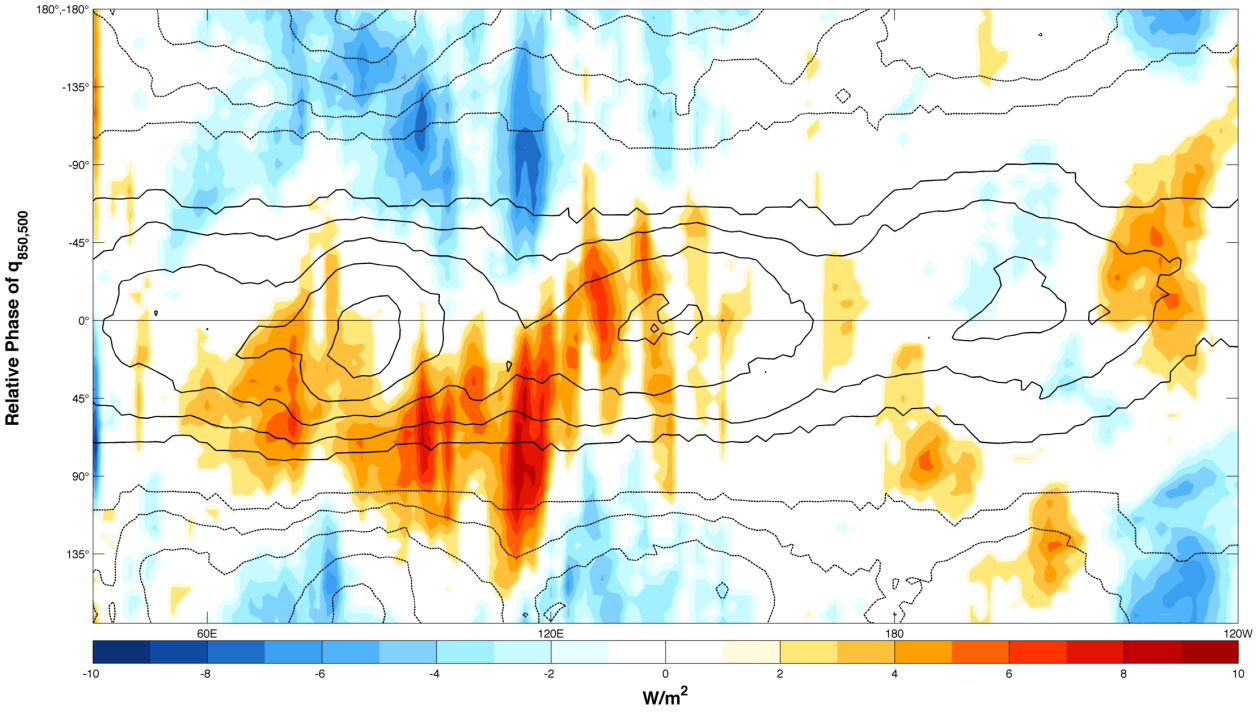

FIG. 3.26. As in Figure 3.15, except color contours are $-\left\langle \omega \frac{\partial h}{\partial p} \right\rangle + \mathrm{Q}_r + \mathrm{SH}$ anomalies.

This interpretation of Figure 3.26 is based on an analysis of the MSE budget terms that assumes a WTG balance. It has already been shown that changes in $\langle Lq \rangle$ account for $\sim 90\%$ of changes in $\langle h \rangle$, lending support to the application of a WTG balance interpretation. Figure 3.27 provides further support for this interpretation. All terms presented here have been bandpass filtered to 20-100 days, and averaged over the central Indian Ocean during periods where the index amplitude exceeded 1. The back line indicates the relationship predicted by equation 1.19 under WTG balance. The slope of the best fit line (not shown) is 1.013, and correlation analysis resulted in an r value of 0.65 that was statistically significant at 95%. This plot suggests that MSE budget terms can provide a reasonable estimate of the net affect of precipitation and vertical moisture advection, especially considering that the net affect is the difference between two large terms.

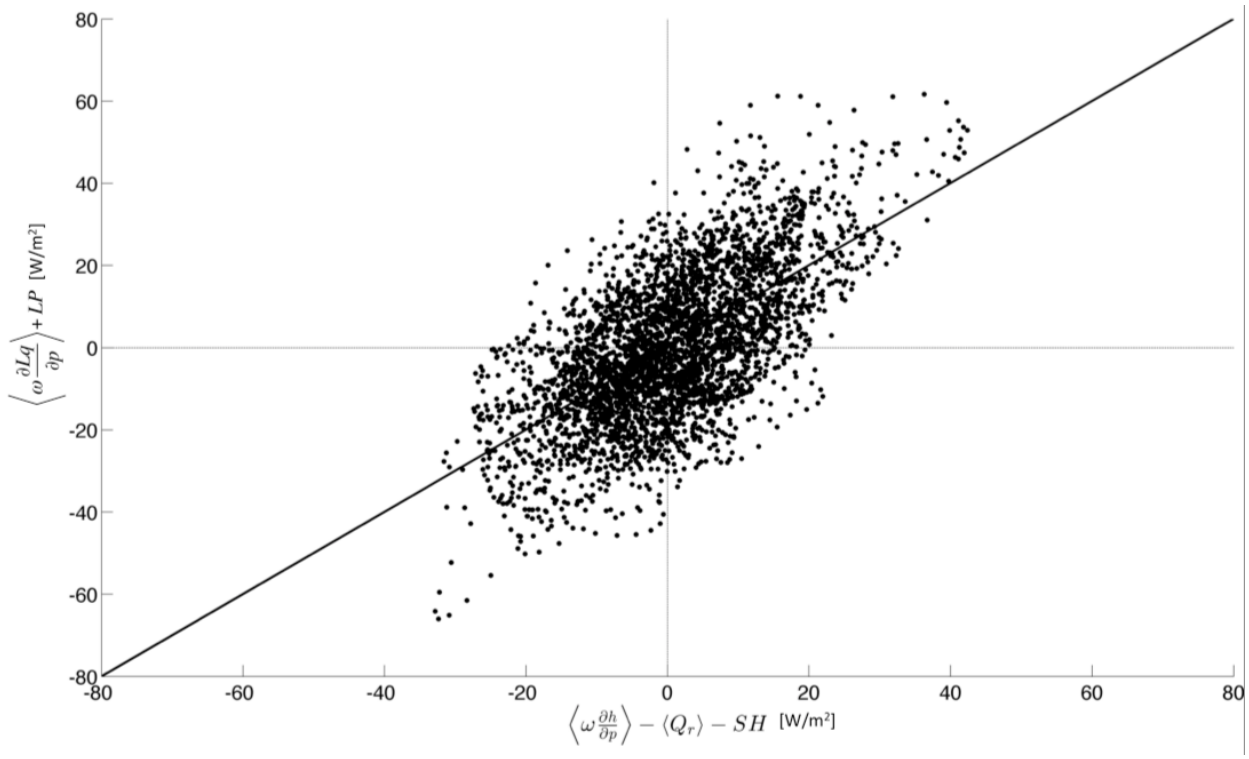

FIG. 3.27. A scatterplot of select vertically integrated anomalous MSE and moisture budget terms in the central Indian Ocean, from 1981-2011. All terms were bandpass filtered to 20-100 days and spatially averaged from 4.5°N-4.5°S,70.5°E-79.5°E. Only days where the index amplitude exceeded 1 were included. The black line has a slope of 1, and is the relationship between MSE budget terms and moisture budget terms predicted by equation 1.19 under WTG balance. This line has not been statistically fit to the data, and is included only to serve as a visual reference for a one-to-one relationship.

Figure 3.28 is a scatterplot of anomalous precipitation and anomalous vertical moisture advection over the central Indian Ocean. The long term average ratio of vertical moisture advection to precipitation is approximately 0.5 over this region. The red line superimposed on Figure 3.28 has a slope of -0.5, and represents the relationship between anomalous precipitation and vertical moisture advection that would occur if anomalies in both fields occurred at the climatological ratio. The black line superimposed on Figure 3.28 has a slope of -1, which would occur if anomalous vertical moisture advection exactly offset the affects of anomalous precipitation. The slope of the best fit line (not shown) is -1.13, and correlation

analysis resulted in an r value of -0.98 that was statistically significant at 95%. This suggests that the affects of anomalous vertical moisture advection tend to slightly exceed the affects of anomalous precipitation, resulting in an anomalous drying during periods of suppressed precipitation and an anomalous moistening during periods enhanced precipitation.

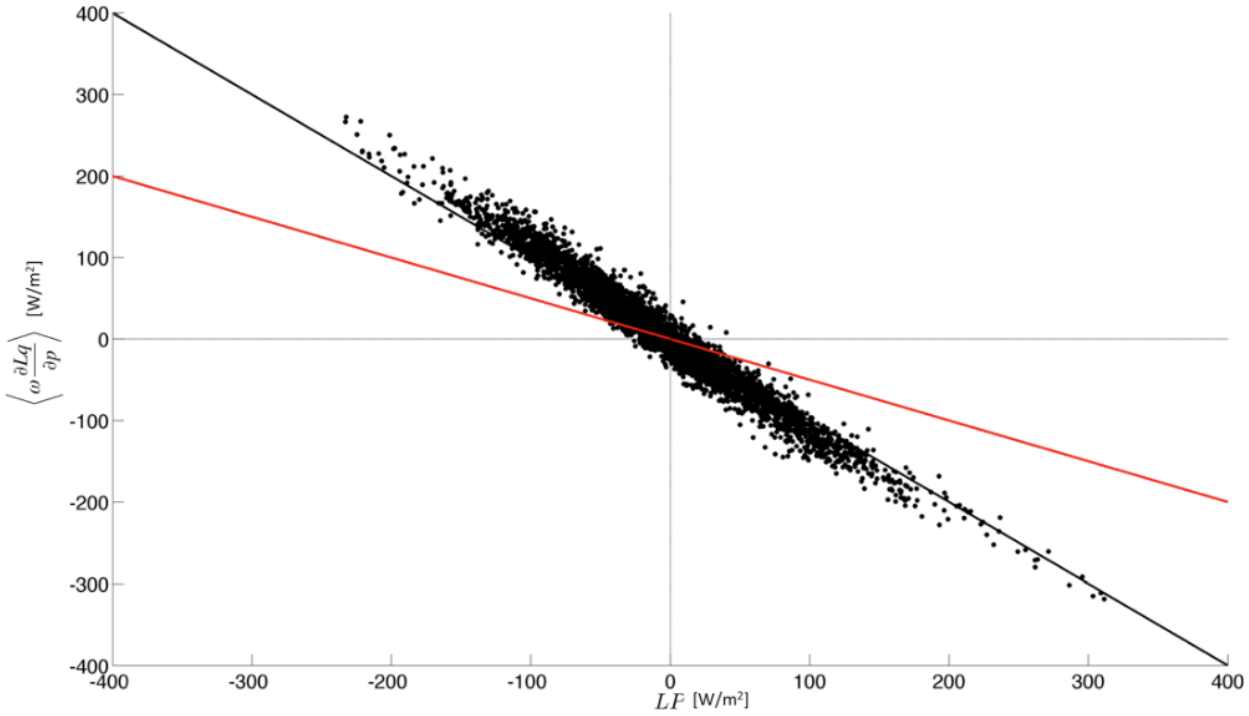

FIG. 3.28. A scatterplot of anomalous precipitation and anomalous vertical moisture advection in the central Indian Ocean, from 1981-2011, where both have been multiplied by the latent heat, L, in order to obtain units of watts per meter squared. Both terms were bandpass filtered to 20-100 days and spatially averaged from 4.5°N-4.5°S,70.5°E-79.5°E. Only days where the index amplitude exceeded 1 were included. The red line has a slope of -0.5, and is a reference for the values expected if the ratio of anomalous vertical moisture advection to precipitation remained at the climatological mean. The black line has a slope of -1, and is a reference for the values expected if anomalous vertical moisture advection exactly balanced anomalous precipitation. These lines have not been statistically fit to the data, and are included only to serve as a visual reference.

Figure 3.29 is a scatterplot of anomalous precipitation and the net affects of anomalous vertical moisture advection and anomalous precipitation in the central Indian Ocean. The

line of best fit is plotted in red and has a slope of -0.134. Correlation analysis resulted in an r value of -0.53 that was statistically significant at 95%. Anomalous net moistening (negative values on the y-axis) tends to occur during periods of anomalously high precipitation, while anomalous net drying (positive values on the y-axis) tends to occur during period of anomalously low precipitation. The results of Kiranmayi and Maloney (2011) support this finding. Considering the approximate quadrature relationship between $\langle q \rangle$ anomalies and both LH and $-\langle \vec{v} \cdot \nabla h \rangle$ anomalies in the Indian Ocean, this suggests that anomalous vertical moisture advection is the primary mechanism that supports anomalous precipitation. In other words, anomalous vertical moisture advection appears to be allowing extended periods of enhanced or suppressed precipitation to be sustained or potentially enhanced, even though latent heat fluxes and horizontal advective drying are occurring near their climatological values. No physical mechanism is proposed by this study to explain this relationship.

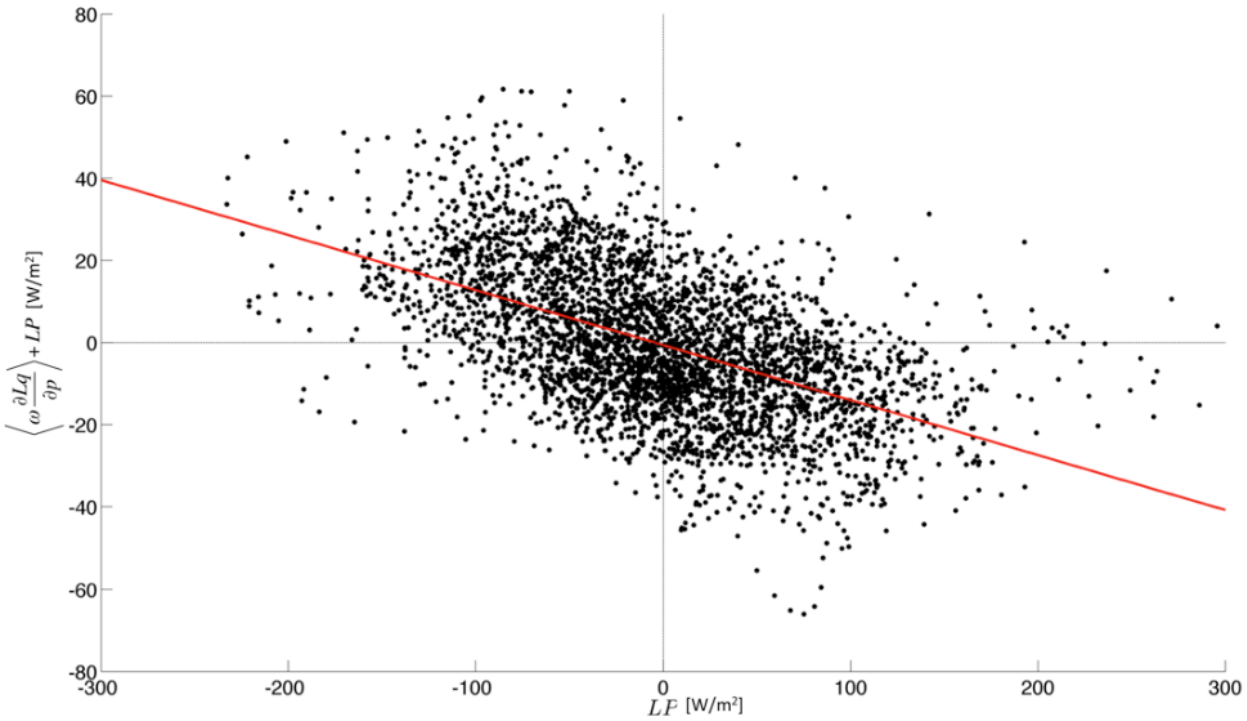

FIG. 3.29. A scatterplot of anomalous precipitation and the net affects of anomalous vertical moisture advection and anomalous precipitation in the central Indian Ocean, from 1981-2011. All terms have been multiplied by the latent heat, L, in order to obtain units of watts per meter squared. All terms were bandpass filtered to 20-100 days and spatially averaged from 4.5°N-4.5°S,70.5°E-79.5°E. Only days where the index amplitude exceeded 1 were included. The line of best fit is plotted in red. Negative(positive) values on the y-axis correspond to moistening(drying).

Figure 3.30 demonstrates that LH anomalies incompletely opposes horizontal advection anomalies, which are the dominant driver of MSE tendency in this study. Both Kiranmayi and Maloney (2011) and Wu and Deng (2013) found that surface flux anomalies were of larger amplitude than horizontal advection anomalies, which is the largest distinction between the findings of this study and those. The substantial residual of these two processes suggests that they may help determine the propagation characteristics of the MJO. The net affects of these processes remain substantial during considerable portions of the enhanced and suppressed

convective phases, suggesting that they may still play an important role in the destabilization and/or maintenance of the MJO.

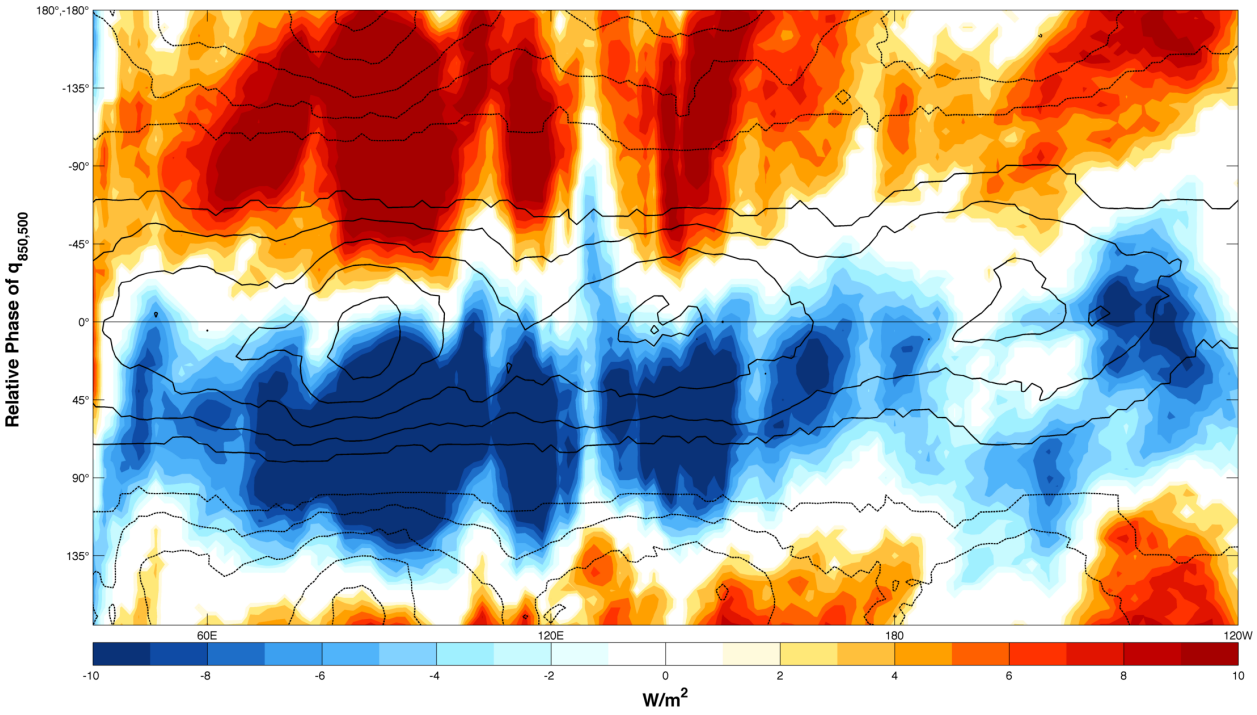

FIG. 3.30. As in Figure 3.15, except color contours are LH $-\langle \vec{v} \cdot \nabla h \rangle$ anomalies.

3.3.2. DECOMPOSITION OF HORIZONTAL ADVECTION TERMS

The large role of horizontal advection in driving MSE tendency motivates further investigation as to the underlying processes at work. Figures 3.31 and 3.32 show latitudinally averaged $-\left\langle u\frac{\partial h}{\partial x}\right\rangle$ and $-\left\langle v\frac{\partial h}{\partial y}\right\rangle$ as a function of relative phase of $q_{850,500}$ respectively. $-\left\langle v\frac{\partial h}{\partial y}\right\rangle$ is the dominant contributor to $-\langle \vec{v} \cdot \nabla h \rangle$ when considered over the broad region of 15°N-15°S, and has a very consistent phase relationship with $q_{850,500}$ across the entire eastern hemisphere. $-\left\langle u\frac{\partial h}{\partial x}\right\rangle$ is also a significant contributor to $-\langle \vec{v} \cdot \nabla h \rangle$, although the phase relationship with $q_{850,500}$ is not nearly as consistent. These results are consistent with the findings of Kiranmayi and Maloney (2011). $-\left\langle u\frac{\partial h}{\partial x}\right\rangle$ is roughly in phase or slightly leads $q_{850,500}$ in the western and central Indian Ocean, and is approximately in quadrature with

$q_{850,500}$ in the eastern indian ocean and over the Maritime Continent. There does not appear to be a clear signal between the Maritime Continent and the dateline, east of which $-\left\langle u\frac{\partial h}{\partial x}\right\rangle$ is in phase with $q_{850,500}$ and of larger amplitude.

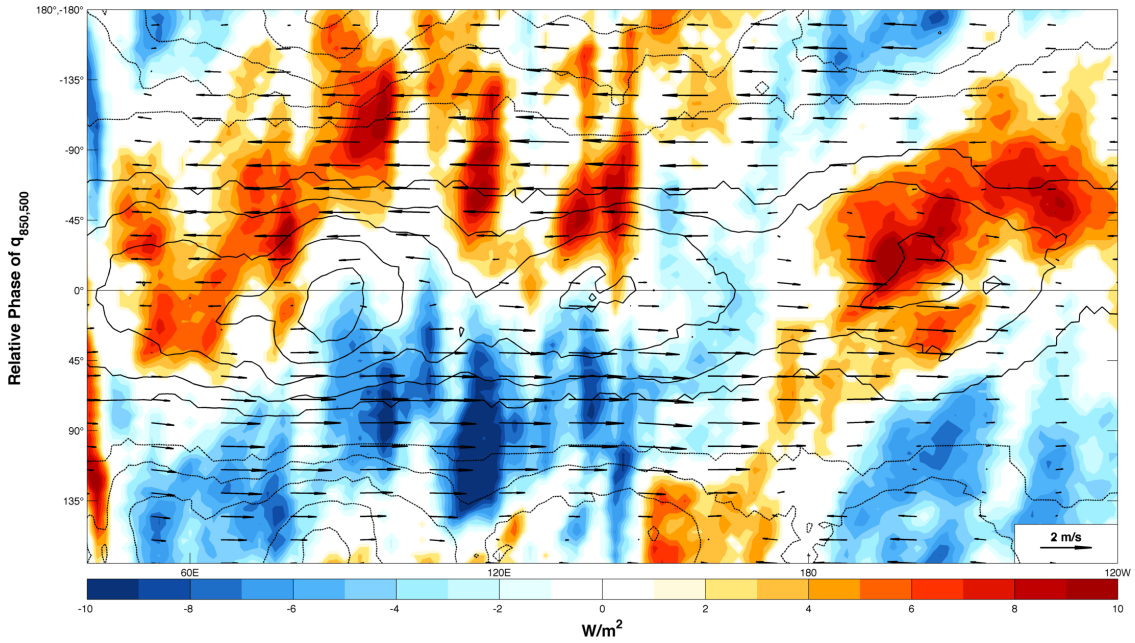

FIG. 3.31. As in Figure 3.15, except color contours are $-\left\langle u\frac{\partial h}{\partial x}\right\rangle$ anomalies.

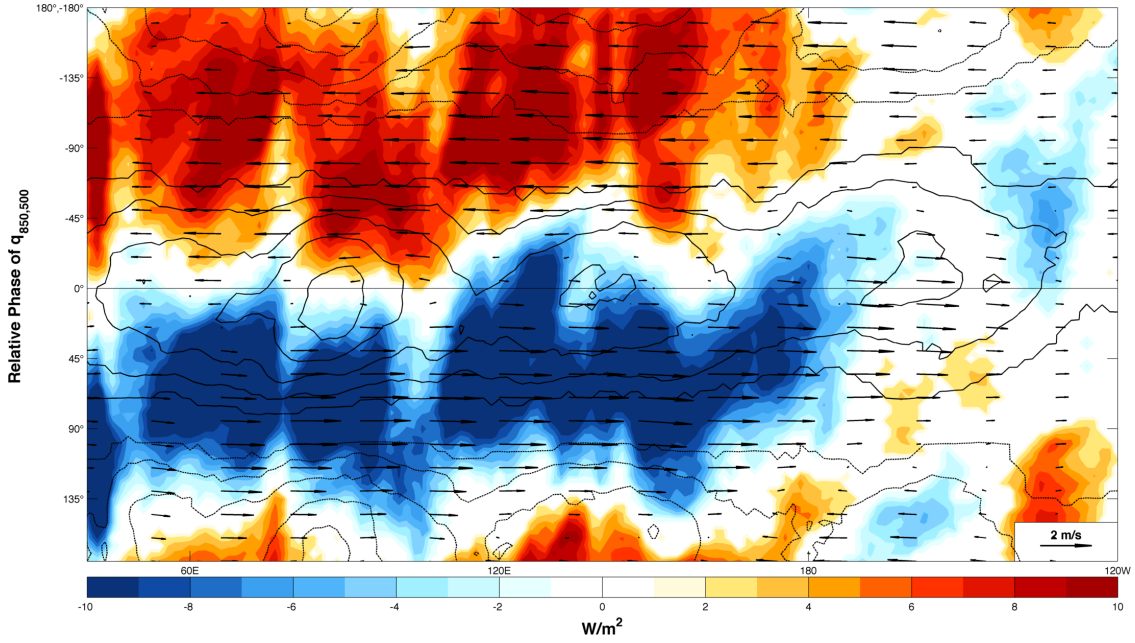

FIG. 3.32. As in Figure 3.15, except color contours are $-\left\langle v\frac{\partial h}{\partial y}\right\rangle$ anomalies.

Much greater insight to the physical mechanisms driving $-\left\langle u\frac{\partial h}{\partial x}\right\rangle$ and $-\left\langle v\frac{\partial h}{\partial y}\right\rangle$ can be gained from decomposing each term into its mean and eddy components. Recall that mean terms result from application of a 51-day running mean, and the prime terms are deviations from that running mean. Figure 3.33 shows latitudinally averaged $-\left\langle \overline{u}\frac{\partial h'}{\partial x}\right\rangle$ as a function of relative phase of $q_{850,500}$. While this term can be locally substantial for limited periods, there appears to be no consistent relationship between $-\left\langle \overline{u}\frac{\partial h'}{\partial x}\right\rangle$ and $q_{850,500}$ anomalies. Similarly, Figure 3.34 suggests that $-\left\langle \overline{v}\frac{\partial h'}{\partial y}\right\rangle$ plays little role in consistently modifying latitudinally averaged MSE, except for a potential small role in the western Indian Ocean where mean winds tend to have a more meridional component.

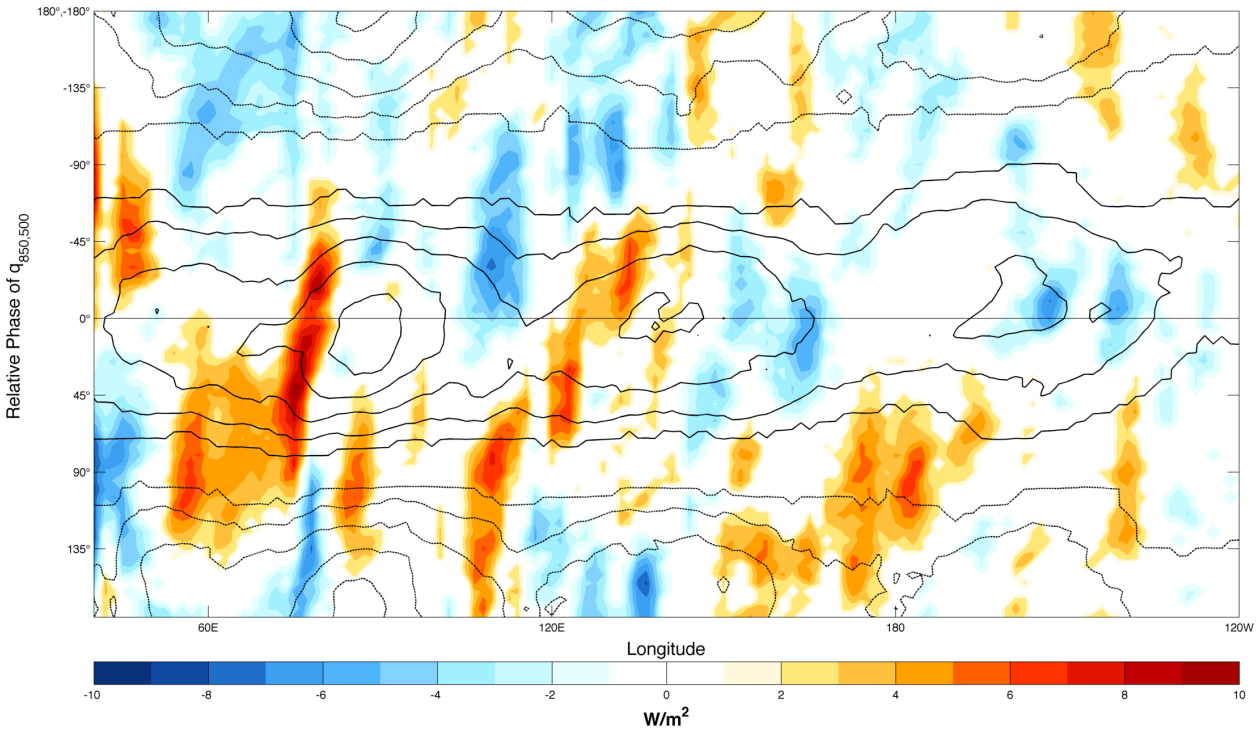

FIG. 3.33. As in Figure 3.10, except color contours are $-\left\langle \overline{u}\frac{\partial h'}{\partial x}\right\rangle$ anomalies.

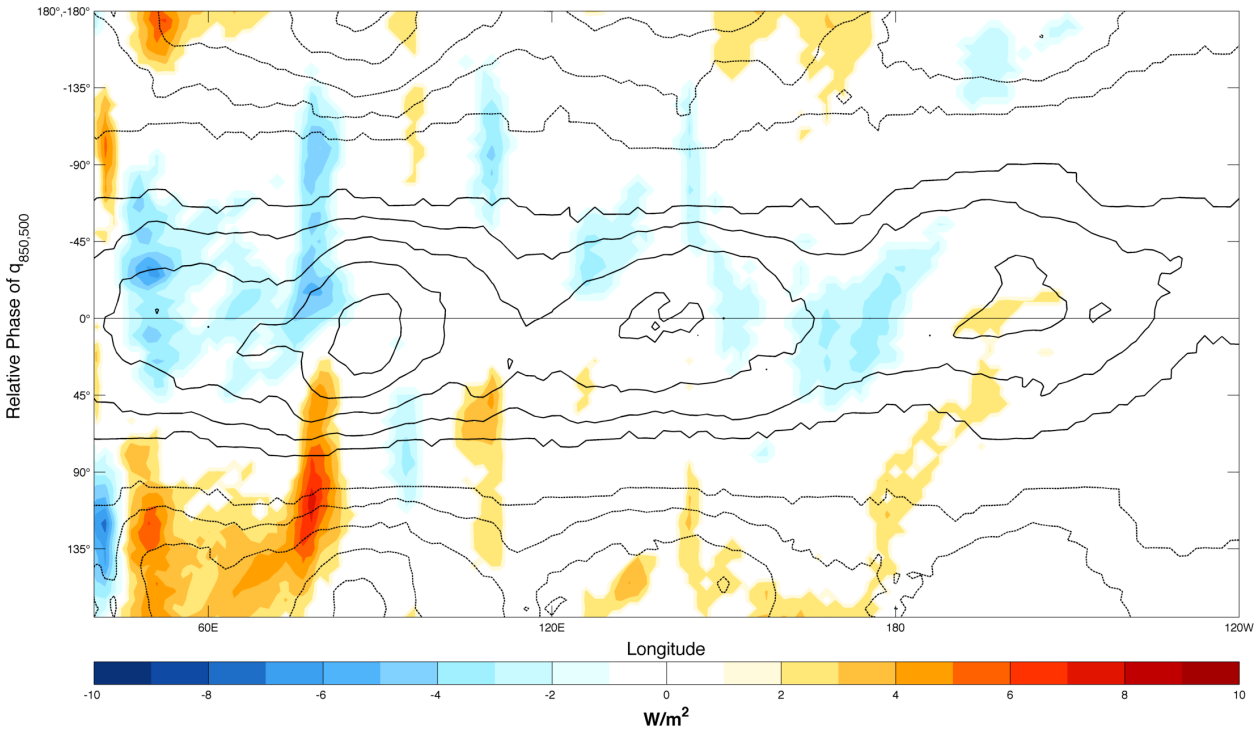

FIG. 3.34. As in Figure 3.10, except color contours are $-\left\langle \overline{v}\frac{\partial h'}{\partial y}\right\rangle$ anomalies.

In contrast, Figure 3.35 indicates that $-\left\langle u'\frac{\partial \overline{h}}{\partial x}\right\rangle$ has an important and consistent role in the Indian Ocean and the region of the maritime continent. This is consistent with the findings of Kiranmayi and Maloney (2011). Here $-\left\langle u'\frac{\partial \overline{h}}{\partial x}\right\rangle$ is approximately in quadrature with $q_{850,500}$ anomalies, acting to import MSE until near the peak in $q_{850,500}$. $-\left\langle u'\frac{\partial \overline{h}}{\partial x}\right\rangle$ is in phase with $q_{850,500}$ east of the dateline, where the time mean zonal moisture gradient decreases eastward and westerly U850 anomalies are located directly beneath maximum $q_{850,500}$ anomalies. The top (bottom) of Figure 3.36 shows U850 and $-\left\langle u'\frac{\partial \overline{h}}{\partial x}\right\rangle$ anomalies at 0° (−180/180°) relative phase of U850. As a reminder, this corresponds to the period of maximum U850 westerly(easterly) wind anomalies associated with the MJO at each location. $-\left\langle u'\frac{\partial \overline{h}}{\partial x}\right\rangle$ appears to play a especially large role equatorward of 10°. At the dateline, where the time mean zonal moisture gradient changes, $-\left\langle u'\frac{\partial \overline{h}}{\partial x}\right\rangle$ changes sign relative to the sign of the U850 anomalies. Also apparent is the role the Maritime Continent plays in introducing much of

the noise present in Figure 3.35. Figure 3.37 similarly indicates that $-\left\langle v'\frac{\partial\bar{h}}{\partial y}\right\rangle$ plays an important role in the Indian Ocean and Maritime continent. Figure 3.38 provides insight into the processes driving large anomalies in $-\left\langle v'\frac{\partial\bar{h}}{\partial y}\right\rangle$. The top(bottom) panel shows $-\left\langle v'\frac{\partial\bar{h}}{\partial y}\right\rangle$ anomalies composited over 66(63) individual events where positive(negative) $-\left\langle v'\frac{\partial\bar{h}}{\partial y}\right\rangle$ anomalies averaged from 15°N-15°S, 49.5°E-60°E exceeded one standard deviation. Only events separated by at least 20 days were included, and the MJO index amplitude needed to remain above 1 for at least 10 consecutive days following the day selected. This domain was chosen because it corresponds to the amplitude maximum observed in Figure 3.37. Rossby-gyre like circulations appear to be centered west of maximum $-\left\langle v'\frac{\partial\bar{h}}{\partial y}\right\rangle$ anomalies. The meridional components of this circulation, acting on the mean equator to pole moisture gradient, result in a moistening(drying) of the periphery of the tropics when U850 anomalies are convergent(divergent). $-\left\langle v'\frac{\partial\bar{h}}{\partial y}\right\rangle$ anomalies of lesser amplitude and opposite sign are observed to both the east and the west of the domain chosen here. Reasons for the geographical variations in phase and amplitude of this term, as seen in Figure 3.37, are less clear.

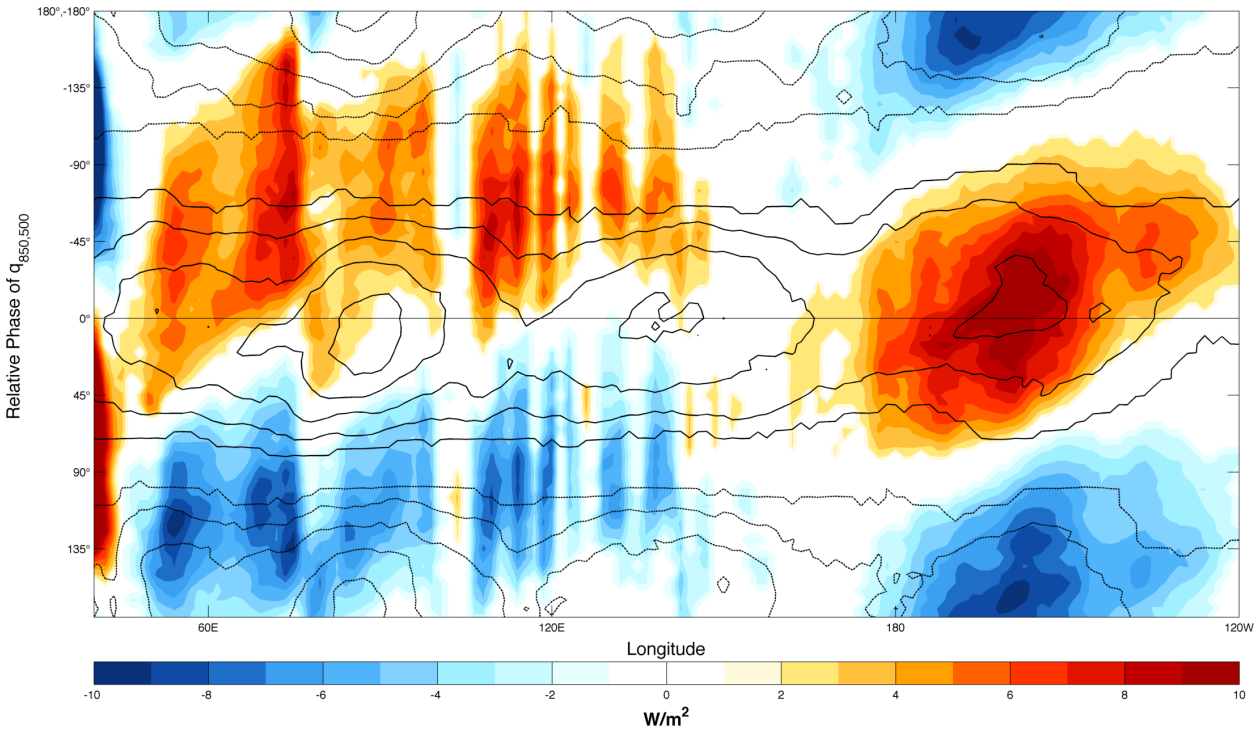

FIG. 3.35. As in Figure 3.10, except color contours are $-\left\langle u' \frac{\partial \bar{h}}{\partial x} \right\rangle$ anomalies.

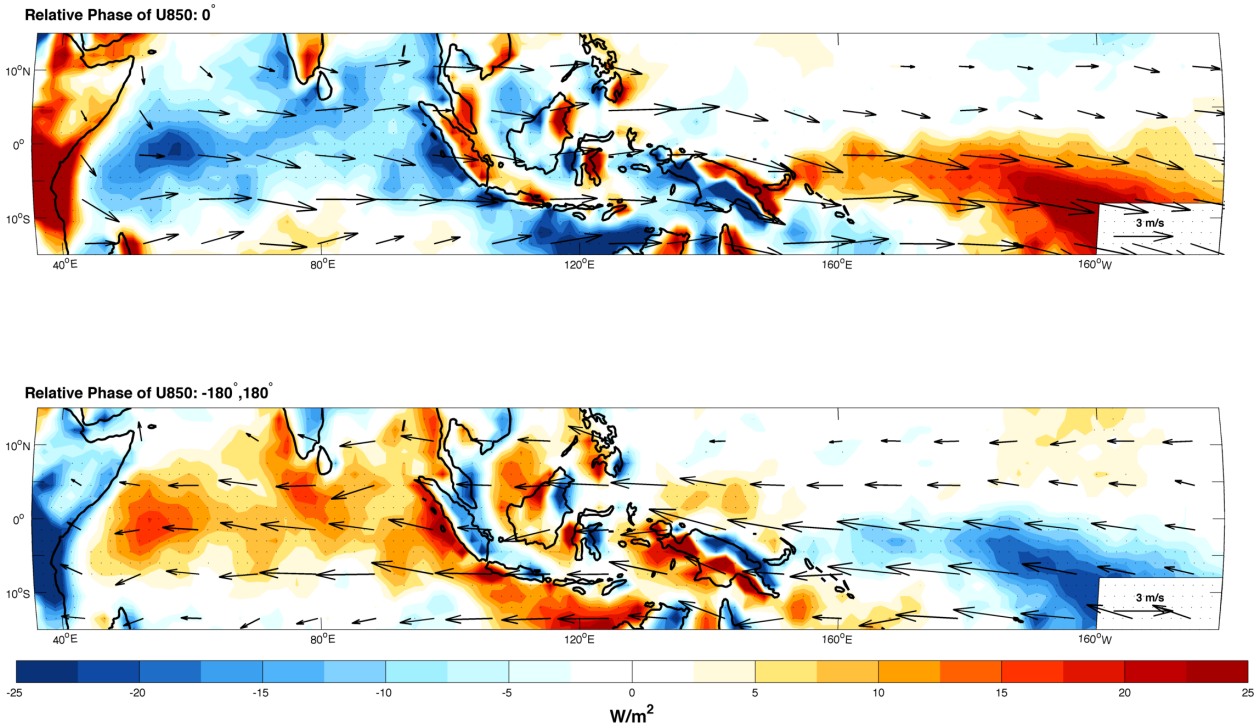

FIG. 3.36. As in Figure 3.22, except color contours are $-\left\langle u' \frac{\partial \bar{h}}{\partial x} \right\rangle$ anomalies.

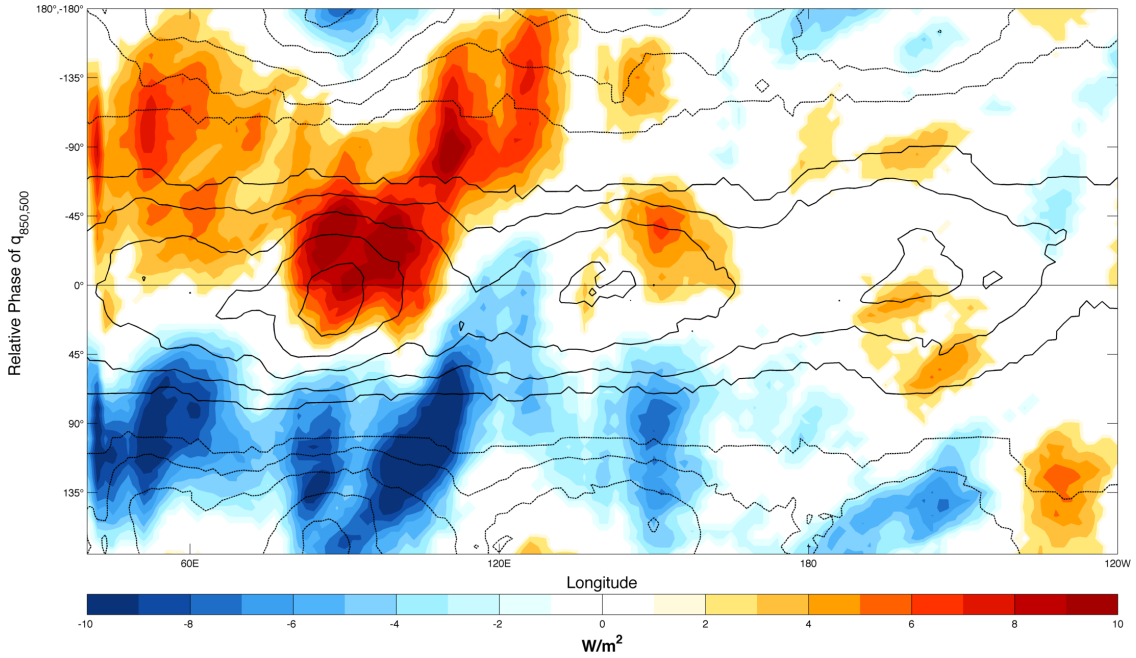

FIG. 3.37. As in Figure 3.10, except color contours are $-\left\langle v' \frac{\partial \bar{h}}{\partial y} \right\rangle$ anomalies.

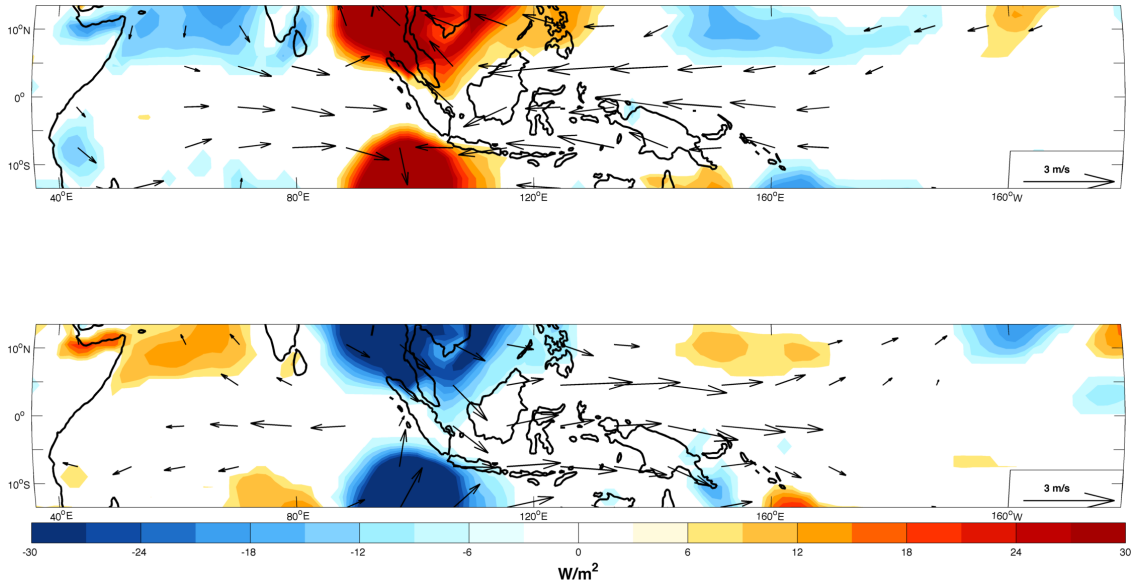

FIG. 3.38. The top(bottom) panel shows $-\left\langle v' \frac{\partial \bar{h}}{\partial y} \right\rangle$ anomalies composited over 66(63) individual events where positive(negative) $-\left\langle v' \frac{\partial \bar{h}}{\partial y} \right\rangle$ anomalies averaged from 15°N-15°S, 49.5°E-60°E exceeded one standard deviation. Individual events included in the composite are separated by at least 20 days, and the MJO index amplitude remained above 1 for at least 10 consecutive days following the day selected.

Figures 3.39 and 3.40 show that $-\left\langle u'\frac{\partial h'}{\partial x}\right\rangle$ and $-\left\langle v'\frac{\partial h'}{\partial y}\right\rangle$ are similar in their phase relationships to $q_{850,500}$ anomalies, though the amplitude of the anomalies are less in $-\left\langle u'\frac{\partial h'}{\partial x}\right\rangle$. Both $-\left\langle u'\frac{\partial h'}{\partial x}\right\rangle$ and $-\left\langle v'\frac{\partial h'}{\partial y}\right\rangle$ anomalies appear to be roughly out of phase with $q_{850,500}$ anomalies and lagging between 0° and 45° in phase. Comparisons with 850 hPa eddy kinetic energy (EKE), shown in Figure 3.41, suggest a similar relationship as that proposed by Maloney (2009) and Kiranmayi and Maloney (2011) to explain modulation of $-\left\langle v'\frac{\partial h'}{\partial y}\right\rangle$. As in Maloney (2009) and Kiranmayi and Maloney (2011), EKE has been defined as $\frac{u''^2+v''^2}{2}$, where the double prime represents deviations from an 11-day running mean. Maximum(minimum) EKE occurs about 45° after the peak(minimum) in $q_{850,500}$. These results are consistent with the findings of Maloney and Dickinson (2003), who showed that synoptic scale eddies such as easterly waves and TD-type disturbances are enhanced(suppressed) during westerly(easterly) phases of the MJO. Figure 3.42, which shows high frequency contributions to the anomalous zonal and meridional eddy transport terms, also supports this suggested mechanism. Here a 20 day high-pass filter was applied to u',v' and h' before calculate of the various eddy transport terms, which were then bandpass filtered. Clearly the high frequency components dominate the eddy transport terms. These results are consistent with the findings of Maloney (2009) and Kiranmayi and Maloney (2011).

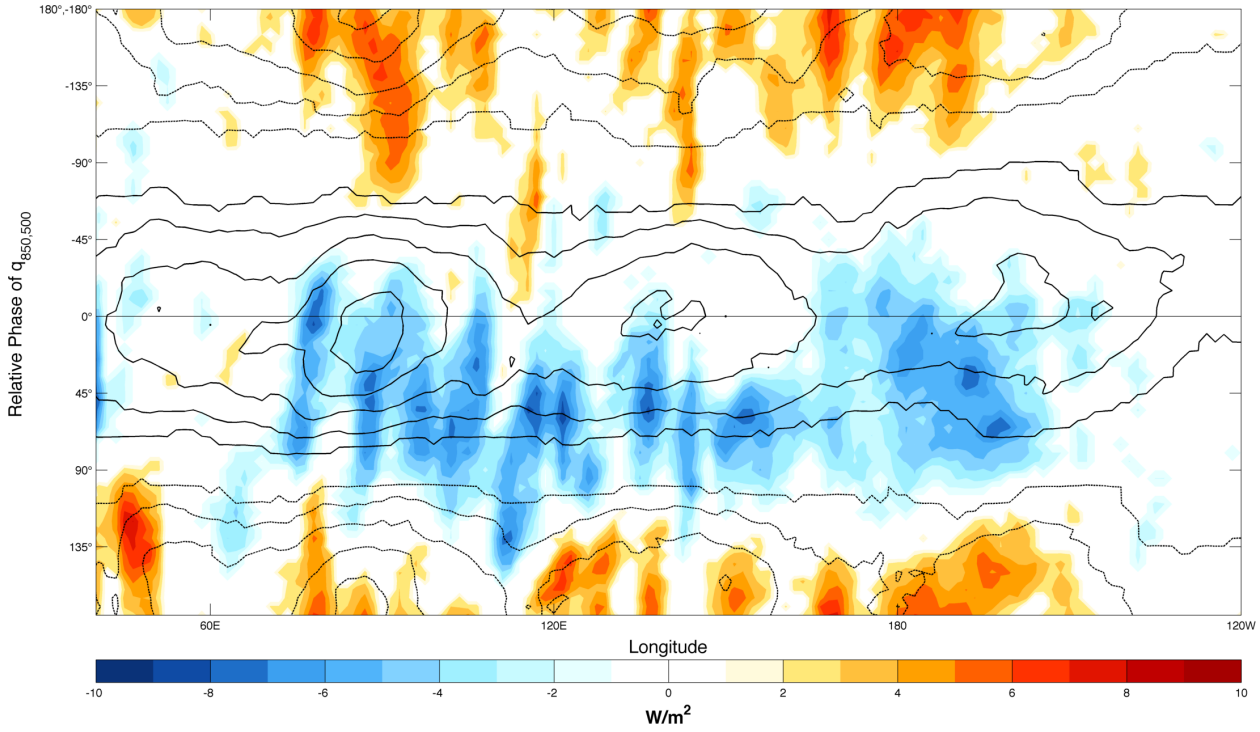

FIG. 3.39. As in Figure 3.10, except color contours are $-\left\langle u' \frac{\partial h'}{\partial x} \right\rangle$ anomalies.

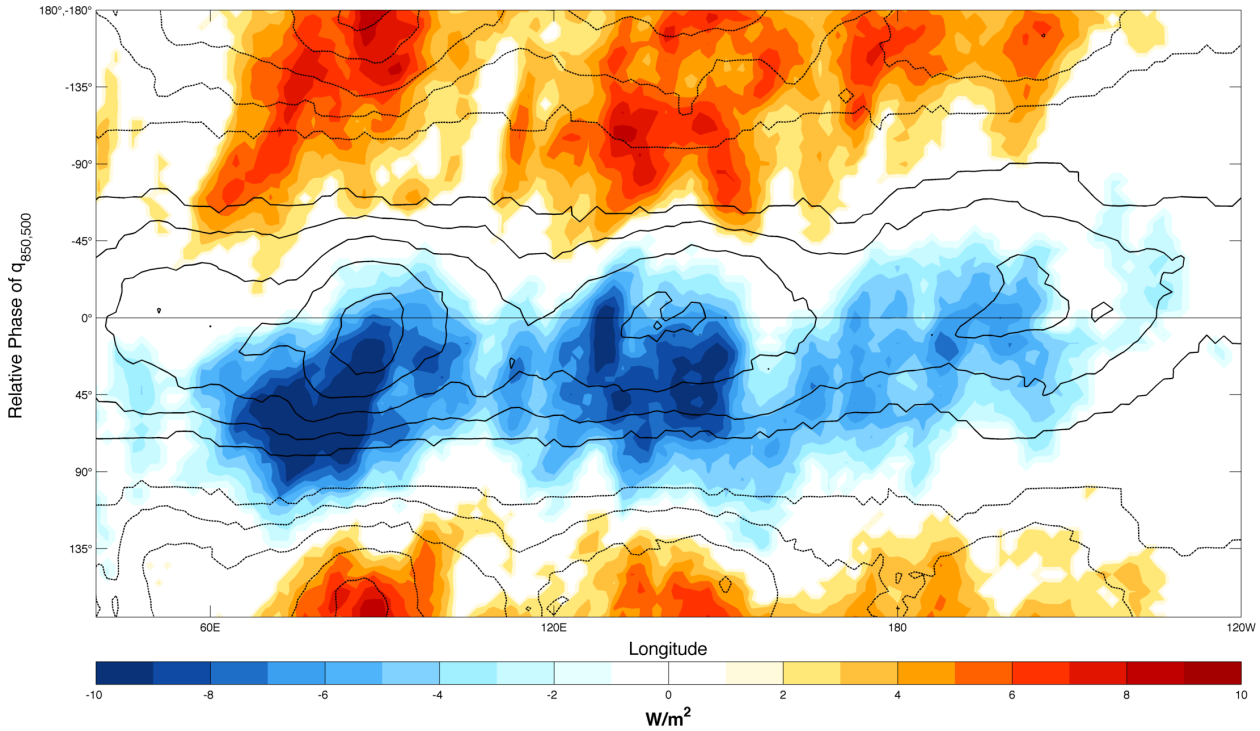

FIG. 3.40. As in Figure 3.10, except color contours are $-\left\langle v' \frac{\partial h'}{\partial y} \right\rangle$ anomalies.

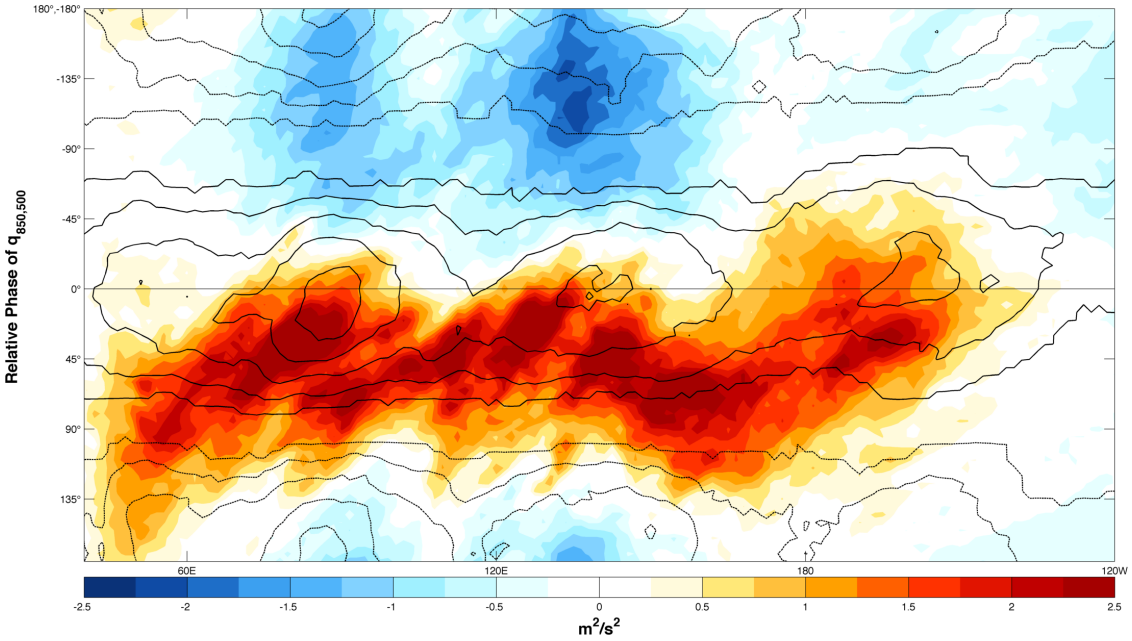

FIG. 3.41. As in Figure 3.10, except color contours are eddy kinetic energy anomalies at 850 hPa.

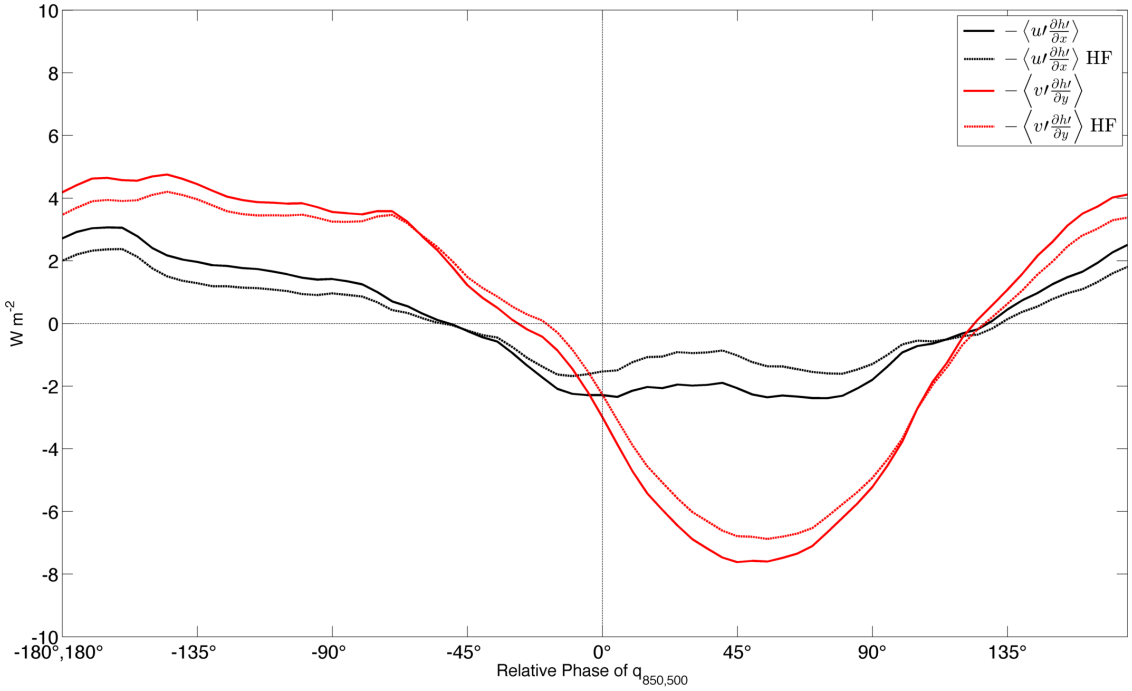

FIG. 3.42. High frequency contribution to anomalous vertically integrated zonal and meridional eddy transport of MSE, as a function of relative phase of $q_{850,500}$. Budget terms were averaged over the Indian Ocean (15°N-15°S,50°E-95°E).

3.4. Indian Ocean MSE Budget

Examining the geographical variability of the various terms in the MSE budget has provided many important insights to the physical processes that modulate MSE. While notable geographical differences have been identified, it has also been shown that the processes driving MSE modulation appear to be remarkably consistent across the Indian Ocean (and to a lesser extent the Maritime Continent). This motivates representation of the fundamental processes associated with the MJO in the Indian Ocean by a single MSE budget. This is done in the hope of providing a succinct model of the processes modulating $\langle h \rangle$ and $\langle Lq \rangle$ throughout an MJO lifecycle, reduced of unnecessary complexity.

Figure 3.43 shows $\langle h \rangle$ anomalies and $L * q_{850,500}$ anomalies as a function of relative phase of $q_{850,500}$. $L * q_{850,500}$ anomalies make up $\sim 70\%$ of $\langle h \rangle$ anomalies. Both $\langle h \rangle$ and $L * q_{850,500}$ anomalies peak at about 15° relative phase. This means that, in an area average sense, the grid point phase estimate of the index phase at which $q_{850,500}$ anomalies would peak was approximately 15° earlier than the true index phase they maximized at. This is an error of $\sim 4\%$ of a lifecycle. A potential source for this error may be the application of the compositing technique to bandpass filtered data, even though the CEOF was calculated using unfiltered data. For ease of interpretation, subsequent figures will be shifted by 15° relative phase (denoted as adjusted relative phase) such that $q_{850,500}$ anomalies maximize at 0° adjusted relative phase.

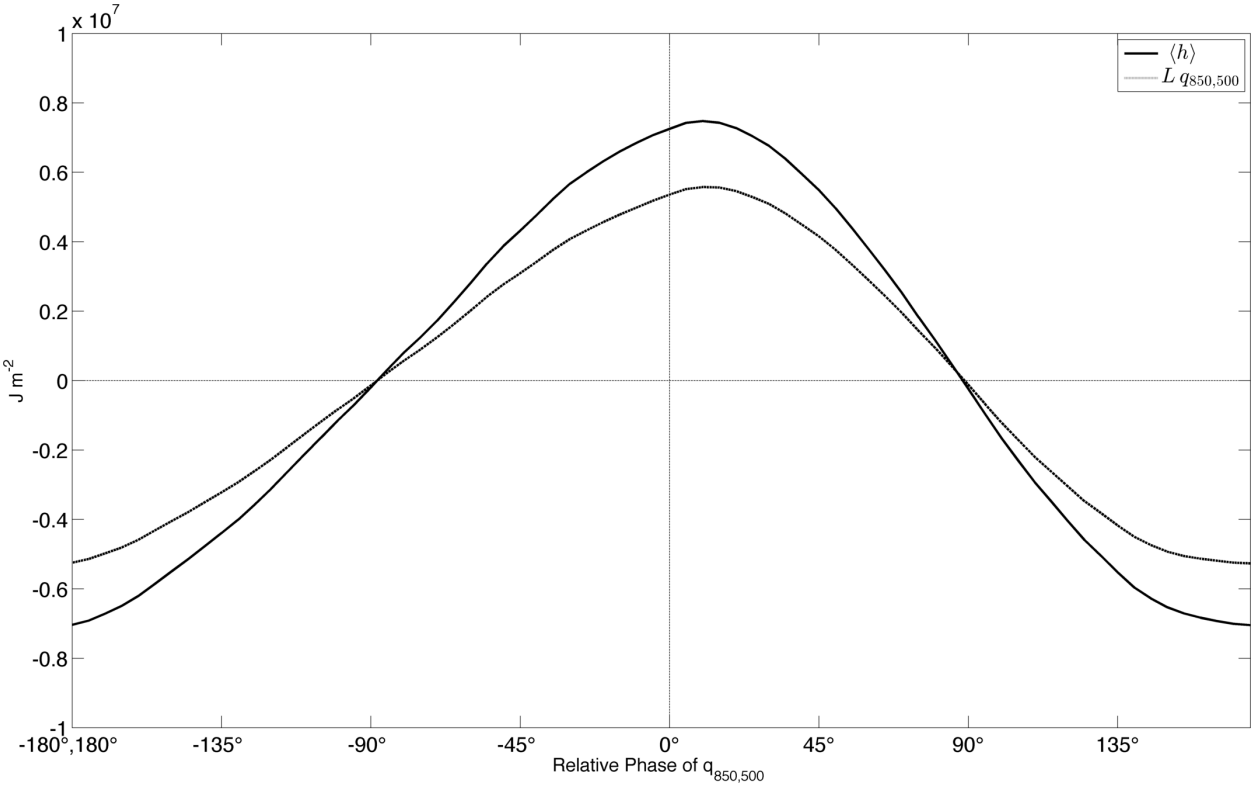

FIG. 3.43. Vertically integrated MSE anomalies and $L * q_{850,500}$ anomalies as a function of relative phase of $q_{850,500}$.

Figure 3.44 shows the MSE budget for the Indian Ocean as a function of adjusted relative phase of $q_{850,500}$. $\langle h \rangle$ anomalies and $\langle Lq \rangle$ anomalies are approximately in phase with $\langle Q_r \rangle$ and SH anomalies (not shown), and approximately out of phase with $-\left\langle \omega \frac{\partial h}{\partial p} \right\rangle$ anomalies. $\left\langle \frac{\partial h}{\partial t} \right\rangle$ is approximately in phase with $-\langle \vec{v} \cdot \nabla h \rangle$ anomalies and approximately out of phase with LH anomalies. Equation 1.19 suggests that net affect of anomalous vertical moisture advection and anomalous precipitation is resulting in an anomalous moistening during periods of enhanced convection and anomalous drying during periods of suppressed convection. This appears to be what allows enhanced convection to be sustained even though both LH and $-\langle \vec{v} \cdot \nabla h \rangle$ are anomalously negative at the peak of anomalous convection. The incomplete offset of $-\langle \vec{v} \cdot \nabla h \rangle$ anomalies by LH anomalies throughout the MJO lifecycle appears to be the primary driver of $\left\langle \frac{\partial h}{\partial t} \right\rangle$. To the extent that the studies are comparable, the MSE budget

presented here largely agrees with those presented in Kiranmayi and Maloney (2011) and Wu and Deng (2013), with the previously mentioned disagreement on the relative amplitudes of horizontal advection anomalies and surface flux anomalies.

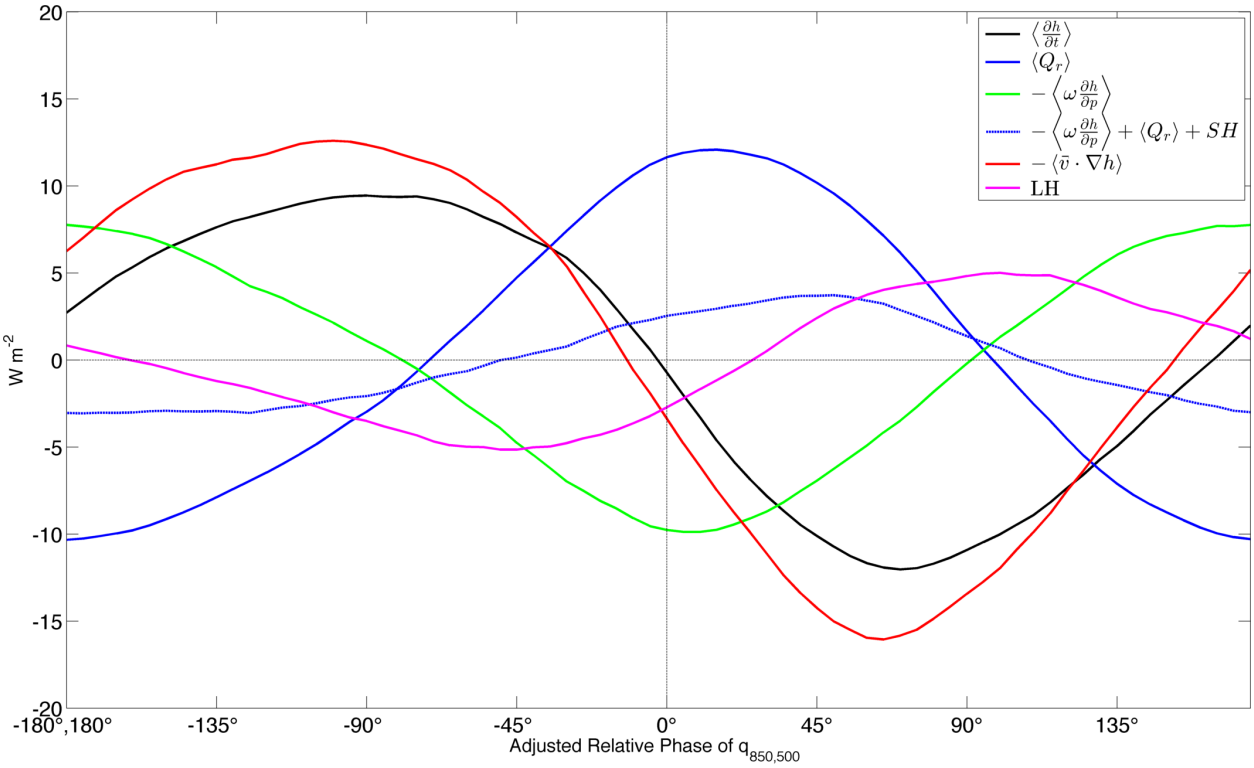

FIG. 3.44. Vertically integrated anomalous MSE budget terms from equation 1.15, as a function of adjusted relative phase of $q_{850,500}$. Budget terms were averaged over the Indian Ocean (15°N-15°S,50°E-95°E).

Figure 3.45 shows $-\left\langle u\frac{\partial h}{\partial x}\right\rangle$, $-\left\langle \overline{u}\frac{\partial h'}{\partial x}\right\rangle$, $-\left\langle u'\frac{\partial \overline{h}}{\partial x}\right\rangle$, and $-\left\langle u'\frac{\partial h'}{\partial x}\right\rangle$ as a function of adjusted relative phase of $q_{850,500}$. The role of $-\left\langle u'\frac{\partial \overline{h}}{\partial x}\right\rangle$ in driving $-\left\langle u\frac{\partial h}{\partial x}\right\rangle$ is clear, although it is partially offset by the other terms. This is consistent with the findings of Kiranmayi and Maloney (2011). When considered from $15°\text{N}-15°\text{S}$, $-\left\langle \overline{u}\frac{\partial h'}{\partial x}\right\rangle$ is nearly as large as $-\left\langle u'\frac{\partial \overline{h}}{\partial x}\right\rangle$, though 2-D plots of $-\left\langle \overline{u}\frac{\partial h'}{\partial x}\right\rangle$ do not show the spatial or temporal consistency of $-\left\langle u'\frac{\partial \overline{h}}{\partial x}\right\rangle$. There is a notable increase in the strength of $-\left\langle u'\frac{\partial \overline{h}}{\partial x}\right\rangle$ when averaged only from $5°\text{N}-5°\text{S}$. This is not surprisingly considering how much larger the zonal moisture gradient is near

the equator than at the periphery of the tropics. Zonal eddy transport appears to play a relatively minor role in the Indian Ocean.

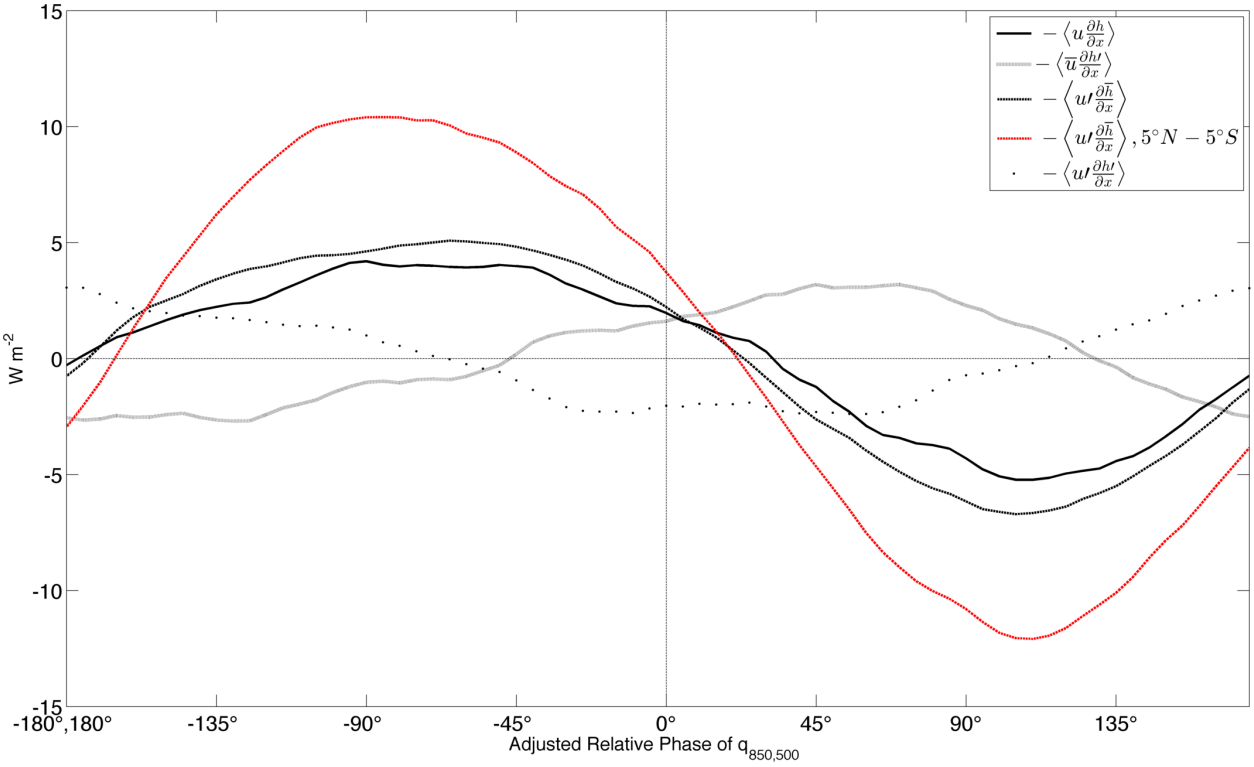

FIG. 3.45. As in Figure 3.44, except for the partitioning of the anomalous zonal advection term.

Figure 3.46 shows $-\left\langle v\frac{\partial h}{\partial y}\right\rangle$, $-\left\langle \overline{v}\frac{\partial h'}{\partial y}\right\rangle$, $-\left\langle v'\frac{\partial \overline{h}}{\partial y}\right\rangle$, and $-\left\langle v'\frac{\partial h'}{\partial y}\right\rangle$ as a function of adjusted relative phase of $q_{850,500}$. Both $-\left\langle v'\frac{\partial \overline{h}}{\partial y}\right\rangle$ and $-\left\langle v'\frac{\partial h'}{\partial y}\right\rangle$ appear to play important roles in driving $-\left\langle v\frac{\partial h}{\partial y}\right\rangle$, and are offset by $\sim 45°$ in phase from each other. There is a notable decrease in the strength of $-\left\langle v'\frac{\partial \overline{h}}{\partial y}\right\rangle$ when averaged only from 5°N−5°S. This, taken together with Figure 3.42, suggests that $-\left\langle v'\frac{\partial \overline{h}}{\partial y}\right\rangle$ plays an important role in moistening(drying) the periphery of the tropics during periods of enhanced(suppressed) convection. Advection of moisture anomalies by the mean state meridional winds appears to play a relatively minor role. The results of Kiranmayi and Maloney (2011) were not consistent among the two locations studied in the Indian Ocean, making a comparison of results difficult.

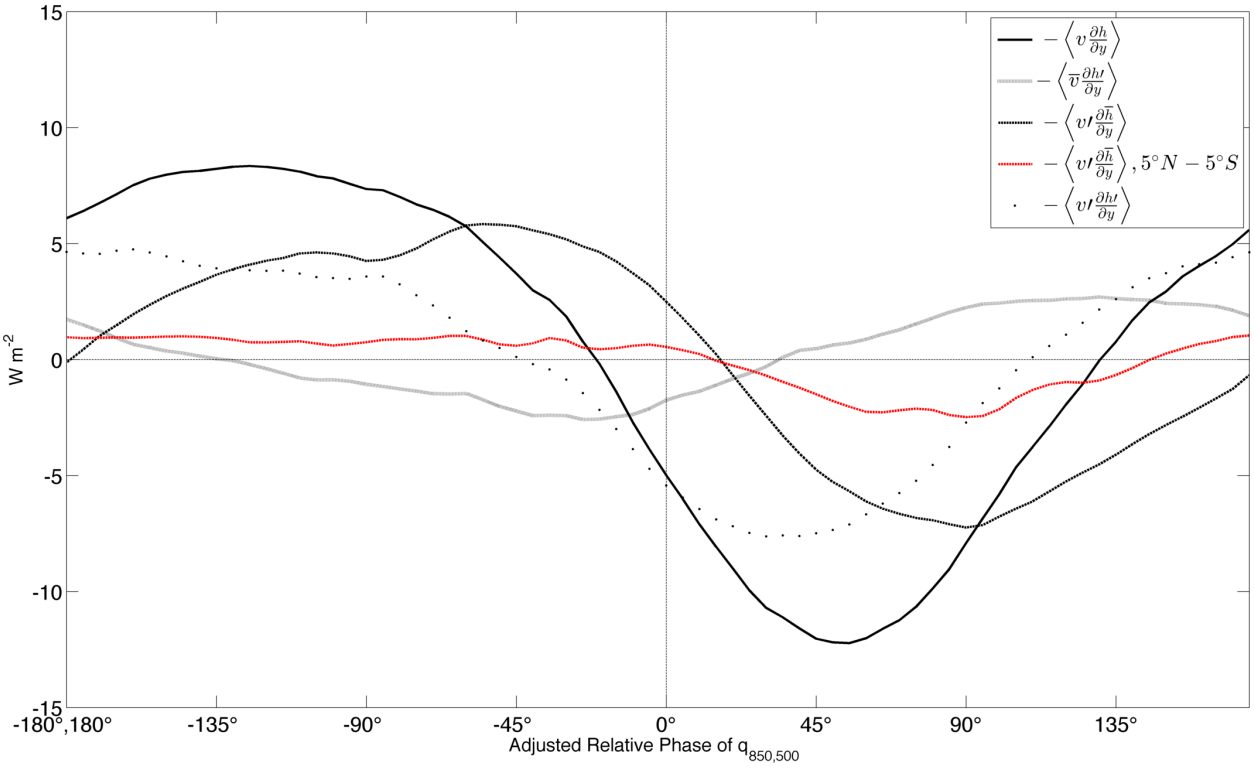

FIG. 3.46. As in Figure 3.44, except for the partitioning of the anomalous meridional advection term.

3.5. INITIATION BUDGET RESULTS

A brief discussion of the compositing technique used here, in the context of previous studies, is warranted. As mention in the introduction, Straub (2013) has shown that the RMM index is predominantly driven by the wind signal of the MJO. Difficulties arise when trying to composite convective initiation based on such an index, as strong projections of wind anomalies remote to the region of interest may provide a "false-positive" for the onset of anomalous deep convection. Similar issues arise if initiation is defined using an index based on the convective signal alone, as such an index provides no assessment of the presence of a MJO-like dynamical signal. As has already been shown, the index used in this study is influenced disproportionately by anomalies in U850 and U200. Complications in compositing associated with this disproportionate influence are avoided by using an initiation index based

on grid point contribution, the details of which are provided in the Data and Methodology section. This ensures that a substantial convective anomaly that projects strongly onto the CEOF structure is present over the initiation domain on day 0, enhancing the signal to noise ratio by reducing "false-positive" events.

Figure 3.47 shows composite U850 wind anomalies, OLR anomalies and $q_{850,500}$ anomalies from day -30 to day 5. These fields have not been subjected to bandpass filtering. A stationary region of suppressed convection appears to be present in the central and eastern Indian Ocean from day -30 to day -15. It is difficult ascertain if this is truly a stationary anomaly of suppressed convection, or the result of the superposition of different precursor suppressed phases associated with successive events. More notable are the positive $q_{850,500}$ anomalies that develop in the initiation region and north Africa by day -15, along with equatorial easterly U850 anomalies spanning from the Maritime Continent to the western Indian Ocean. The initial development of positive $q_{850,500}$ anomalies is collocated in time and space with the onset of easterly U850 anomalies. At this point there is no evidence of a circumnavigating U850 anomalies. Between day -15 and day -5 positive $q_{850,500}$ anomalies develop into a notable tongue of enhanced moisture that extends across the Indian Ocean, centered just north of the equator. The development of the $q_{850,500}$ is coincident with the enhancement and eastward extension of the easterly U850 anomalies. A circumnavigating wind signal is evident at day -10, but is still remote from the initiation region and of low amplitude, suggesting it is not associated with the development of enhanced moisture over the initiation domain. This is consistent with the findings of Zhao et al. (2013). Convection over the Maritime Continent between these time period is substantially more suppressed, and shows characteristics of propagation. Again, it is difficult to discern if these suppressed

anomalies "develop", or are the results of a more coherent superposition of precursor events as "Day 0" is approached. While enhanced convection over the Indian Ocean is evident at day -5, it undergoes remarkable enhancement between day -5 and day 0. This is coincident with the onset of westerly U850 anomalies to the west of the region of enhanced convection, and the onset of propagation is evident after this point. At all lags in this composites, minimum OLR values are collocated with maximum values in $q_{850,500}$. It is worth highlighting that the buildup of $q_{850,500}$ anomalies was initiated a full 15 days prior to the onset of the deepest convection over the initiation region. These results are largely consistent with the findings of Matthews (2008), Straub (2013) and Zhao et al. (2013), though details of the timing vary among these studies. Matthews (2008) did not find a buildup of moisture anomalies prior to primary initiation events, but in that study the analysis of moisture was limited to the 1000 hPa level were anomalies may be smaller than in the free troposphere.

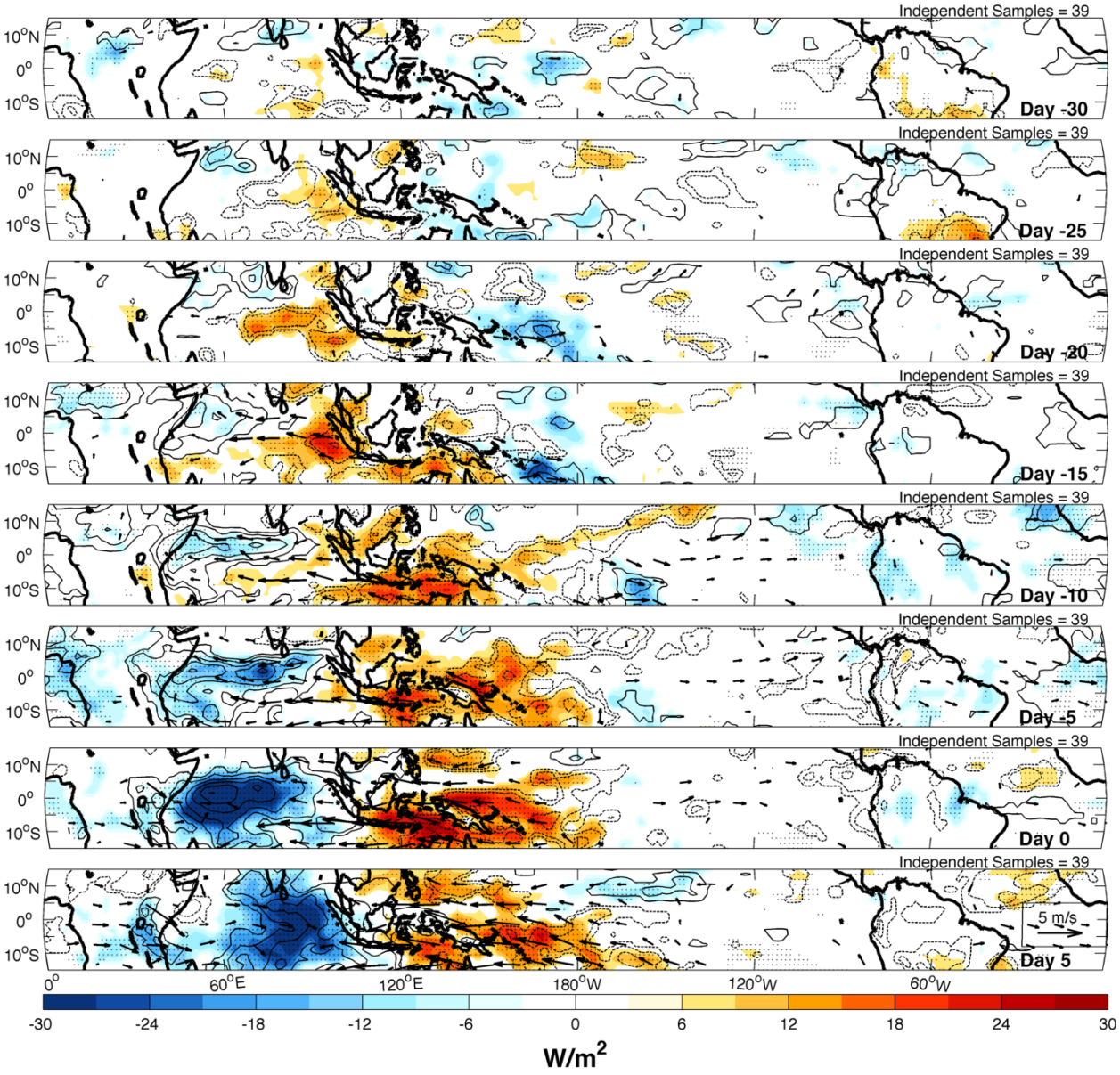

FIG. 3.47. ERAi composite of $q_{850,500}$ anomalies(contours), OLR anomalies (colored contours), and 850 hPa horizontal wind anomalies from day -30 to day 5 for the initiation budget. Bandpass filtering was not applied to these fields. Solid (dashed) contours are positive (negative) $q_{850,500}$ anomalies of 0.5,1.5,2.5,3.5 (-0.5,-1.5,-2.5,-3.5) $\mathrm{kg\,kg^{-1}}$. Wind vectors are statistically significant at the 95% level. A reference wind vector is provided in the lower right corner of the bottom panel. Stippling indicates OLR anomalies significant at the 95% level.

Figure 3.48 shows composite $\langle h \rangle$ anomalies and $L * q_{850,500}$ anomalies (both bandpass filtered and non bandpass filtered) at different lag times. Of particular importance is the

substantial differences between the bandpass filtered and non bandpass filtered $L * q_{850,500}$ anomalies. In the non bandpass filtered case, a slow buildup of $q_{850,500}$ occurs over the course of 20 days, peaking at day 0. This is immediately followed by a rapid reduction of the $q_{850,500}$ anomalies over the course of 5 days, followed by a more gradual drying between days 5 and 10 that causes substantial negative $q_{850,500}$ anomalies. The application of the bandpass filter clearly introduces several spurious features into the results. Most notably, the peak in $q_{850,500}$ is shifted by approximately 5 days. Also, the amplitude of the maximum and minimum anomalies are made to be much more symmetrical than are observed in the non band passed values. As has been demonstrated several times, $\langle h \rangle$ anomalies are primarily the result of $q_{850,500}$ anomalies. Therefore, it is a reasonable assumption $\langle h \rangle$ has suffered a similar artificial phase shift, and may in fact peak near "Day 0". The potential affects of bandpass filtering on the phase relationships of the various terms presented in this study is a qualification that should discourage the over interpretation of results stemming from phase lags on the order of a few days or similarly small increments of relative phase.

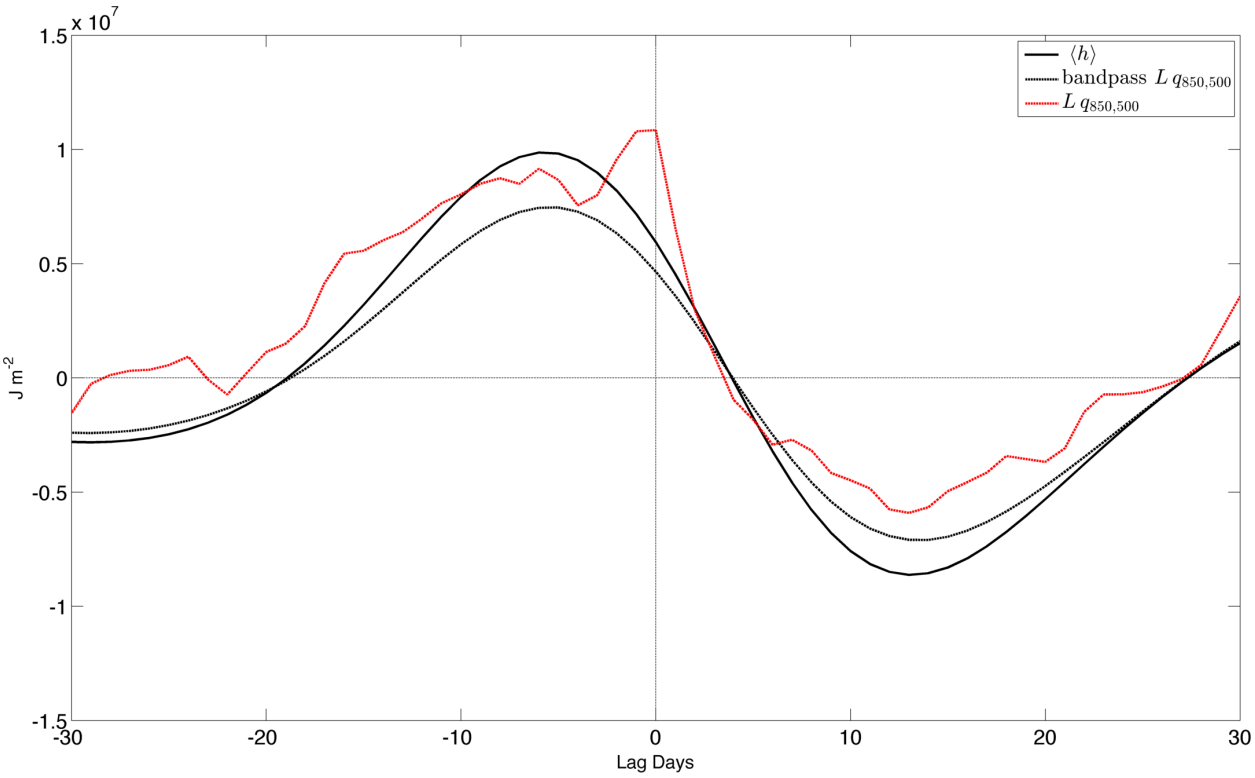

FIG. 3.48. Vertically integrated MSE anomalies, $L * q_{850,500}$ anomalies and bandpass filtered $L * q_{850,500}$ anomalies as a function of relative phase of $q_{850,500}$ for days -30 to 30 of the initiation budget.

Figure 3.49 shows the composite MSE budget for the initiation domain. Note that $\left\langle \frac{\partial h}{\partial t} \right\rangle$ becomes negative at day -5, likely the result of the aforementioned bandpass filtering affects. During the transition from suppressed convection to enhanced convection, horizontal advection is a major source of anomalous moistening, opposed by LH anomalies of a smaller amplitude. Figure 3.47 shows that easterly U850 anomalies are present over the initiation region during this period. Vertical MSE advection anomalies are out of phase with radiative heating anomalies and SH anomalies. The net affects of these processes, considered under WTG balance, suggest that anomalous vertical moisture advection is exceeding anomalous precipitation from day -20 to day 5, resulting in a anomalous moistening. Taken in consideration with Figure 3.47, which shows that large scale convective anomalies are fully developed

over the initiation region by day 0, suggests that very large vertical moisture advection anomalies must be present to offset the moisture loss due to anomalous precipitation likely occurring in the region. Both horizontal advection anomalies and LH anomalies switch sign between day -5 and day 0, coincident with the onset of westerly U850 anomalies observed in Figure 3.47.

Comparison of figures 3.50 and 3.51 suggests that $-\langle \vec{v} \cdot \nabla h \rangle$ is primarily driven by $-\left\langle u \frac{\partial h}{\partial x} \right\rangle$, which is largely the results of $-\left\langle u' \frac{\partial \overline{h}}{\partial x} \right\rangle$. This suggests that easterly anomalies advecting moisture down the mean moisture gradient are an important driver of MSE tendency over the initiation region. This is similar to the findings of Zhao et al. (2013). $-\left\langle v \frac{\partial \overline{h}}{\partial y} \right\rangle$ acts as an important sink of MSE from day -5 to day 5, though no single component of this term is the cause of this sink.

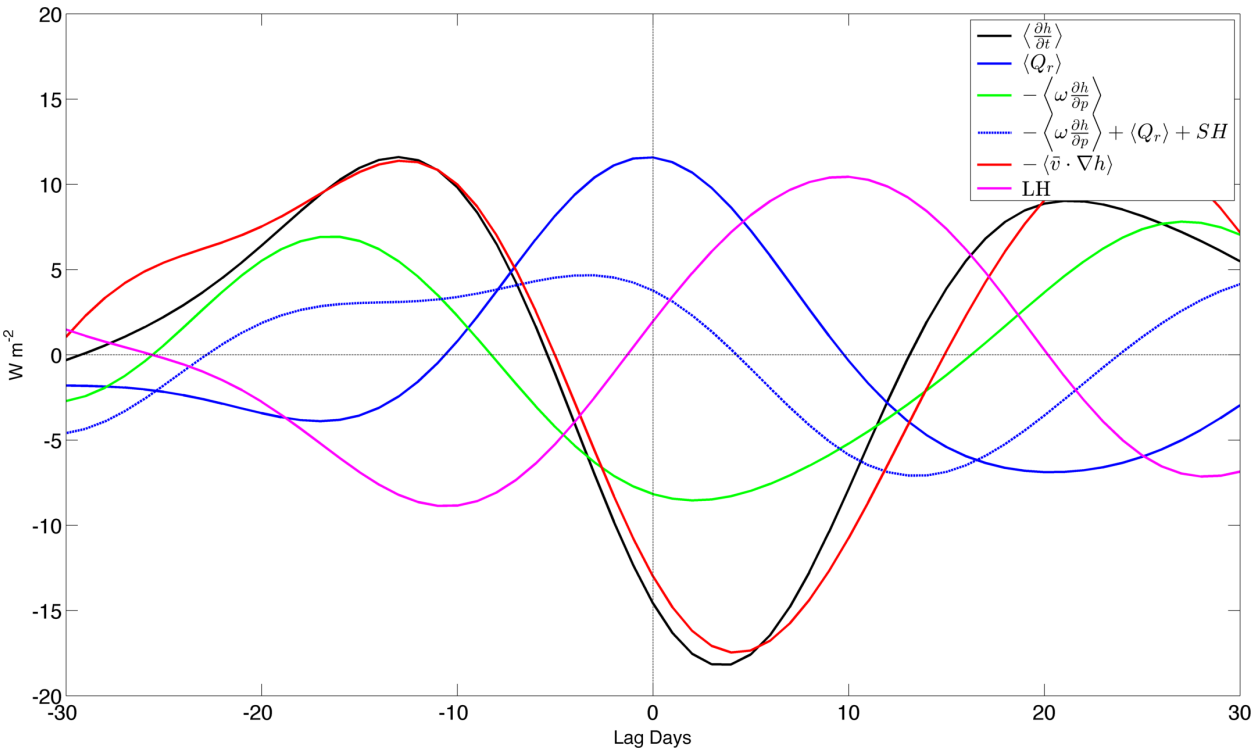

FIG. 3.49. Vertically integrated anomalous MSE budget terms from equation 1.15, from days -30 to 30 for the initiation budget. Budget terms were averaged over the initiation domain (4.5°N-4.5°S, 49.5°E-60°E).

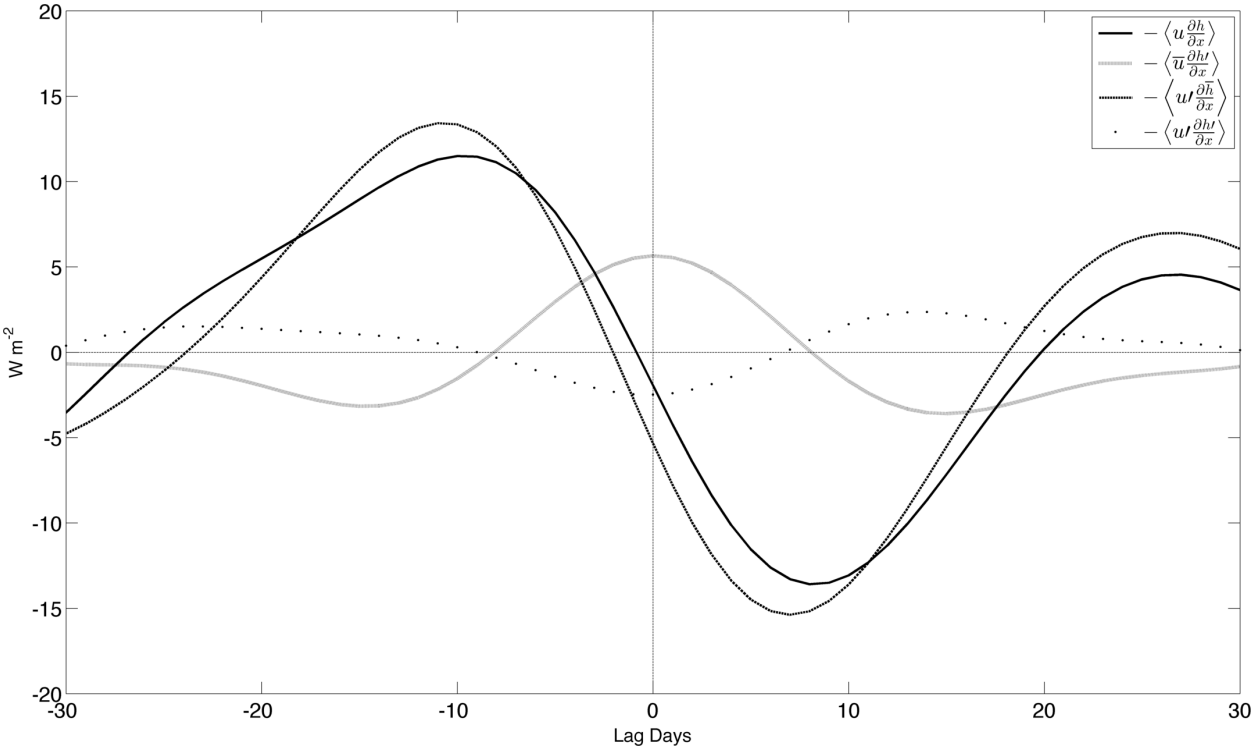

FIG. 3.50. As in Figure 3.49, except for the partitioning of the anomalous zonal advection term.

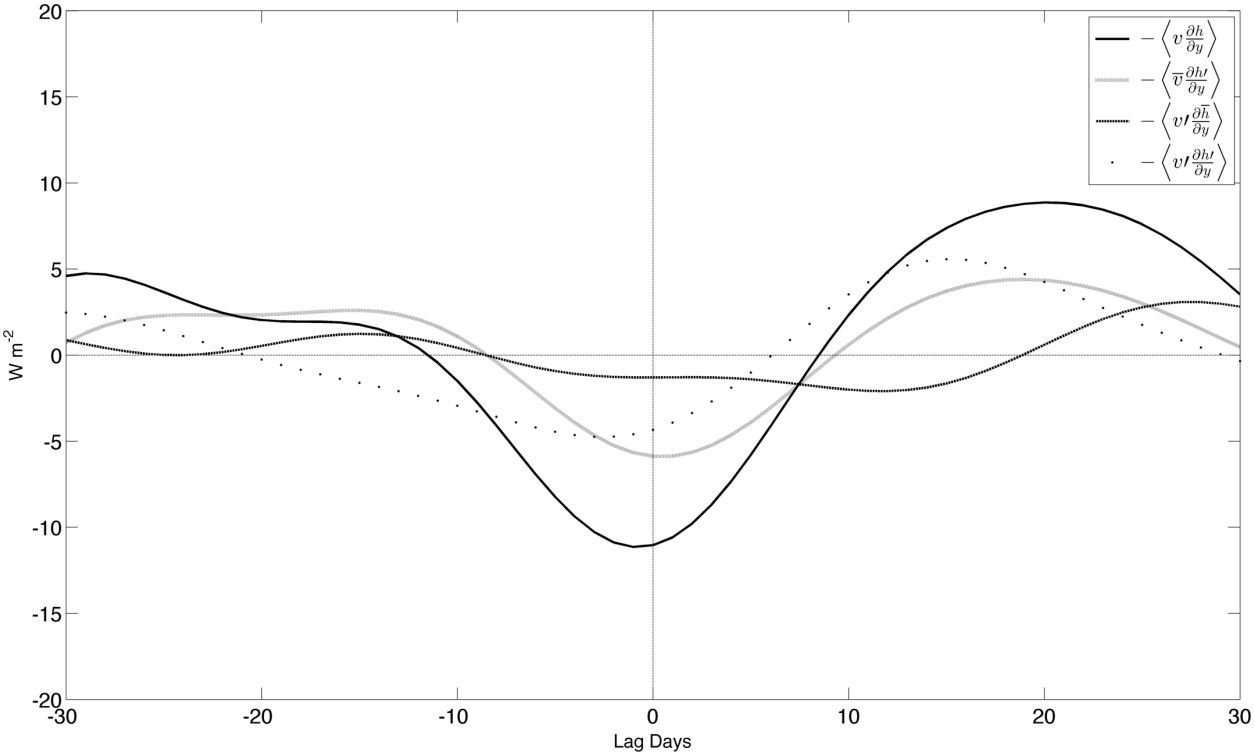

FIG. 3.51. As in Figure 3.49, except for the partitioning of the anomalous meridional advection term.

Figure 3.52 shows composites of the most influential terms in the MSE budget at day -10. This is the period during which the rapid building and eastward extension of a tongue of positive $q_{850,500}$ anomalies across the equatorial Indian Ocean occurs, as identified in figure 3.47. Coincident with this narrow tongue of positive $q_{850,500}$ anomalies is a region where anomalous vertical moisture advection appears to exceed anomalous precipitation, resulting in a net moistening. Easterly U850 anomalies originating from the region of suppressed convection span the Indian Ocean, and are associated with negative LH anomalies between 10°N and 10°S. The easterly U850 anomalies are also associated with anomalously positive horizontal advection of MSE. The dominant contribution of zonal advection to horizontal advection in the equatorial region is evident, and is primarily the result of $-\left\langle u' \frac{\partial \bar{h}}{\partial x} \right\rangle$ (not shown). This process is acting to moisten the regions eastward of the initiation region all the way to the maritime continent well before enhanced convection has fully developed over the initiation region.

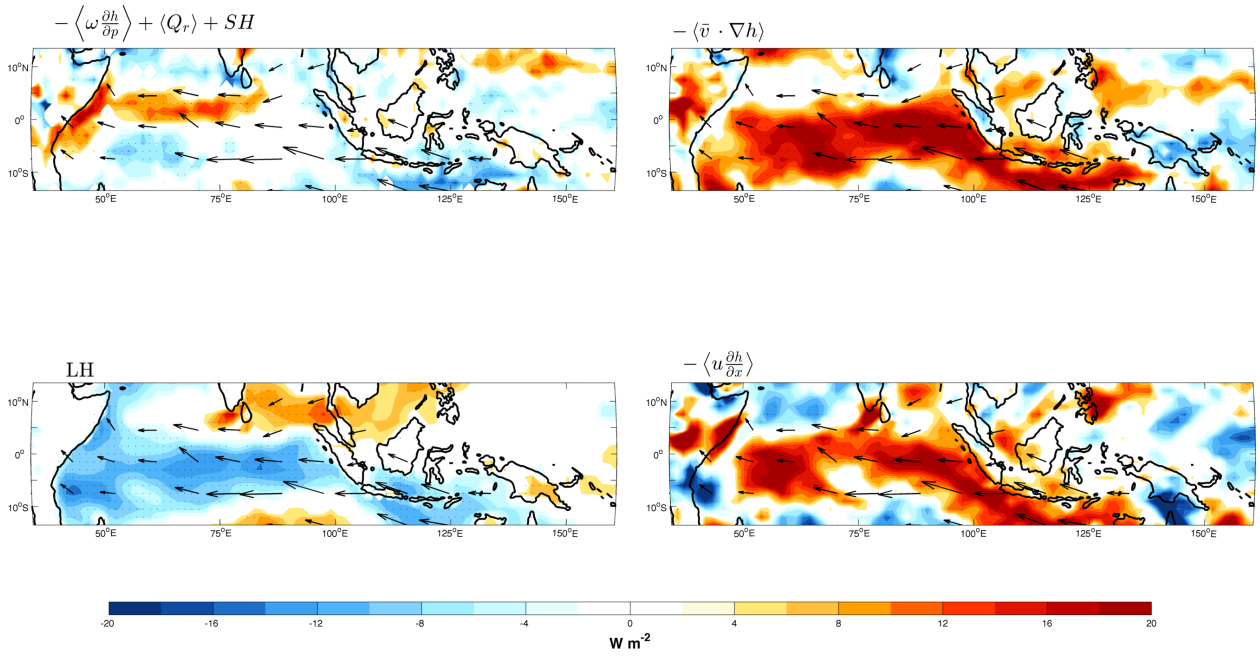

FIG. 3.52. Select vertically integrated anomalous MSE budget terms from equation 1.15 (color contours) and 850 hPa horizontal wind anomalies (vectors) at days -10 for the initiation budget. Stippling indicates anomalies significant at the 95% level. Wind vectors are statistically significant at the 95% level. A reference wind vector is provided in the lower right corner of the lower right panel.

A similar budget analysis was performed on events identified to be "primary", drawn as a subset of the events included in the analysis above. To qualify as primary events, a period of at least 7 consecutive days with index amplitude below 1 must have occurred in the 2 weeks prior to "Day 0". Only 13 events met this qualification. The resultant budget was remarkably similar to the initiation budget presented above, but with substantially lower statistical significance. Hence, these results have not been included in the present work.

CHAPTER 4

Discussion

A set of objective diagnostics, obtained as an extension of CEOF analysis, have been introduced. These diagnostics were used to objectively compare the anomalous MSE budget of geographically disparate locations in the context of a composite MJO lifecycle. This highlighted prominent geographical variability in the processes affecting the MSE budget of the MJO, and demonstrated that these processes act in a fairly consistent fashion throughout the Indian Ocean. This motivated a composite MSE budget of the MJO in the Indian Ocean, which suggests that net affects of anomalous vertical moisture advection and anomalous precipitation on column integrated moisture content largely balance, potentially acting to maintain convective anomalies throughout the MJO lifecycle. Anomalous horizontal advection, which is incompletely opposed by anomalous LH, appears to play a important role in driving MSE tendency in the Indian Ocean. Convective initiation in the western Indian Ocean is preceded by anomalous moistening, driven in large part by anomalous zonal advection resulting from anomalous easterlies acting on the mean state moisture gradient. Anomalous vertical moisture advection exceeding anomalous precipitation may play a role in moistening during this period as well. Each one of these findings will now be discussed in further detail below.

4.1. Geographical Variability

The geographical variability of the processes that control the MSE budget of the MJO was assessed using the new diagnostics. Prominent geographical variability is primarily related to changes in the mean state low level winds that occur near the dateline and poleward of

$\sim 7.5°$, changes in the mean state zonal moisture gradient that occur east of the Maritime Continent and poleward of $\sim 7.5°$, and changes in the phase relation between low level wind anomalies and MSE anomalies that occur most dramatically east of the Maritime Continent. These changes cause LH $\left(-\left\langle u'\frac{\partial \bar{h}}{\partial x}\right\rangle\right)$ to transition from being out of phase (in phase) with $\left\langle \frac{\partial h}{\partial t}\right\rangle$ in the Indian Ocean and Maritime Continent region to being out of phase (in phase) with MSE anomalies near the dateline. This fundamentally changes how the actions of various processes combine to help grow, maintain and dissipate MSE anomalies throughout the lifecycle of the MJO.

The modulation of MSE over a broad region of the tropics ($15°N - 15°S$) appears to be driven by a combination of processes that act to induce anomalous moistening or drying in characteristically different ways. For example, LH and $-\left\langle u'\frac{\partial \bar{h}}{\partial x}\right\rangle$) are in excess of $25\,\mathrm{W\,m^{-2}}$ equatorward of $5°$, yet are typically less than $10\,\mathrm{W\,m^{-2}}$ when averaged from $15°N - 15°S$. The dramatic reduction of the influence of these terms when considered over the broader tropics occurs because the mean state conditions that determine the manner in which they act exist only over a narrow equatorial band. The limited regions where these terms have large amplitude and dominate the MSE tendency are co-located with the regions of largest wintertime intraseasonal OLR variability identified by Sobel et al. (2010). In contrast, the affects of the horizontal advection terms related to the enhancement or suppression of synoptic scale eddy mixing are almost negligible over these limited regions, yet have substantial roles when considered in the $15°N - 15°S$ average. This suggests that LH and $-\left\langle u'\frac{\partial \bar{h}}{\partial x}\right\rangle$ provide substantial anomalous sources/sinks of MSE that support the growth of MSE anomalies in limited regions of the deep tropics, while the modulation of synoptic scale eddy activity acts to condition the tropics on a broader scale, extending the enhancement/suppression of

convective activity to the periphery of the tropics. $-\left\langle v'\frac{\partial \bar{h}}{\partial y}\right\rangle$ also appears to play an important role in strengthening the amplitude of MSE anomalies near the periphery of the tropics, although this process acts in phase with MSE anomalies, distinguishing it from the affects of horizontal eddy transports.

The distinct ways which these processes act to modulate MSE reflect differences in the physical nature of the processes themselves. The manner in which LH, $-\left\langle v'\frac{\partial \bar{h}}{\partial y}\right\rangle$ and $-\left\langle u'\frac{\partial \bar{h}}{\partial x}\right\rangle$ effect MSE anomalies is largely determined by background state in which a given MJO event occurs, namely the background state low level winds and zonal moisture gradient. The tendency for certain background states to occur more frequently in distinct geographical regions is reflected in the time mean of these fields. This tendency leads these processes to act as consistent sources/sinks of MSE anomalies in certain geographical locations. In contrast, the effects of modulating synoptic scale eddy mixing is dependent on the timing, location, strength and number of synoptic scale eddies occurring during a given MJO event. These factors likely display a great deal of variability from one MJO event to another. When considered in a composite sense, the consistent modulation of eddy activity over numerous MJO events depicts a pervasive broad scale modulation of MSE with little geographical preference, reflecting the more diffusive nature of the process.

4.2. The MJO in the Indian Ocean

The combination of processes that drive the MSE budget of the MJO appears remarkably consistent across the Indian Ocean (and to a lesser extent the Maritime Continent region), allowing the lifecycle of the MJO in this region to be generalized and represented by a single MSE budget. This budget indicates that $\sim 90\%$ of these MSE anomalies are in the form of $\langle q \rangle$ anomalies, which has important implications for the large degree of cancelation

between anomalous $-\left\langle \omega \frac{\partial h}{\partial p} \right\rangle$, anomalous $\langle Q_r \rangle$ and anomalous SH throughout the MJO lifecycle. The small contribution of temperature anomalies to MSE anomalies indicates that there is an approximate balance between anomalous diabatic heating(cooling) and anomalous adiabatic cooling(warming), and provides justification for using equation 1.19 to relate MSE budget terms to moisture budget terms. This relationship suggests that anomalous vertical moisture advection approximately balances the affects of anomalous precipitation on column integrated moisture content throughout the MJO lifecycle, helping maintain convective anomalies. An initial analysis of the relationship of vertical moisture advection and anomalous precipitation in the central Indian Ocean suggests that anomalous vertical moisture advection slightly exceeds anomalous precipitation, potentially helping destabilize MJO. The moisture budget results of Kiranmayi and Maloney (2011) support these findings.

Anomalous vertical moisture advection can result from a change in mass convergence and/or a change in the moisture content of the mass converged. Anomalous vertical moisture advection is likely a consequence of changes in both the vertical profile of diabatic heating associated with latent heat release, and anomalous adiabatic decent associated with anomalous longwave cooling to space. The net affect of these two changes must lead to a enhancement(reduction) in vertical moisture advection during periods of enhanced(suppressed) precipitation, to the extent they balance or exceed moisture loss(gain) from the anomalous precipitation.

The large degree of cancelation between anomalous $-\left\langle \omega \frac{\partial h}{\partial p} \right\rangle$, anomalous $\langle Q_r \rangle$ and anomalous SH throughout the MJO lifecycle also suggests that other process may play an important role in the zonally asymmetric growth and dissipation of moisture anomalies in the Indian Ocean. It is ultimately this asymmetrical growth and dissipation of moisture anomalies that

results in the eastward propagation of the MJO. This study finds that anomalous horizontal advection is responsible for the growth(decrease) of moisture anomalies during the transition from suppressed(enhanced) convection to enhanced(suppressed) convection, and that smaller amplitude LH anomalies continually act in opposition to anomalous horizontal advection. Anomalous horizontal advection is primarily the result of $-\left\langle u' \frac{\partial \overline{h}}{\partial x} \right\rangle$) equatorward of 5° and $-\left\langle v \frac{\partial h}{\partial y} \right\rangle$ over the broader region of $15°N - 15°S$. Remember that the manner in which these terms act is determined by mean state zonal moisture gradient and the mean state zonal wind shear. These findings suggest that the westerly mean state winds themselves may not be crucial to the MJO, although they likely have a large influence on its propagation speed through their impacts on LH anomalies. The tendency for MJO to preferentially occur in regions of mean state westerly winds appears to be a result of the colocation of westerly mean state winds with the largest mean state moisture gradient. This colocation results from the overturning Walker circulation, and so is intimately linked to climatological convection.

Convective initiation over the western Indian Ocean appears to be preceded by a similar combination of processes. For $\sim$ 2 weeks prior to the onset of deep convection, a narrow tongue of enhanced free tropospheric moisture develops in tandem with substantial anomalous positive horizontal MSE advection, driven primarily by $-\left\langle u' \frac{\partial \overline{h}}{\partial x} \right\rangle$). This may be one reason why successive events, which are often preceded by suppressed convection and easterly U850 anomalies across the Indian Ocean, appear to occur more frequently than primary events (Matthews 2008; Straub 2013). Anomalous vertical moisture advection appears to exceed anomalous moisture loss from precipitation in the initiation region during this period of deepening convection, and may play an important role in destabilization.

4.3. A simplified conceptual model for the MJO

The true physical nature of the processes discussed above deserves further clarification. As demonstrated above, the MJO can be examined effectively by considering anomalies in the processes that control MSE. While such a perspective aides in the identification of processes important to the MJO, it can also be a source of misinterpretation of the physical processes at work. The mean action of each process must be considered to fully understand how a combination of changes in such processes can conspire to produce environmental conditions that support the MJO. The following simplified conceptual model, many aspects of which originate from the model proposed by Sobel and Maloney (2013), aims to distill the findings of this study and put them in the context of the mean state of processes at work in the tropics.

Figure 4.1 shows the intraseasonal anomalies presented in 3.44 added to their mean values over the respective time period. Certain processes, such as LH(radiation), always act as a source(sink) of MSE. Therefore anomalies in such processes must be viewed as a reduction or enhancement of the MSE source(sink). Although the mean state of individual processes are very large, the net affect of their combined mean states is zero. Therefore, anomalies in any of these processes, although small relative to their mean state, have large consequences.

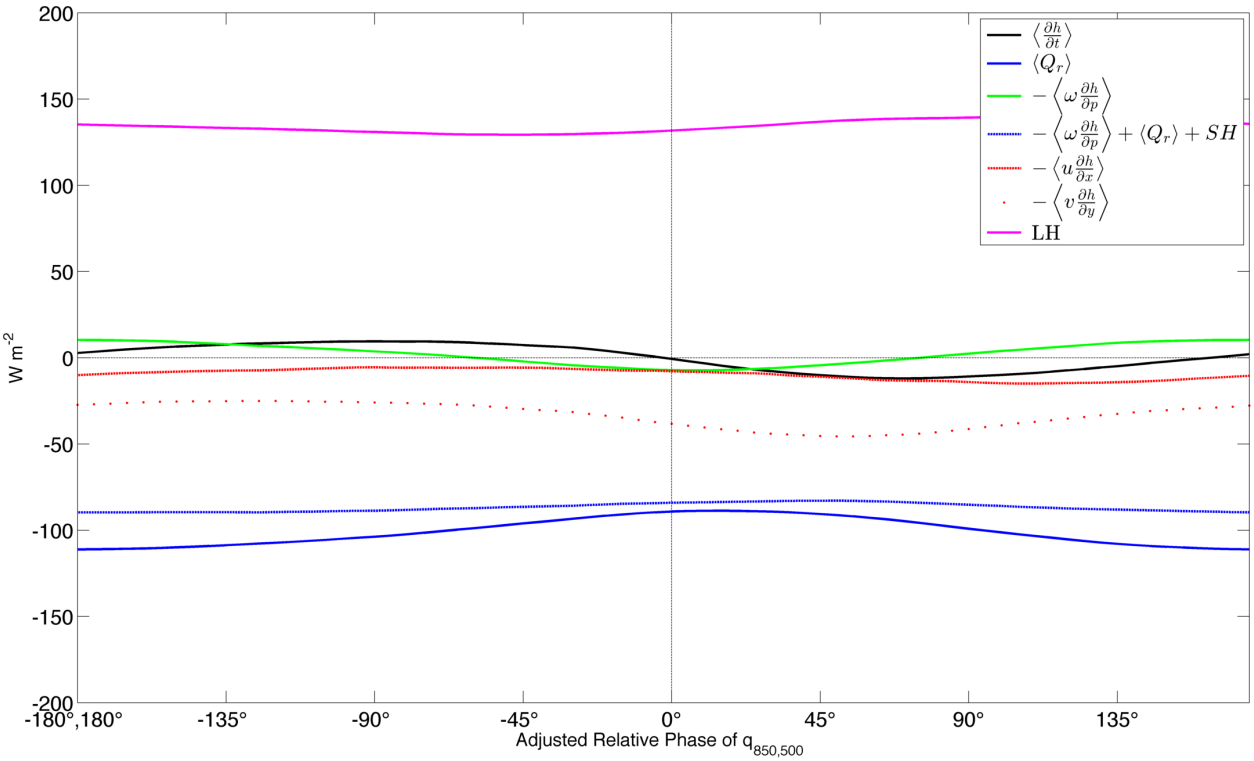

FIG. 4.1. As in Figure 3.44, except the time mean of each term over the respective area has been added to the anomalies presented in Figure 3.44.

The tropics contain both regions of mean moisture convergence and mean moisture divergence. The distribution of these regions is largely controlled by the features of the general circulation, driving large mean moisture convergence in the deep tropics and reduced mean moisture convergence or mean moisture divergence at their periphery. In both of these regions, the action of mean precipitation (considered over a sufficiently long period) is to remove moisture provided by the net affects of LH and mean moisture convergence/divergence. Note the near constant value of $-\left\langle \omega \frac{\partial h}{\partial p} \right\rangle + \langle Q_r \rangle + SH$, which approximately quantifies the net affects of vertical moisture advection and precipitation on $\langle h \rangle$ and $\langle Lq \rangle$. This shows that throughout the lifecycle of the MJO, the net affects of vertical moisture advection and precipitation result in a near constant loss of 90 W m^{-2}. This suggests that other processes play an important role in the modulation of $\left\langle \frac{\partial h}{\partial t} \right\rangle$ and the evolution of convective anomalies.

The asymmetric dynamical response to equatorial heating is such that a region of enhanced convection occurring in the context of the mean state of the eastern hemisphere induces preferential moistening to the east and drying to the west, in both the deep tropics and at their periphery. Regions of enhanced convection are associated anomalous vertical moisture advection that balances or slightly exceeds anomalous moisture loss from precipitation, helping to maintain instability in this region. The physical mechanism that links these processes remains unclear. Anomalous easterlies extending to the east of this region result in a reduction in moisture loss due to horizontal advection. LH is reduced in regions of westerly mean state winds, but to a lesser extent than the reduction in horizontal drying, allowing for moisture supplied by LH and vertical moisture advection to support the enhancement of convection. Anomalous westerlies extending to the west of this region result in an enhancement in moisture loss due to horizontal advection. LH is enhanced in regions of westerly mean state winds, but to a lesser extent than the enhancement in horizontal drying, resulting in a reduction in the ability of LH and vertical moisture advection to support convection. Ultimately it is this asymmetrical moistening and drying that leads to the propagation of the region of enhanced convection. While certain processes affected by the asymmetric dynamical response do not display a high degree of geographical dependence (i.e. terms related to modulation of synoptic eddy activity), the geographical dependence of other processes (i.e. $-\left\langle u' \frac{\partial \bar{h}}{\partial x} \right\rangle$) and LH) result in a stronger asymmetrical response in the eastern hemisphere.

In this simplified conceptual model, geographical changes in the MJO result from changes in the mean state winds and the mean state moisture gradient, as well as the climatological convection that they modulate. The meridional gradient of mean state zonal winds appears

to be a crucial part of this arrangement of mean state winds, as it may affect the extent to which the MJO modulates synoptic eddy activity. This model is not meant to be representative of the observed MJO, or the processes that determine the evolution of the MSE environment during individual MJO events. Investigation of the non-filtered terms of the MSE budget (not shown) clearly demonstrates the large role variability across a range of spatial and temporal scales plays in the evolution of MSE. Mean fields are only representative of a tendency for certain conditions to exist, not a perpetual background state in which the MJO occurs. Higher frequency variability that does not influence the MSE environment of the MJO in a consistent way still has dramatic affects on this environment during individual events. The fact that many of the important processes highlighted in this model are related to long term mean features allows their affects, acting in a relatively consistent manner over the course of decades, to emerge from this noise in composite analysis. This model simply highlights the roles of the processes that influence the MSE environment of the MJO in relatively consistent manner, and how their combined effects can explain features of a composite MJO.

The results of this study support the idea of the MJO as a moisture mode. The large contribution ($\sim 90\%$) of moisture anomalies to total MSE anomalies suggests that a WTG balance holds to first order. There is a large and direct covariance between column integrated moisture anomalies and anomalies in convection. The processes that control the evolution of the moisture field, and thereby the evolution of convective anomalies, are largely determined by the large scale dynamical response to these convective anomalies in the context of mean state winds and the mean state moisture gradient.

4.4. Summary

The primary findings of this study are that

(1) MSE anomalies associated with the MJO are mostly ($\sim 90\%$) the result of moisture anomalies.

(2) Prominent geographical variability in the MSE budget of the MJO occurs near the dateline, and is associated with changes in the mean state moisture gradient and mean state lower tropospheric winds.

(3) Anomalous horizontal MSE advection, incompletely opposed by anomalous LH fluxes, is primarily responsible for propagating MSE anomalies associated with the MJO eastward in the Indian Ocean.

(4) In the deep tropics, anomalous horizontal MSE advection is primarily the result of zonal wind anomalies occurring within a zonal mean state moisture gradient. Over the broader tropics, anomalous horizontal MSE advection is primarily the result of the modulation of synoptic scale eddy mixing, as well as meridional wind anomalies occurring within a meridional mean state moisture gradient.

(5) Anomalous vertical moisture advection appears to slightly exceed anomalous precipitation throughout the MJO lifecycle, helping maintain moisture anomalies against dissipation by anomalous precipitation.

(6) The application of new objective diagnostics introduced in this study has provided unique and useful insight to the MJO.

4.5. Implications for Future Work

These findings suggest that if modeling studies wish to create an accurate representation of the processes that affecting the MSE budget of the MJO, certain basic state conditions

must be realistic. Foremost among these are the mean state moisture gradient, the strength and spatial distribution of mean state winds, and realistic meridional wind shear. While MJO-like variability can, and has been created in modeling studies where the basic state does not match that presented in this study, the combination of processes that grow, maintain and propagate MSE anomalies in such a model are likely to deviate from those observed in the real world. Such deviations should be considered if the model is to be used to assess problems such as changes the MJO may undergo during climate change.

A central finding of this study is the relationship between anomalous precipitin and anomalous vertical moisture advection. In this study, precipitation was estimated from a moisture budget calculated from reanalysis data, and subjected to bandpass filtering. The inclusion of a budget residual, and the deleterious affects of bandpass filtering on a noisy field such as precipitation must be considered when analyzing the scatterplot results presented in this study. Nonetheless, similar conclusions derived from an analysis of the MSE budget, as well as the findings of Kiranmayi and Maloney (2011) suggest that this relationship may be present, and worthy of further investigation. No physical mechanism to explain the observed relationship between anomalous vertical moisture advection and anomalous precipitation has been proposed in this study, and should be a focus of future research.

While reanalysis products have many desirable features that make studies such as this one feasible, many questions are raised in the use of such a product. How well is the parametrized convection in ERAi able to represent any convective-radiative feedback that may exist? What physical processes are poorly represented, and lead to the residual consistently seen in other studies? To what extent are bandpass filtered terms misleading, homogenizing certain

asymmetrical features of the MJO such as the westerly wind burst? These are questions that must be addressed in future observational and modeling studies.

REFERENCES

Andersen, J. A. and Z. Kuang, 2012: Moist static energy budget of mjo-like disturbances in the atmosphere of a zonally symmetric aquaplanet. *Journal of Climate*, **25 (8)**, 2782–2804.

Back, L. and C. Bretherton, 2006: Geographic variability in the export of moist static energy and vertical motion profiles in the tropical pacific. *Geophysical research letters*, **33 (17)**.

Benedict, J. J. and D. A. Randall, 2007: Observed characteristics of the mjo relative to maximum rainfall. *Journal of the atmospheric sciences*, **64 (7)**, 2332–2354.

Bladé, I. and D. L. Hartmann, 1993: Tropical intraseasonal oscillations in a simple nonlinear model. *Journal of the atmospheric sciences*, **50 (17)**, 2922–2939.

Bretherton, C. S., P. N. Blossey, and M. Khairoutdinov, 2005: An energy-balance analysis of deep convective self-aggregation above uniform sst. *Journal of the atmospheric sciences*, **62 (12)**, 4273–4292.

Bretherton, C. S., M. E. Peters, and L. E. Back, 2004: Relationships between water vapor path and precipitation over the tropical oceans. *Journal of climate*, **17 (7)**, 1517–1528.

Cai, Q., G. J. Zhang, and T. Zhou, 2013: Impacts of shallow convection on mjo simulation: A moist static energy and moisture budget analysis. *Journal of Climate*, **26 (8)**, 2417–2431.

Carvalho, L. M., C. Jones, and T. Ambrizzi, 2005: Opposite phases of the antarctic oscillation and relationships with intraseasonal to interannual activity in the tropics during the austral summer. *Journal of climate*, **18 (5)**, 702–718.

Charney, J. G., 1963: A note on large-scale motions in the tropics. *Journal of the Atmospheric Sciences*, **20 (6)**, 607–609.

Charney, J. G. and A. Eliassen, 1964: On the growth of the hurricane depression. *Journal of the Atmospheric Sciences*, **21 (1)**, 68–75.

Cooley, J. W. and J. W. Tukey, 1965: An algorithm for the machine calculation of complex fourier series. *Mathematics of computation*, **19 (90)**, 297–301.

Dee, D., et al., 2011: The era-interim reanalysis: Configuration and performance of the data assimilation system. *Quarterly Journal of the Royal Meteorological Society*, **137 (656)**, 553–597.

Ebdon, R., 1960: Notes on the wind flow at 50 mb in tropical and sub-tropical regions in january 1957 and january 1958. *Quarterly Journal of the Royal Meteorological Society*, **86 (370)**, 540–542.

Emanuel, K. A., 1987: An air-sea interaction model of intraseasonal oscillations in the tropics. *Journal of the atmospheric sciences*, **44 (16)**, 2324–2340.

Gill, A., 1980: Some simple solutions for heat-induced tropical circulation. *Quarterly Journal of the Royal Meteorological Society*, **106 (449)**, 447–462.

Haertel, P. T., G. N. Kiladis, A. Denno, and T. M. Rickenbach, 2008: Vertical-mode decompositions of 2-day waves and the madden-julian oscillation. *Journal of the Atmospheric Sciences*, **65 (3)**, 813–833.

Hall, J. D., A. J. Matthews, and D. J. Karoly, 2001: The modulation of tropical cyclone activity in the australian region by the madden-julian oscillation. *Monthly weather review*, **129 (12)**, 2970–2982.

Heckley, W. and A. Gill, 1984: Some simple analytical solutions to the problem of forced equatorial long waves. *Quarterly Journal of the Royal Meteorological Society*, **110 (463)**, 203–217.

Hendon, H. H. and M. L. Salby, 1994: The life cycle of the madden-julian oscillation. *Journal of the Atmospheric Sciences*, **51 (15)**, 2225–2237.

Holloway, C. E. and J. D. Neelin, 2009: Moisture vertical structure, column water vapor, and tropical deep convection. *Journal of the Atmospheric Sciences*, **66 (6)**, 1665–1683.

Holton, J., 2004: *Introduction to dynamic meteorology, forth edition, Department of Atmospheric Science University of Washington*. Elsevier Academic Press.

Hoskins, B. J. and G.-Y. Yang, 2000: The equatorial response to higher-latitude forcing. *Journal of the atmospheric sciences*, **57 (9)**, 1197–1213.

Hu, Q. and D. A. Randall, 1994: Low-frequency oscillations in radiative-convective systems. *Journal of the atmospheric sciences*, **51 (8)**, 1089–1099.

Jiang, X., et al., 2011: Vertical diabatic heating structure of the mjo: Intercomparison between recent reanalyses and trmm estimates. *Monthly Weather Review*, **139 (10)**, 3208–3223.

Jin, F. and B. J. Hoskins, 1995: The direct response to tropical heating in a baroclinic atmosphere. *Journal of the atmospheric sciences*, **52 (3)**, 307–319.

Jones, C., D. E. Waliser, K. Lau, and W. Stern, 2004: The madden-julian oscillation and its impact on northern hemisphere weather predictability. *Monthly weather review*, **132 (6)**, 1462–1471.

Kemball-Cook, S. R. and B. C. Weare, 2001: The onset of convection in the madden-julian oscillation. *Journal of climate*, **14 (5)**, 780–793.

Kiladis, G. N., K. H. Straub, and P. T. Haertel, 2005: Zonal and vertical structure of the madden-julian oscillation. *Journal of the atmospheric sciences*, **62 (8)**, 2790–2809.

Kiladis, G. N. and K. M. Weickmann, 1992: Circulation anomalies associated with tropical convection during northern winter. *Monthly weather review*, **120 (9)**, 1900–1923.

Kiladis, G. N., M. C. Wheeler, P. T. Haertel, K. H. Straub, and P. E. Roundy, 2009: Convectively coupled equatorial waves. *Reviews of Geophysics*, **47 (2)**.

Kim, D., J.-S. Kug, and A. H. Sobel, 2013a: Propagating vs. non-propagating madden-julian oscillation events. *Journal of Climate*, **(2013)**.

Kim, D., M.-I. Lee, D. Kim, S. D. Schubert, D. E. Waliser, and B. Tian, 2013b: Representation of tropical subseasonal variability of precipitation in global reanalyses. *Climate Dynamics*, 1–18.

Kiranmayi, L. and E. D. Maloney, 2011: Intraseasonal moist static energy budget in reanalysis data. *Journal of Geophysical Research: Atmospheres (1984–2012)*, **116 (D21)**.

Lau, W. K. and D. E. Waliser, 2012: *Intraseasonal variability in the atmosphere-ocean climate system*. Springer.

Lau, W. K., D. E. Waliser, and B. Goswami, 2012a: South asian monsoon. *Intraseasonal variability in the atmosphere-ocean climate system*, Springer, 21–72.

Lau, W. K., D. E. Waliser, and P. E. Roundy, 2012b: Tropical–extratropical interactions. *Intraseasonal Variability in the Atmosphere-Ocean Climate System*, Springer, 497–512.

Liebmann, B. and C. Smith, 1996: Description of a complete (interpolated) outgoing longwave radiation dataset. *Bulletin of the American Meteorological Society*, **77**, 1275–1277.

Lin, H., G. Brunet, and J. Derome, 2008: Forecast skill of the madden-julian oscillation in two canadian atmospheric models. *Monthly Weather Review*, **136 (11)**, 4130–4149.

Lin, X. and R. H. Johnson, 1996a: Heating, moistening, and rainfall over the western pacific warm pool during toga coare. *Journal of the atmospheric sciences*, **53 (22)**, 3367–3383.

Lin, X. and R. H. Johnson, 1996b: Kinematic and thermodynamic characteristics of the flow over the western pacific warm pool during toga coare. *Journal of the atmospheric sciences*, **53 (5)**, 695–715.

Lindzen, R. S., 1974: Wave-cisk in the tropics. *Journal of the Atmospheric Sciences*, **31 (1)**, 156–179.

Lindzen, R. S. and T. Matsuno, 1968: On the nature of large scale wave disturbances in the equatorial lower stratosphere. *J. Meteor. Soc. Japan*, **46**, 215–221.

Madden, R. A. and P. R. Julian, 1971: Detection of a 40-50 day oscillation in the zonal wind in the tropical pacific. *Journal of the Atmospheric Sciences*, **28 (5)**, 702–708.

Madden, R. A. and P. R. Julian, 1972: Description of global-scale circulation cells in the tropics with a 40-50 day period. *Journal of the Atmospheric Sciences*, **29 (6)**, 1109–1123.

Maloney, E. D., 2009: The moist static energy budget of a composite tropical intraseasonal oscillation in a climate model. *Journal of Climate*, **22 (3)**, 711–729.

Maloney, E. D. and M. J. Dickinson, 2003: The intraseasonal oscillation and the energetics of summertime tropical western north pacific synoptic-scale disturbances. *Journal of the atmospheric sciences*, **60 (17)**, 2153–2168.

Maloney, E. D. and D. L. Hartmann, 1998: Frictional moisture convergence in a composite life cycle of the madden-julian oscillation. *Journal of climate*, **11 (9)**, 2387–2403.

Maloney, E. D. and D. L. Hartmann, 2000a: Modulation of eastern north pacific hurricanes by the madden-julian oscillation. *Journal of climate*, **13 (9)**, 1451–1460.

Maloney, E. D. and D. L. Hartmann, 2000b: Modulation of hurricane activity in the gulf of mexico by the madden-julian oscillation. *Science*, **287 (5460)**, 2002–2004.

Maloney, E. D. and A. H. Sobel, 2007: Idealized hot spot experiments with a general circulation model. *Journal of climate*, **20 (5)**, 908–925.

Maloney, E. D., A. H. Sobel, and W. M. Hannah, 2010: Intraseasonal variability in an aquaplanet general circulation model. *Journal of Advances in Modeling Earth Systems*, **2 (2)**.

Mapes, B., S. Tulich, J. Lin, and P. Zuidema, 2006: The mesoscale convection life cycle: Building block or prototype for large-scale tropical waves? *Dynamics of atmospheres and oceans*, **42 (1)**, 3–29.

Mapes, B. E. and J. T. Bacmeister, 2012: Diagnosis of tropical biases and the mjo from patterns in the merra analysis tendency fields. *Journal of Climate*, **25 (18)**, 6202–6214.

Matsuno, T., 1966: Quasi-geostrophic motions in the equatorial area. *J. Meteor. Soc. Japan*, **44 (1)**, 25–43.

Matthews, A. J., 2000: Propagation mechanisms for the madden-julian oscillation. *Quarterly Journal of the Royal Meteorological Society*, **126 (569)**, 2637–2651.

Matthews, A. J., 2008: Primary and successive events in the madden–julian oscillation. *Quarterly Journal of the Royal Meteorological Society*, **134 (631)**, 439–453.

Matthews, A. J. and G. N. Kiladis, 1999: The tropical-extratropical interaction between high-frequency transients and the madden-julian oscillation. *Monthly weather review*, **127 (5)**, 661–677.

McPhaden, M. J., 1999: Genesis and evolution of the 1997-98 el niño. *Science*, **283 (5404)**, 950–954.

Moore, R. W., O. Martius, and T. Spengler, 2010: The modulation of the subtropical and extratropical atmosphere in the pacific basin in response to the madden-julian oscillation. *Monthly Weather Review*, **138 (7)**, 2761–2779.

Moskowitz, B. M. and C. S. Bretherton, 2000: An analysis of frictional feedback on a moist equatorial kelvin mode. *Journal of the atmospheric sciences*, **57 (13)**, 2188–2206.

Murakami, T., 1980: Empirical orthogonal function analysis of satellite-observed outgoing longwave radiation during summer. *Monthly Weather Review*, **108 (2)**, 205–222.

Nakazawa, T., 1988: Tropical super clusters within intraseasonal variations over the western pacific. *Journal of the Meteorological Society of Japan*, **66 (6)**, 823–839.

Neelin, J. D. and I. M. Held, 1987: Modeling tropical convergence based on the moist static energy budget. *Monthly Weather Review*, **115 (1)**, 3–12.

Neelin, J. D., I. M. Held, and K. H. Cook, 1987: Evaporation-wind feedback and low-frequency variability in the tropical atmosphere. *Journal of the Atmospheric Sciences*, **44 (16)**, 2341–2348.

Neelin, J. D., O. Peters, and K. Hales, 2009: The transition to strong convection. *Journal of the Atmospheric Sciences*, **66 (8)**, 2367–2384.

North, G. R., T. L. Bell, R. F. Cahalan, and F. J. Moeng, 1982: Sampling errors in the estimation of empirical orthogonal functions. *Monthly Weather Review*, **110 (7)**, 699–706.

Olivier, J. and M. M. Norberg, 2010: Positively skewed data: Revisiting the box-cox power transformation. *International Journal of Psychological Research*, **3 (1)**, 68–77.

Peters, O. and J. D. Neelin, 2006: Critical phenomena in atmospheric precipitation. *Nature Physics*, **2 (6)**, 393–396.

Raymond, D. J., 1995: Regulation of moist convection over the west pacific warm pool. *Journal of the atmospheric sciences*, **52 (22)**, 3945–3959.

Raymond, D. J., 2001: A new model of the madden-julian oscillation. *Journal of the atmospheric sciences*, **58 (18)**, 2807–2819.

Raymond, D. J. and Ž. Fuchs, 2009: Moisture modes and the madden-julian oscillation. *Journal of Climate*, **22 (11)**, 3031–3046.

Raymond, D. J., S. L. Sessions, A. H. Sobel, and Ž. Fuchs, 2009: The mechanics of gross moist stability. *Journal of Advances in Modeling Earth Systems*, **1 (8)**.

Roundy, P. E., K. MacRitchie, J. Asuma, and T. Melino, 2010: Modulation of the global atmospheric circulation by combined activity in the madden-julian oscillation and the el niño-southern oscillation during boreal winter. *Journal of Climate*, **23 (15)**, 4045–4059.

Roundy, P. E., C. J. Schreck III, and M. A. Janiga, 2009: Contributions of convectively coupled equatorial rossby waves and kelvin waves to the real-time multivariate mjo indices. *Monthly Weather Review*, **137 (1)**, 469–478.

Rui, H. and B. Wang, 1990: Development characteristics and dynamic structure of tropical intraseasonal convection anomalies. *Journal of the Atmospheric Sciences*, **47 (3)**, 357–379.

Sahany, S., J. D. Neelin, K. Hales, and R. B. Neale, 2012: Temperature-moisture dependence of the deep convective transition as a constraint on entrainment in climate models. *Journal of the Atmospheric Sciences*, **69 (4)**, 1340–1358.

Schumacher, C., M. H. Zhang, and P. E. Ciesielski, 2007: Heating structures of the trmm field campaigns. *Journal of the atmospheric sciences*, **64 (7)**, 2593–2610.

Slade, S. A. and E. D. Maloney, 2013: An intraseasonal prediction model of atlantic and east pacific tropical cyclone genesis. *Monthly Weather Review*, **141 (6)**, 1925–1942.

Sobel, A. and E. Maloney, 2012: An idealized semi-empirical framework for modeling the madden-julian oscillation. *Journal of the Atmospheric Sciences*, **69 (5)**, 1691–1705.

Sobel, A. and E. Maloney, 2013: Moisture modes and the eastward propagation of the mjo. *Journal of the Atmospheric Sciences*, **70 (1)**, 187–192.

Sobel, A. H., E. D. Maloney, G. Bellon, and D. M. Frierson, 2010: Surface fluxes and tropical intraseasonal variability: A reassessment. *Journal of Advances in Modeling Earth Systems*, **2 (1)**.

Sobel, A. H., J. Nilsson, and L. M. Polvani, 2001: The weak temperature gradient approximation and balanced tropical moisture waves*. *Journal of the atmospheric sciences*, **58 (23)**, 3650–3665.

Straub, K. H., 2013: Mjo initiation in the real-time multivariate mjo index. *Journal of Climate*, **26 (4)**, 1130–1151.

Takayabu, Y. N., T. Iguchi, M. Kachi, A. Shibata, and H. Kanzawa, 1999: Abrupt termination of the 1997–98 el niño in response to a madden–julian oscillation. *Nature*, **402 (6759)**, 279–282.

Tian, B., D. E. Waliser, E. J. Fetzer, B. H. Lambrigtsen, Y. L. Yung, and B. Wang, 2006: Vertical moist thermodynamic structure and spatial-temporal evolution of the mjo in airs observations. *Journal of the atmospheric sciences*, **63 (10)**, 2462–2485.

Tian, B., D. E. Waliser, E. J. Fetzer, and Y. L. Yung, 2010: Vertical moist thermodynamic structure of the madden-julian oscillation in atmospheric infrared sounder retrievals: An update and a comparison to ecmwf interim re-analysis. *Monthly Weather Review*, **138 (12)**, 4576–4582.

Tompkins, A. M., 2001: Organization of tropical convection in low vertical wind shears: The role of water vapor. *Journal of the atmospheric sciences*, **58 (6)**, 529–545.

Wallace, J. M. and V. Kousky, 1968: Observational evidence of kelvin waves in the tropical stratosphere. *Journal of the Atmospheric Sciences*, **25 (5)**, 900–907.

Wang, B., 2012: Theory. *Intraseasonal Variability in the Atmosphere-Ocean Climate System*, Springer, 335–398.

Wheeler, M. and G. N. Kiladis, 1999: Convectively coupled equatorial waves: Analysis of clouds and temperature in the wavenumber–frequency domain. *Journal of the Atmospheric Sciences*, **56 (3)**, 374–399, doi:10.1175/1520-0469(1999)056⟨0374:CCEWAO⟩2.0.CO;2, URL `http://dx.doi.org/10.1175/1520-0469(1999)056<0374:CCEWAO>2.0.CO;2`.

Wheeler, M. C. and H. H. Hendon, 2004: An all-season real-time multivariate mjo index: Development of an index for monitoring and prediction. *Monthly Weather Review*, **132 (8)**, 1917–1932.

Woolnough, S., J. Slingo, and B. Hoskins, 2001: The organization of tropical convection by intraseasonal sea surface temperature anomalies. *Quarterly Journal of the Royal Meteorological Society*, **127 (573)**, 887–907.

Wu, X. and L. Deng, 2013: Comparison of moist static energy and budget between the gcm-simulated madden-julian oscillation and observations over the indian ocean and western pacific. *Journal of Climate*, **26 (14)**, 4981–4993.

Yamada, H., K. Yoneyama, M. Katsumata, and R. Shirooka, 2010: Observations of a super cloud cluster accompanied by synoptic-scale eastward-propagating precipitating systems over the indian ocean. *Journal of the Atmospheric Sciences*, **67 (5)**, 1456–1473.

Yanai, M., S. Esbensen, and J.-H. Chu, 1973: Determination of bulk properties of tropical cloud clusters from large-scale heat and moisture budgets. *Journal of the Atmospheric Sciences*, **30 (4)**, 611–627.

Yanai, M. and R. Johnson, 1993: Impacts of cumulus convection on thermodynamic fields. *Met. Monogr*, **24**, 39–62.

Yano, J.-I. and M. Bonazzola, 2009: Scale analysis for large-scale tropical atmospheric dynamics. *Journal of the Atmospheric Sciences*, **66 (1)**, 159–172.

Yano, J.-I. and K. Emanuel, 1991: An improved model of the equatorial troposphere and its coupling with the stratosphere. *Journal of the Atmospheric Sciences*, **48 (3)**, 377–389.

Yasunari, T., 1979: Cloudiness fluctuations associated with the northern hemisphere summer monsoon. *J. Meteor. Soc. Japan*, **57 (3)**, 227–242.

Yasunari, T., 1980: A quasi-stationary appearance of 30 to 40 day period in the cloudiness fluctuations during the summer monsoon over india. *Meteorological Society of Japan, Journal*, **58**, 225–229.

Zhang, C., 2005: Madden-julian oscillation. *Reviews of Geophysics*, **43 (2)**.

Zhang, C., J. Gottschalck, E. D. Maloney, M. W. Moncrieff, F. Vitart, D. E. Waliser, B. Wang, and M. C. Wheeler, 2013: Cracking the mjo nut. *Geophysical Research Letters*.

Zhang, C. and S. M. Hagos, 2009: Bi-modal structure and variability of large-scale diabatic heating in the tropics. *Journal of the Atmospheric Sciences*, **66 (12)**, 3621–3640.

Zhang, C. and M. J. McPhaden, 2000: Intraseasonal surface cooling in the equatorial western pacific*. *Journal of climate*, **13 (13)**, 2261–2276.

Zhao, C., T. Li, and T. Zhou, 2013: Precursor signals and processes associated with mjo initiation over the tropical indian ocean*. *Journal of Climate*, **26 (1)**, 291–307.

Zhou, S. and A. J. Miller, 2005: The interaction of the madden-julian oscillation and the arctic oscillation. *Journal of climate*, **18 (1)**, 143–159.

APPENDIX A

Additional Diagnostics

A.1. Conservative Field Reconstruction

Activities such as forecast assessment (Jiang et al, 2008) have motivated attempts to reconstruct the signal of the MJO in certain fields using regression analysis of the leading PC values. This method has the disadvantage of indiscriminately reconstructing each field based solely on the overall amplitude and phase of the index, regardless of how much each field is contributing to the overall amplitude of the index. The CEOF structure, combined with knowledge of phase activity, can be used to reconstruct the MJO signal in fields in a manner that conserves certain desired features of the observed fields. Reconstructing fields with this method ensures that the amplitude and phase of the overall index, as well as each field included in the CEOF structure, remains unchanged from their observed values. In addition, the phase activity of each field remains unchanged, preserving the geographical location of observed MJO related field anomalies. The field reconstruction is given by

$$\text{Reconstructed Field}(\phi_2 - \phi_1)_{j,k} = \frac{\text{phase activity}(\phi_2 - \phi_1) \cdot \text{AE}_{j,n}}{\sum_{n=1}^{N} \text{AE}_{j,n} \cdot \cos \phi_{j.n}} \tag{A.1}$$

where

$$\text{AE}_{j,n} = \sqrt{CEOF1_{j,n}^2 + CEOF2_{j,n}^2} \tag{A.2}$$

is the amplitude of the CEOF structure at grid point n of field j, $(\phi_2 - \phi_1)$ is the range of grid point phase the redistribution of grid point contribution occurs over, and $\phi_{j,n}$ is the relative phase of the field j at grid point n of total N grid points included in the phase range of the reconstruction.